UNIVERSIDADE ESTADUAL DE CAMPINAS

Faculdade de Engenharia Mecânica

ALEXANDRE DE ALMEIDA ALVES

On the correlation between barite sediment compaction and its ultrasound properties

Correlação entre a compactação de sedimento de barita e suas propriedades ultrassônicas

CAMPINAS

2025

ALEXANDRE DE ALMEIDA ALVES

On the correlation between barite sediment compaction and its ultrasound properties

Correlação entre a compactação de sedimento de barita e suas propriedades ultrassônicas

Dissertation presented to the School of Mechanical Engineering of the University of Campinas in partial fulfillment of the requirements for the degree of Master in Mechanical Engineering, in the area of Thermal and Fluids.

Dissertação apresentada à Faculdade de Engenharia Mecânica da Universidade Estadual de Campinas como parte dos requisitos exigidos para a obtenção do título de Mestre em Engenharia Mecânica, na área de Térmica e Fluidos.

Orientador: Prof. Dr. Flávio de Campos Bannwart

ESTE TRABALHO CORRESPONDE À VERSÃO FINAL DA DISSERTAÇÃO DEFENDIDA PELO ALUNO ALEXANDRE DE ALMEIDA ALVES, E ORIENTADO PELO PROF. DR. FLÁVIO DE CAMPOS BANNWART.

CAMPINAS

2025

Ficha catalográfica
Universidade Estadual de Campinas (UNICAMP)
Biblioteca da Área de Engenharia e Arquitetura
Rose Meire da Silva - CRB 8/5974

AL87c

Alves, Alexandre de Almeida, 1996-
On the correlation between barite sediment compaction and its ultrasound properties / Alexandre de Almeida Alves. – Campinas, SP : [s.n.], 2025.

Orientador: Flávio de Campos Bannwart.
Dissertação (mestrado) – Universidade Estadual de Campinas (UNICAMP), Faculdade de Engenharia Mecânica.

1. Ultrassom. 2. Atenuação. 3. Propagação de ondas. 4. Barita. 5. Solos - Compactação. 6. Ultrassonografia. I. Bannwart, Flávio de Campos, 1969-. II. Universidade Estadual de Campinas (UNICAMP). Faculdade de Engenharia Mecânica. III. Título.

Informações complementares

Título em outro idioma: Correlação entre a compactação de sedimento de barita e suas propriedades ultrassônicas
Palavras-chave em inglês:
Ultrasound
Attenuation
Wave propagation
Barite
Soil - Compaction
Ultrasonography
Área de concentração: Térmica e Fluídos
Titulação: Mestre em Engenharia Mecânica
Banca examinadora:
Flávio de Campos Bannwart [Orientador]
Flávio Vasconcelos da Silva
Eric Brandão Carneiro
Data de defesa: 24-06-2025
Programa de Pós-Graduação: Engenharia Mecânica

Objetivos de Desenvolvimento Sustentável (ODS)
Não se aplica

Identificação e informações acadêmicas do(a) aluno(a)
- ORCID do autor: https://orcid.org/0009-0006-9721-8234
- Currículo Lattes do autor: https://lattes.cnpq.br/2151553760561023

Prof. Dr. Flávio de Campos Bannwart, Presidente

Prof. Dr. Flávio Vasconcelos da Silva

Prof. Dr. Eric Brandão Carneiro

A Ata de Defesa com as respectivas assinaturas dos membros encontra-se no SIGA/Sistema de Fluxo de Dissertação/Tese e na Secretaria do Programa da Unidade.

DEDICATION

I dedicate this work to my family and friends, whose unwavering support and encouragement have been invaluable throughout this journey. In particular, to my father, who is no longer with us, but always supported and encouraged my education during my early school years. And to everyone at FEM-UNICAMP, Flow & R Labs and FEQ-UNICAMP who generously offered their help, clarified my doubts, and provided constant support.

ACKNOWLEDGEMENTS

I gratefully acknowledge the financial support from PETROBRAS, which provided funding through FUNCAMP agreement 5971. Their contribution was essential in advancing my work, and I sincerely appreciate their support.

My sincere thanks go to Prof. Dr. Ricardo Augusto Mazza, director of Flow & R Labs, and the entire laboratory staff for their invaluable assistance throughout this research. This work was made possible thanks to the resources and infrastructure provided by Flow & R Labs, part of CEPETRO at the University of Campinas (UNICAMP).

This study was financed in part by the Coordenação de Aperfeiçoamento de Pessoal de Nível Superior – Brasil (CAPES) – Finance Code 001

I am grateful to the School of Mechanical Engineering at the University of Campinas (UNICAMP) for providing the infrastructure and support necessary for this study.

Special thanks are due to my advisor, Prof. Dr. Flávio de Campos Bannwart, whose guidance and encouragement have been a constant source of support. His genuine concern for my well-being and his commitment to keeping me on track—both academically and personally—made a significant difference throughout this journey.

I also appreciate the support of the School of Chemical Engineering at UNICAMP, which provided essential equipment that enabled this research.

Finally, I thank the Department of Physics at the Federal University of Viçosa, the Scanning Electron Microscopy Laboratory, Dr. Kairon Márcio de Oliveira, Prof. Dr. Eduardo Nery, and Prof. Dr. Álvaro Vianna for supplying the microscopy images used in this study.

RESUMO

A caracterização das propriedades acústicas de sedimentos marinhos é essencial para o monitoramento de poços de petróleo em ambientes offshore, onde a compactação desses sedimentos desempenha um papel crítico nas estratégias de alívio do acúmulo de pressão anular (APB). Essa dissertação explora a correlação entre a compactação do sedimento de barita e sua resposta ultrassônica, com foco na atenuação e na velocidade da onda como indicadores-chave do comportamento do sedimento. Dois tipos de amostras foram analisados: barita, um dos principais materiais utilizados para o aumento do peso de coluna de líquido em poços offshore, e esferas de vidro (60-120μm) para avaliar a influência do tamanho e formato dos grãos nas assinaturas acústicas. Uma técnica ultrassônica de alta frequência (400kHz) foi empregada utilizando um único transdutor (pulso-eco), demonstrando também, a viabilidade de configurações econômicas que produzem resultados comparáveis à técnicas mais complexas. Os resultados experimentais revelam uma forte relação entre a compactação de sedimentos e a atenuação acústica para ambos os tipos de amostra, com a barita apresentando uma diminuição na atenuação a medida que a compactação aumenta. Além disso, a velocidade da onda na barita apresentou um claro aumento com a compactação, enquanto tal tendência não foi observada em amostras de esferas de vidro. Essas descobertas contribuem como uma base fundamental para o desenvolvimento de técnicas de sensoriamento remoto para caracterização de sedimentos em ambientes subaquáticos de alta pressão e temperatura, com potenciais aplicações na avaliação da estabilidade de poços de petróleo e gerenciamento de pressão.

Palavras chave: ultrassom, atenuação, velocidade de onda, sedimento de barita, compactação, método pulso-eco, APB

ABSTRACT

Understanding the acoustic properties of granular sediments is essential for offshore oil well monitoring, where sediment compaction plays a critical role in Annular Pressure Build-up (APB) relief strategies. This dissertation examines the correlation between compaction of barite—a common drilling fluid densifier—and its ultrasonic response, focusing on attenuation and wave velocity as key indicators of sediment behavior. Two types of samples were analyzed: barite, the primary weighting material used in offshore wells, and glass spheres ($60 - 120\mu m$) to assess the influence of grain size on acoustic signatures. A high-frequency (200 to $600kHz$) ultrasonic technique was employed using a single transducer (pulse-echo), demonstrating the feasibility of cost-effective setups that yield comparable results to more complex systems. Experimental results reveal a strong relationship between sediment compaction and ultrasound acoustic attenuation for both sample types, with barite exhibiting a decrease in attenuation meanwhile glass spheres exhibiting a high order frequency dependence as compaction increases. Additionally, wave velocity in barite increased with compaction, whereas no such trend was observed in the glass sphere samples. Furthermore, both samples exhibited positive velocity dispersion with frequency. These findings contribute to a primary ground foundation for the development of remote sensing techniques for sediment compaction characterization, with potential applications in oil well stability assessment and pressure management.

Keywords: ultrasound, attenuation, wave-velocity, barite sediment, compaction, pulse-echo method, APB

LIST OF FIGURES

Figure 1.1 – Wellbore annuli schematics. Wang *et al.* 2022 18
Figure 1.2 – APB phenomenon schematics. 20
Figure 1.3 – Simplification of wave propagation and particle behavior (Daniel A. Russell. The Pennsylvania State University Website). 23
Figure 2.1 – Wave velocity (a) and attenuation (b) for low frequencies. Reference: Adapted from Dunlop 1988. 33
Figure 2.2 – Wave velocity (a) and attenuation (b) for high frequencies. Reference: Adapted from Hare & Hay 2018. 39
Figure 3.1 – Spectral analysis procedure. 43
Figure 3.2 – Three transducer layout made by Buckingham & Richardson 2002. 45
Figure 3.3 – Pulse echo method based on Papadakis 1968. 47
Figure 3.4 – Propagation of a broad-frequency wave group through a dispersive medium (Pickering 2024). 53
Figure 3.5 – Phase velocity and group velocity characteristics. Reference: (Shin & Hammond 2008) 54
Figure 3.6 – Phase delay between pulses through Cross-correlation. 55
Figure 3.7 – Photo of the ultrasonic measurement cell utilized in this work. 56
Figure 3.8 – Ultrasonic measurement cell schematics. The type of data captured by the oscilloscope is represented in red. 57
Figure 3.9 – Barite sample at 1,000x magnification. 60
Figure 3.10–Magnification at 3,500x. 61
Figure 3.11–Magnification at 11,000x. 61
Figure 3.12–Morphology of the smaller particles. 61
Figure 3.13–Experimental procedure for compaction control. 63
Figure 3.14–Mechanical wave mode conversion representation. 67
Figure 3.15–Mechanical wave mode conversion for sources with finite sizes. 68
Figure 3.16–No diffraction presence (a), diffraction representation for sources with finite sizes (b). 69
Figure 3.17–Scattering representation for shortwavelength (a) and longwavelength (b). . 71

Figure 3.18–Flowchart illustrating the sequence of data processing steps for the dataset. . 75
Figure 3.19–Transducer half power bandwidth. 78
Figure 4.1 – Attenuation comparison with levels of compaction. 81
Figure 4.2 – Attenuation comparison between Barite samples and Glass Sphere samples. 84
Figure 4.3 – Phase velocity of barite as a function of compaction. 87
Figure 4.4 – Phase velocity of glass spheres as a function of compaction. 88
Figure 4.5 – Comparison of phase velocities between glass spheres and barite samples. . 89
Figure A.1 – Complete vector in time domain. 98
Figure A.2 – Separated echoes in time domain. 99
Figure B.1 – Numerical representation of the wave behavior within the cell using FEM method (Multiphysics 1998). 101
Figure B.2 – Unwanted echoes using a flat back-wall end. 102
Figure B.3 – Unwanted echoes using a inclined back-wall end. 102
Figure B.4 – Unwanted echoes using a positive conic back-wall end. 103
Figure B.5 – Unwanted echoes using a negative conic back-wall end. 103
Figure B.6 – Geometry as the simulation from Fig.B.1(d). 104
Figure B.7 – Geometry as the simulation from Fig.B.1(c). 104
Figure B.8 – Out of scale representation of the improved ultrasonic measurement cells. . 104
Figure B.9 – Geometry tested in COMSOL (Multiphysics 1998). 105
Figure B.10–Sound field within the optimized ultrasound measurement cell. 106
Figure B.11–Acoustic data collected from the probe. 107
Figure B.12–Sample attenuation using FEM. 108

LIST OF ABBREVIATIONS AND ACRONYMS

APB	Annular pressure build-up
NDT	Non-destructive method
FFT	Fast Fourier transform
Unicamp	Universidade Estadual de Campinas
MPD	Managed pressure drilling
SAX99	Sediment collection site 1
SAX04	Sediment collection site 2
GS	Grain shearing models (Buckingham)
COMSOL	(Multiphysics 1998)
DC	Direct current
SNR	Signal-to-noise ratio
SRM	Spectral ratio method
SEM	Scanning electron microscopy
Clay/mud like	Sediment grains in the order of dozens of μm
Sand like	Sediment grains in the order of hundreds of μm

LIST OF SYMBOLS

P	Static pressure
p	Acoustic pressure
$\mathbf{p}$	Complex acoustic pressure
P_0	Acoustic pressure amplitude
$\dot{Q}$	Fluid flow
τ	Shear stress
$\overrightarrow{u}$	Acoustic particle velocity
η	Shear viscosity
η_B	Bulk viscosity
ρ_0	Density
t	Time
t_g	Group delay
t_p	Phase delay
ϕ	Phase difference between the two echoes
ϕ_g	Phase difference between the two echoes (group)
ϕ_p	Phase difference between the two echoes (phase)
δ	Partial derivative
f	Frequency
s	Condensation
c_p	Wave phase velocity
c_g	Wave group velocity

k	Wave number
τ_s	Relaxation time
$\mathbf{k}$	Complex wave number
λ	Wavelength
α	Attenuation
α_1	Buffer rod's attenuation
α_2	Sample's attenuation
$\alpha_{2,s}$	Sample's attenuation in Buckinghams's method
$\alpha_{2,w}$	Reference (water) attenuation in Buckinghams's method
w	Angular frequency
j	Imaginary number
a	Grain diameter
$\mathcal{O}$	In the order of
R_{12}	Reflection coefficient buffer rod/sample interface
R_{23}	Reflection coefficient sample/back-wall interface
R_{ref}	Reflection coefficient buffer rod/sample interface using calibrant
T_{12}	Transmission coefficient buffer rod/sample interface
T_{21}	Transmission coefficient sample/buffer rod interface
d	Transmitter diameter
$D_{ref/1/2}$	Diffraction correction reference $\&$ buffer $\&$ sample
l	Buckingham's method receivers distance
l_1	Papadakis' method buffer rod depth
l_2	Papadakis' method sample depth

A_{in}	Papadakis' method pressure amplitude power spectrum (emitted pulse).
A_1	Papadakis' method pressure amplitude power spectrum (entry echo).
A_2	Papadakis' method pressure amplitude power spectrum (back-wall echo).
B_1	Buckingham's method pressure amplitude power spectrum Mic.1.
B_2	Buckingham's method pressure amplitude power spectrum Mic.2.
$Z_{acrylic}$	Acrylic buffer rod impedance.
Z_{Steel}	Stainless steel back-wall impedance.
Z_s	Sample's impedance.
K_1	Elastic constant of the porous material for low frequency.
K_2	Elastic constant of the porous material for high frequency.
ka	Frequency normalized with the grain size

CONTENTS

1 INTRODUCTION 17

1.1 Research contextualization 17

1.1.1 Annular pressure build-up 18

1.1.2 Remote Survey of Offshore Wells 21

1.2 Mechanical Waves 22

1.3 Research objectives 26

2 LITERATURE REVIEW 28

2.1 Wave propagation through wet sediments 28

2.2 Biot-Stoll Theory 29

2.3 Theoretical Alternatives 36

2.4 Theoretical understanding of the compaction correlation 38

3 METHODOLOGY 41

3.1 Techniques for measuring acoustic properties. 42

3.1.1 Domain analysis and processing 42

3.1.2 Wave attenuation processing 44

3.1.2.1 Buckingham's approach 44

3.1.2.2 Papadakis' method 46

3.1.2.2.1 Buffer rod and back-wall made of the same material 49

3.1.2.2.2 Buffer rod and back-wall made of different materials 50

3.1.3 Wave velocity processing 52

3.2 Design of the experimental setup 56

3.2.1 Ultrasonic measurement cell geometry 56

3.2.2 Samples, working frequencies and applied power 60

3.2.2.1 Barite and glass spheres morphology 60

3.2.2.2 Compaction control 62

3.2.2.3 Frequency range 63

3.2.2.4 Electronic equipment 64

3.2.3 Measurement challenges and future improvements of the ultrasonic cell 64

3.2.4 Planar wave considerations and scattering 65

3.2.4.1 Mode conversion 66
3.2.4.2 Diffraction 68
3.2.4.3 Scattering 69
3.3 Diffraction Correction 71
3.4 Data acquisition and processing 74
4 RESULTS AND DISCUSSIONS 80
4.1 Attenuation 80
4.2 Phase velocity 86
5 CONCLUSIONS 90

Bibliography 93
APPENDIX A Collected data representation 98
APPENDIX B Numerical Simulation for Experimental Cell Optimization 100

1 INTRODUCTION

This dissertation is organized as follows:

In Sec. 1.1, the motivation behind investigating the correlation between barite sediment compaction and its ultrasonic properties is discussed, emphasizing its significance in field applications. Following, in Sec. 1.2, the choice of acoustic waves for this investigation is justified, highlighting their capability for remote underwater sensing. In Sec. 1.3, the main goals of the present research are outlined.

2. Next, in Sec.2 acoustic models are introduced, and their relevance to characterizing barite compaction is discussed. The section begins by presenting the early pioneers who developed the foundations of acoustic sediment theory in the early 20th century, followed by a discussion of contemporary acoustic models that build upon these theories to investigate the physical properties of sediments.

3. Sec. 3 presents the methodology adopted for data acquisition, signal processing, and the construction of the experimental apparatus. First, in Sec. 3.1, the processing of acoustic data in the frequency domain is detailed, followed by the mathematical methods used to extract and compare the desired acoustic parameters. Then, in Secs. 3.2 and 3.3, the experimental setup is described, along with the main challenges encountered during implementation and the solutions adopted to overcome them for future applications Sec.3.2.3.

4. In Sec. 4, the experimental results are analyzed. The effects of varying barite compaction levels on P-wave attenuation (Sec. 4.1) and P-wave velocity (Sec. 4.2) are investigated. Additionally, the acoustic properties of compacted glass spheres are also examined for comparative analysis.

5. Finally, in Sec. 5, the experimental findings are discussed, including an evaluation of whether the research objectives were successfully achieved.

1.1 Research contextualization

Petroleum is a naturally occurring liquid, ranging in color from yellow to black, found in geological formations beneath the Earth's surface. It is typically processed into various fuels and is considered an essential global energy resource. Its extraction is often made by drilling process (springs are not common), hence, engineering efficiently ways to extract it from

the formation are always on the mind of the oil and gas companies around the world (Schulte).

Over the decades, increasingly complex drilling environments have become accessible, ranging from onshore wells to highly sophisticated offshore wells designed to reach extremely deep oil and gas formations. Some offshore pipelines extend for thousands of meters and are subjected to significant temperature gradients along their length, from the ocean surface to the seabed and into the formation. These gradients increase the likelihood of the annular pressure build-up (APB) phenomenon.

1.1.1 Annular pressure build-up

Annular Pressure Buildup (APB) refers to the pressure increase caused by the thermal expansion of confined fluids within the various annuli that make up a wellbore as they are heated. A schematic representation of these annuli is shown in Fig.1.1.

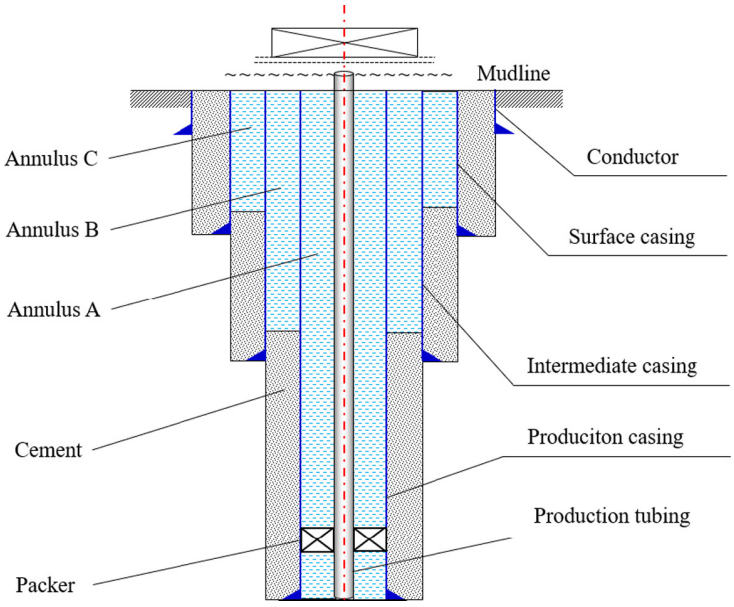

Figure 1.1 – Wellbore annuli schematics. Wang *et al.* 2022

According to Moe & Erpelding 2000, this phenomenon is present in every well ever produced, yet it is generally overlooked by well designers. This phenomenon has gained attention due to the extreme conditions faced in recent decades, including deeper cold water production and hotter extraction formations (Moe & Erpelding 2000). Given that the pressure rise is a function of fluid properties and temperature changes, there is a clear relationship between these factors, which underscores the need for a comprehensive study.

The occurrence of annular pressure buildup in the annuli has been documented by the industry for many years (Adams & MacEachran 1994). A notable case occurred in the Marlin oil field in the Gulf of Mexico, where casing pipes collapsed due to excessive annular pressure, leading to a temporary shutdown of operations. This incident highlighted the critical importance of protecting annular trap casings, making it a key factor to consider in the design of deep-water oil and gas wells.

There are some methods for reducing annular pressure buildup, such as increasing the annulus strength, removing the annulus itself, and pressure relief, bleeding valves, relief seals, each having advantages and disadvantages. Onshore platforms and spar-type wells with access to the annuli generally manage annular pressure build-up by periodically relieving the pressure as required (Vargo Richard F. *et al.* 2003). However, this procedure isn't simple for off-shore cases.

With this in mind, among the APB mitigation strategies for off-shore platforms, ensuring communication between the annulus and the formation is often considered; i.e deep when the pressure of the confined fluid exceeds the fracture pressure of the formation, the drilling fluid can be displaced from the annulus to the formation.

These challenges highlight a critical conclusion: controlling subsurface pressure is essential in extraction operations. To manage these pressures, high-density minerals such as barite and hematite are commonly added to drilling fluids to increase their density (Nguyen *et al.* 2011). However, the sedimentation of the weighting material particles under suspension causes fluctuation in fluid density and consequently several problems during drilling or completion (Calçada *et al.* 2016).

Sedimentation is the process by which solid particles settle out of a fluid in which they are suspended and accumulate against a barrier. This phenomenon occurs as the particles move through the fluid under the influence of forces such as gravity, centrifugal acceleration (due to de inertia of the particle), or electromagnetic forces. The accumulation of solid particles at the bottom of the drilling string can create numerous challenges during the oil extraction process. These include erosion, reduced drilling efficiency, decreased oil permeability, and increased pressure. Taken together, these issues contribute to higher overall costs in oil and gas production (Irawan *et al.* 2017).

To mitigate these problems, studies are carried out in a way that manages sediment-related problems. Some examples are carefully formulated drilling fluid systems that remove

sediment from the drilling zone, Managed Pressure Drilling (MPD), advanced sensors and monitoring technologies, allowing operators to detect and respond promptly to changes in well conditions. Even with all these approaches presented, there are no general or satisfactory solutions and the proper characterization of this phenomenon, still a difficult task (Nguyen *et al.* 2011).

Another challenge posed by sedimentation arises in approaches where pressure communication between the annulus and the formation is intended. In such scenarios, Calçada *et al.* 2016 report that, over time, barite sedimentation (or sag) in the drilling fluid can form an impermeable layer within the formation pores. This layer may obstruct pressure transmission from the annulus to the formation, potentially compromising the communication strategy.

The main idea of such phenomenon, also proposed by several authors other than Calçada *et al.* 2016 is presented illustrated in Fig. 1.2.

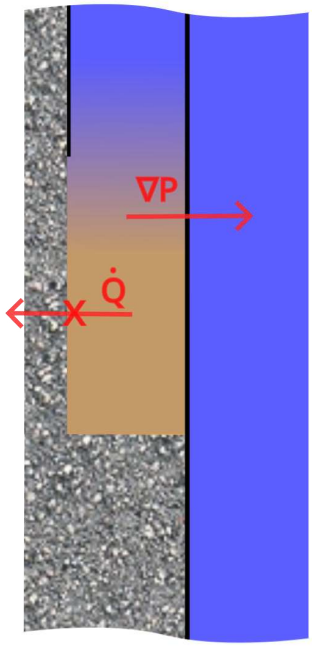

Figure 1.2 – APB phenomenon schematics.

As shown in Fig. 1.2, the increase in pressure resulting from the thermal expansion of the downstream cold fluid, as it heats from the top to the high temperatures at the bottom, can lead to significant pressure buildup ΔP. If the pressure relief is situated in a zone with sufficient particle (barite) compaction, preventing timely pressure relief, this may lead to the fracturing of the annulus. Therefore, the development of a way to observe the barite compaction behavior within the wellbore is extremely useful for field monitoring applications.

1.1.2 Remote Survey of Offshore Wells

Several direct contact methods are possible, such as the placement of numerous pressure transmitters along the string to the bottom, or temperature measurement devices. However, this approach faces many problems in field applications due to the extremely inhospitable environment inside offshore wells, creating measurement gaps and money waste due to replacement or rescheduling of the internal team for the task. The use of remote devices addresses several of these issues, which is why remote measurements have become a viable option.

There are numerous remote measurement methods, which can be categorized into two types of wave communication: mechanical waves and electromagnetic waves. Both play a crucial role in characterizing materials and different media. Since our case involves an underwater environment, acoustic waves are the most prominent and least attenuated type of mechanical wave. Therefore, they will be used in subsequent analyses.

Acoustic wave methods include techniques such as:

- High-frequency pulsed waves;
- Low-frequency steady waves;
- Resonance chambers.

Similarly, electromagnetic wave methods also have various techniques, such as:

- Transmission and reflection-based techniques;
- Resonance-based methods;
- Time-domain devices.

The name of the technique depends on several factors, including the dependence on the transducer position, the number of transducers, the type of transducer (emitter, receiver, or both), the frequency range used, and whether there is direct contact with the material or not.

This classification highlights the diverse range of techniques available for remote material characterization.

Building on this, the present work aims to offer a preliminary validation of the acoustic ultrasound response at various stages of barite solid particle compaction, thereby laying the foundation for a remote method to monitor the phenomena mentioned above.

Knowing that our problem is solid particle sedimentation under high-pressurized fluids, along hundreds/thousands of meters deep, mechanical waves seem to be a feasible way to fulfill it. The origins of underwater acoustics date back to 1490, Leonardo da Vinci being one of the pioneers, who wrote: “If you cause your ship to stop and place the head of a long tube in the water and place the outer extremity to your ear, you will hear ships at a great distance from you.” Fast forward to the beginning of the twentieth century, amid the tensions leading to World War I and following the sinking of the Titanic in 1912, there was a surge in patents related to underwater communication and object localization. Since then, mechanical waves have been used in underwater environments for decades.

The popularity of acoustic waves over electromagnetic ones in an underwater environment is due to its low attenuation during propagation through this media. Electromagnetic waves are highly attenuated underwater, so for distant communications or localization, their use is more feasible in low density media, such as air or vacuum. This is the mainly difference between mechanical and electromagnetic wave propagation, the first one needs a medium to propagate through. This characteristic makes mechanical waves particularly important for characterizing high-density media; all their physical properties, such as amplitude variation, velocity, diffusion, and others, depend on the type of medium through which the wave propagates.

For this reason, it is reasonable to infer the acoustic properties and behavior of a mechanical wave from the physical properties of the medium, such as density, bulk modulus, porosity, permeability, and other relevant parameters, depending on the type of medium.

As we shall see in Sec.1.2, a mechanical wave describes how mechanical energy propagates through a compressible medium, allowing this vectorial propagation to be in a specific direction due to the spring-like reaction in its microstructure. This phenomenon is closely related to the properties of the medium, highlighting the importance of mechanical waves for a comprehensive understanding of the medium.

1.2 Mechanical Waves

Mechanical energy transported through a material medium is called mechanical waves. For example, when a rod is moved from one place to another, the motion occurs at the material’s speed of sound. In other words, for the displacement applied to one side of the rod to reach the other side, the mechanical energy must be transmitted through the material at the speed of sound of the material, as governed by mechanical waves.

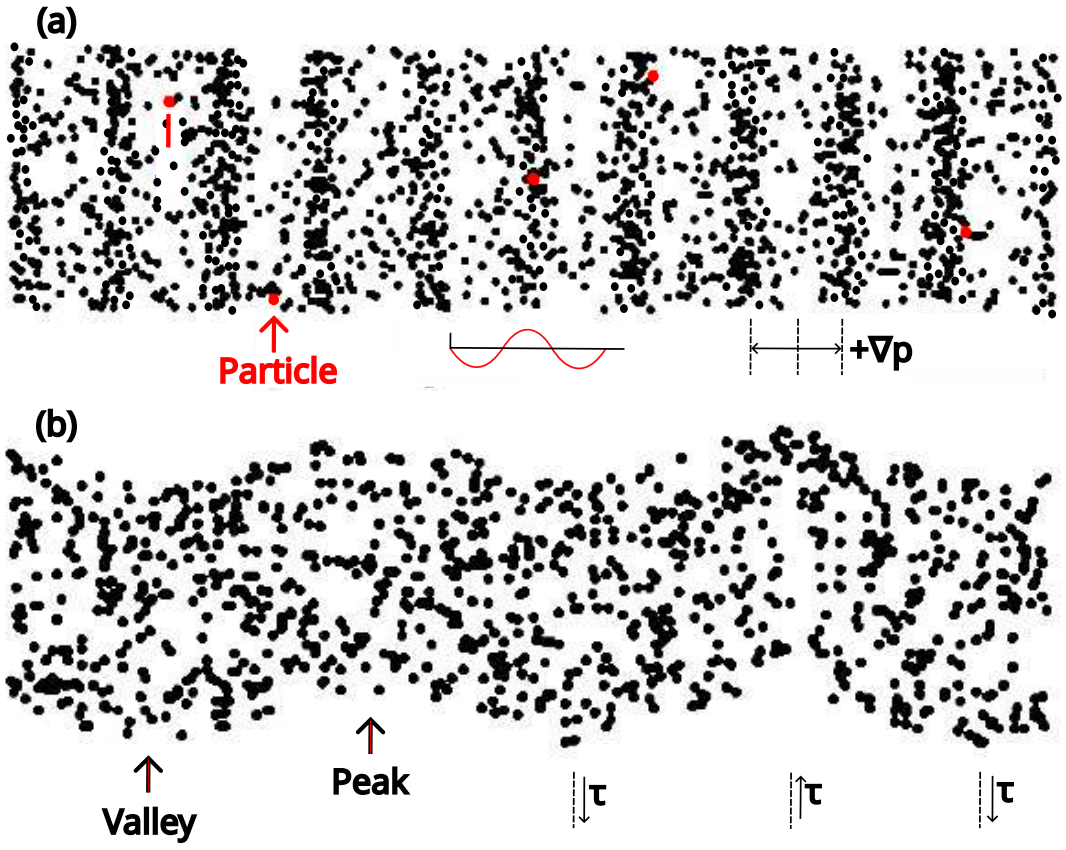

Figure 1.3 – Simplification of wave propagation and particle behavior (Daniel A. Russell. The Pennsylvania State University Website).

There are two main types of wave propagation, the longitudinal and transversal, as can be seen in Fig.1.3.

When dealing with mechanical wave propagation in solids, such as a rod, it is unlikely that only one type of wave propagation occurs. For example, if a hammer strikes the center of the cross-sectional area of the rod, a slight eccentricity will generate transverse waves. This type of elastic motion is associated with shear stress τ, where the force is always perpendicular to the direction of energy transport, as illustrated in Fig.1.3(b). In contrast, when dealing with fluids, where shear forces are negligible compared to compression and rarefaction (normal) pressures ∇p, wave propagation is typically assumed to be predominantly longitudinal (compression), as shown in Fig.1.3(a) (Kinsler *et al.* 2000).

Nearly inviscid fluids experience fewer limitations to deformation compared to solids. The restoring forces that drive wave propagation in fluids are the pressure variations that arise when the fluid undergoes compression or expansion ∇p. Fluid elements move back and forth in

the direction of the applied forces, creating alternating regions of compression and rarefaction, similar to the behavior of longitudinal waves in a bar.

For the development of all the acoustic equations needed to understand our phenomena, the continuum assumption must be made. Which is basically that all the fluid element have enough number of particles, ensuring that properties are constant throughout the entire volume. The terms "fluid element" and "acoustic particle" refer to an infinitesimally small volume of fluid that is sufficiently large to encompass millions of molecules, allowing the fluid to be treated as a continuous medium. At the same time, it is small enough to ensure that all acoustic properties remain uniform within that volume.

In a fluid, the molecules do not have fixed average positions within the medium. Even in the absence of an acoustic wave, they constantly move in a random fashion, with their average velocities far exceeding the velocities of particles associated with wave motion. However, a small volume can be treated as a stable unit, as any molecules leaving its boundaries are, on average, replaced by an equal number with similar properties, ensuring that the macroscopic characteristics of the element remain constant.

We also must create a small displacement of the source within the range of linear acoustics. This ensures that the changes in the density of the medium remain small compared to its equilibrium value. The amplitude is dependent on a parameter, called condensation, that describes how much the medium is compressed as the sound wave moves. When the condensation reaches certain levels, the sound becomes nonlinear (Kinsler *et al.* 2000).

Without linear simplification, we first have the nonlinear Navier-Stokes equation Eq.1.1.

$$\rho\left(\frac{\delta\overrightarrow{u}}{\delta t}+(\overrightarrow{u}\cdot\nabla)\overrightarrow{u}\right)=-\nabla p+(\frac{4}{3}\eta+\eta_B)\nabla(\nabla\cdot\overrightarrow{u})-\eta\nabla\times\nabla\times\overrightarrow{u}. \tag{1.1}$$

The last two terms on the right represent the expansion of the viscous stress tensor, accounting for bulk viscosity η_B and shear viscosity η. Unlike the simplifications typically applied to fluids under Stokes' hypothesis, the divergence of the velocity field must be explicitly considered in this case.

The bulk viscosity, η_B, governs the energy losses associated with compressibility and density variations, which are particularly relevant for the propagation of sound waves. In contrast, shear viscosity, η, accounts for viscous losses due to shear deformation between fluid layers with differing velocities; this makes it a factor in absorption even during purely longitudinal

motion. Both processes involve a finite time for the system to return to equilibrium following changes in density and temperature caused by compression or expansion. These delays lead to the conversion of acoustic energy into random thermal energy.

Using the assumptions made previously, we can simplify Eq.1.1 using the linearized equation of continuity Eq.1.2:

$$\nabla \cdot \overrightarrow{u} = -\frac{\delta s}{\delta t}, \tag{1.2}$$

which can be applied for small perturbations, turning the bulk density equal to the media density which is independent of space and time. With the linearization of the left side of the momentum equation Eq.1.1, assuming the process to be adiabatic:

$$p = \rho_0 c^2 s, \tag{1.3}$$

and assuming a mono frequency motion e^{jwt}, we can reduce the lossy wave equation to the lossy Helmholtz equation Eq.1.4:

$$\nabla^2 \mathbf{p} + \mathbf{k}^2 \mathbf{p} = 0. \tag{1.4}$$

With **k** being:

$$\mathbf{k} = k - j\alpha. \tag{1.5}$$

By assuming the linearity of the wave equation, the complete solution can be constructed by superimposing the individual solutions for each frequency. A physical analogy for this process is the behavior of light waves. Similarly, as one can study the behavior of red, orange, yellow, green, blue, indigo, and violet light individually and then combine them to understand the overall behavior of white light, the same approach can be applied to construct a general wave solution by combining the responses of its constituent frequencies.

The harmonic solution, expressed in the complex form as a function of the acoustic pressure propagating as a plane wave described by the differential equation Eq.1.4, is given by:

$$\mathbf{p} = P_0 e^{-\alpha x} e^{j(wr - kx)}. \tag{1.6}$$

All of these equations account for various losses in wave propagation across a wide range of fluids, including water, accounting for viscous losses, heat conduction losses, and losses

associated with internal molecular processes, which are commonly referred to as molecular or relaxational sound absorption.

It's worthy to now that all these equations break down at frequencies where the relation $w\tau_s \approx 1$ holds. Given that $\tau_s \approx 1 \times 10^{-12} s$ for most liquids, except for highly viscous liquids such as glycerin, the operational frequency must be below $1.5915964 \times 10^{12} Hz$ to maintain the validity of the continuum hypothesis, thankfully such frequency is far higher the one utilized in this work (Kinsler *et al.* 2000).

Since the primary interest is in the decay of pressure due to attenuation, rather than the oscillatory nature of the sound wave, the harmonic solution for the "lossy" Helmholtz equation given by equation Eq.1.6 can be written as:

$$p = P_0 e^{-\alpha x}. \tag{1.7}$$

The representation of amplitude decrement as a mechanical wave propagates through a lossy medium is typically described by an attenuation factor, α. This type of absorption occurs in all media through which a mechanical wave propagates, with varying levels of strength depending on the properties of the medium. This makes attenuation an excellent parameter for characterizing the properties of a desired medium.

Nevertheless, since the objective of this dissertation is to analyze the compaction of granular medium (barite) rather than a homogeneous fluid, understanding the differences in their acoustic loss mechanisms is crucial. Due to this, the acoustic aspects of granular media will be discussed in detail in the next section, supported by information from various sources of the literature.

1.3 Research objectives

The three main purposes of this dissertation are as follows:

1. To obtain P-wave sound speed and attenuation measurements in sedimented barite within the high-frequency range (hundreds of kilohertz), establishing reference data for the use of high-frequency ultrasound waves to study the physical behavior of underwater barite compaction.

2. Establish a comparison between barite sediment and fine-grained glass spheres to better understand the influence of grain size on the acoustic behavior during the granular compaction process.

3. Simultaneously, to propose a novel measurement cell arrangement for granular media. This new experimental setup, featuring a monostatic transducer, will have its applicability evaluated through comparison with specialized literature, highlighting its relevance for sediment characterization.

2 LITERATURE REVIEW

The goal of this section is to provide a comprehensive overview of the significant efforts made over the decades to understand and predict the acoustic behavior of sedimentary media. First, we will present the pioneering researchers who established the foundations for the modern understanding of such phenomena, with a focus on achieving a physical comprehension of ultrasonic acoustic behavior in water-saturated sedimentary media, such as barite. Moreover, at the end of the section, recent works will be presented that reflect our current understanding of the physics behind sedimentary acoustics.

2.1 Wave propagation through wet sediments

Since barite $BaSO_4$ is a sedimentary mineral and its compaction process occurs similarly to that of seafloor sediments, it is reasonable to apply acoustic theories developed over decades to better understand the behavior of this phenomenon. According to McClements 1996, the acoustic properties of a particle system are influenced by changes in the phase and magnitude of the wave resulting from interactions between the ultrasonic wave, the particles and the surrounding liquid. This is particularly relevant for the sensitive probing of various granular processes, such as compaction, avalanches, and shear band formation (Tournat & Gusev 2010).

Another example is from Zhang *et al.* 2021, which has shown that the frequency-dependent attenuation behavior of a sound wave can be used to characterize the microstructural properties of materials, such as grain size and porosity. This approach is valuable for structural health monitoring, including the detection of early damage and defects in structures.

Sediments may be assumed to be two-phase composite materials made of granular media filled with fluid in its pores. The acoustic response of sediments resembles that of suspension of particles in a fluid, characterized by low rigidity and shear modulus (Dunlop 1988). For all such materials, the particle size is comparable to the overall size of the system. This similarity in scales results in the inherent heterogeneity observed in these systems.

To avoid misunderstandings, Jackson & Richardson 2007 divided the granular properties of sea sediments in two groups, the geophysical and geoacoustic properties.

In acoustic modeling, a distinction is often made between geoacoustic parameters and physical parameters, both of which play critical roles in understanding and predicting wave

propagation in granular media such as sediments.

Geoacoustic parameters are derived quantities that describe the acoustic properties of a medium as they relate to wave propagation and attenuation. These parameters include quantities such as wave velocity (both phase and group velocities), attenuation coefficients, acoustic impedance, and reflection coefficients. Geoacoustic parameters are typically obtained through experimental measurements or derived from wave-based models and are directly tied to the interaction of acoustic waves with the medium.

In contrast, physical parameters are the fundamental properties of the medium that define its material characteristics. These include porosity, density, grain size, bulk modulus, shear modulus, permeability, and fluid saturation. Physical parameters describe the inherent structure and composition of the medium and are independent of wave propagation. However, they form the basis for the calculation or estimation of geoacoustic parameters.

The relationship between these two sets of parameters is central to acoustic modeling. Physical parameters serve as input for theoretical models, such as Biot's theory or scattering-based models, which predict the geoacoustic behavior of the medium.

For example, Jackson & Richardson 2007 stated that acoustic impedance is a commonly used geoacoustic parameter, valued for its ease of measurement and strong correlation with other physical properties; as well as the acoustic attenuation of an ultrasonic wave passing through a fluid, which is higher in the presence of suspended particles compared to when they are absent (Flammer 1962).

Building on this understanding, several researchers developed theories to explain the relationship between geoacoustic and physical parameters in seafloor sediments, aiming to predict one property using another as input. These investigations paved the way for this work for exploring the feasibility of using acoustic waves to more effectively characterize barite porosity and permeability (compaction level) through the geoacoustic properties of the medium, specifically wave velocity and attenuation.

2.2 Biot-Stoll Theory

The first successfully attempt to relate acoustical properties with the composition of a heterogeneous dispersion in a surrounding liquid was accomplished by Wood (Wood 1946). Wood saw that the adiabatic bulk modulus of a suspension with one or more heterogeneity heterogeneities is equal to the sum of the modulus of each component multiplied by its fraction

of the total volume. In his work, he exemplified the applicability of his model to a water-air mixture but stated the applicability for a liquid-solid mixture. In subsequent studies, researchers tested his equations on various sediment types, finding that Wood's theory aligned more closely with refined (clay-like) sediments and deviated significantly from experimental data for coarser (sand-like) sediments. This deviation is attributed to the model's assumption that the sediment behaves as a fluid.

According to Dunlop 1988, Gassman 1951 proposed that assuming an elastic wave propagation through a spherical packing filled with liquid or gas, the elastic modulus should account for the interparticle interaction of the skeletal frame formed by the integration between the particles. His assumption improved those wave velocities results yielded by Wood's model, though they were still far from the ideal at the time.

Zwikker 1949 studied an air saturated porous material assuming compressional waves only. Although its results had a lot of simplification, the idea behind a vibration between the skeletal solid frame and the saturated fluid is an extremely intuitive vision and it is worth understanding the physics behind the wave propagation throughout a porous media. Their results were later utilized and improved by Biot.

In 1956, Maurice Anthony Biot introduced a groundbreaking theory on sound propagation in isotropic, homogeneous, poroelastic media saturated with a viscous fluid (Biot I 1956; Biot II 1956).

Building on the foundational work of Zwikker 1949, which examined air-saturated elastic porous materials, Biot developed a more comprehensive framework that incorporates all relevant physical mechanisms in a systematic and quantitative manner focusing on liquid-saturated elastic porous materials.

Biot essentially considered the relative motion of an elastic fluid within an elastic porous cube, calculating the strain energy by assuming that it depends on the divergence of the relative flow between the fluid and the solid, as well as the cubic strain or dilatation. He applied elastic theory, which states that the strain energy is a quadratic function of the strain invariants and the divergence of the relative displacement.

These assumptions allowed Biot to derive a set of constitutive equations for porous materials, establishing relationships between stress and strain in such systems. This set of equations included four constants, which he related to bulk parameters commonly used to describe porous systems. With these constitutive equations, he applied the equations of motion

to both a volume element attached to the porous frame and to the fluid moving in and out of this element (Dunlop 1988).

Biot accounted also for the viscous resistance being a frequency dependent variable for high frequencies, where the pore flow deviate from the Poisseuille regime. His theory serves as the foundation for understanding the acoustic properties of porous fluid-filled sediments, providing predictions for both dilatational and shear wave propagation. Due to its versatility, Biot's theory is a generalized model that requires several input parameters (physical properties of the sediment), making it challenging to accurately evaluate all the necessary parameters.

To highlight the broad applicability of Biot's approach, it is useful to compare it with previously developed methods by Wood 1946 and Gassman 1951, which are specific cases of Biot's theory. The former assumes fluid-like behavior, while the latter focuses on differential elastic properties.

In spite of that, Biot's theory, as discussed in this section, is not the only existing formulation, but remains one of the most widely used, thanks in part to the adaptations by Stoll for granular media (Stoll 1989). Specifically, the Biot-Stoll model interprets the collection of grains that constitute the sediment as the porous frame through which pore fluid can flow.

Apart from this adjustment in the geometry of the model, no major modifications were required to extend the theory to granular media. This adaptation is often referred to as the "Biot-Stoll theory."

According to McCann & McCann 1969, the Biot equation that relates acoustical attenuation α with frequency f can be represented as Eq. 2.1:

$$2\alpha = K_1 f + K_2 f^{1/2}. \tag{2.1}$$

In this equation, K_1 cannot be determined due to the absence of a theoretical framework. In contrast, K_2 can be calculated using Biot's (Biot II 1956) equations, provided that all the elastic coefficients necessary for the specific sediment are known. The concepts regarding the importance of each term will be discussed in greater depth at an appropriate point in this section.

The concept of correlating geoacoustic properties with physical characteristics is straightforward; however, it remains an extremely challenging task due to the inherent complexity of the granular media.

Unconsolidated granular media, such as assemblies of elastic beads in noncohesive contact, represent one of the most complex classes of materials for studying acoustic wave

propagation. These materials exhibit a wide range of phenomena that influence mechanical waves, including velocity dispersion, nonlinear behaviors (such as hysteresis, clapping effects, and classical nonlinearity), scattering caused by bead interactions, contact and geometrical disorder, and force chain dynamics. Additional complexities arise from anisotropy, memory effects, relaxation processes, thermoelastic interactions, mode coupling (e.g., Biot waves and rotational waves), macroscopic inhomogeneities (such as elastic property gradients), spatial correlations, and fragility. Together, these features make wave propagation in such media particularly challenging to analyze and model

There exist various medium configurations and wave parameters, each influencing the dominance or insignificance of certain processes in linear and nonlinear acoustic propagation (Tournat & Gusev 2010). As highlighted by Biot's theory, the acoustic properties generally depend on 14 parameters; however, the impact of these parameters varies according to the sediment type and frequency (Dunlop 1988). Consequently, it becomes the responsibility of the acoustic modeler to effectively manage all these parameters, focusing primarily on the critical ones that contribute significantly to geoacoustic characterization.

Based on the Biot-Stoll theory, we can assume two types of wave propagation regime through granular media. The first is the long-wavelength regime, which is characterized by wavelengths with nominal sizes much bigger than those of porous structures $ka << 1$. This type of regime seems to fit well with the results obtained by Wood 1946, which assumes the granular medium as an isotropic fluid. Relative movement between the skeletal frame and the pore fluid is not established due to the significant restriction to flow imposed by the porous parameters in comparison to the inertial forces exerted by the mechanical wave on the fluid. In this regime, the acoustic wave is primarily propagated through the beads and their contacts. Consequently, the entire medium can be treated as a single homogeneous medium with uniform characteristics (Dunlop 1988).

When this regime is more dominant, the first term on the right-hand side of Eq. 2.1 prevails, causing the attenuation to scale approximately linearly with frequency Fig.2.1(b) f^1. A simplified representation of wave velocity and attenuation based on Biot's theory is shown in Fig. 2.1, which is adapted from an image in Dunlop's work (Dunlop 1988).

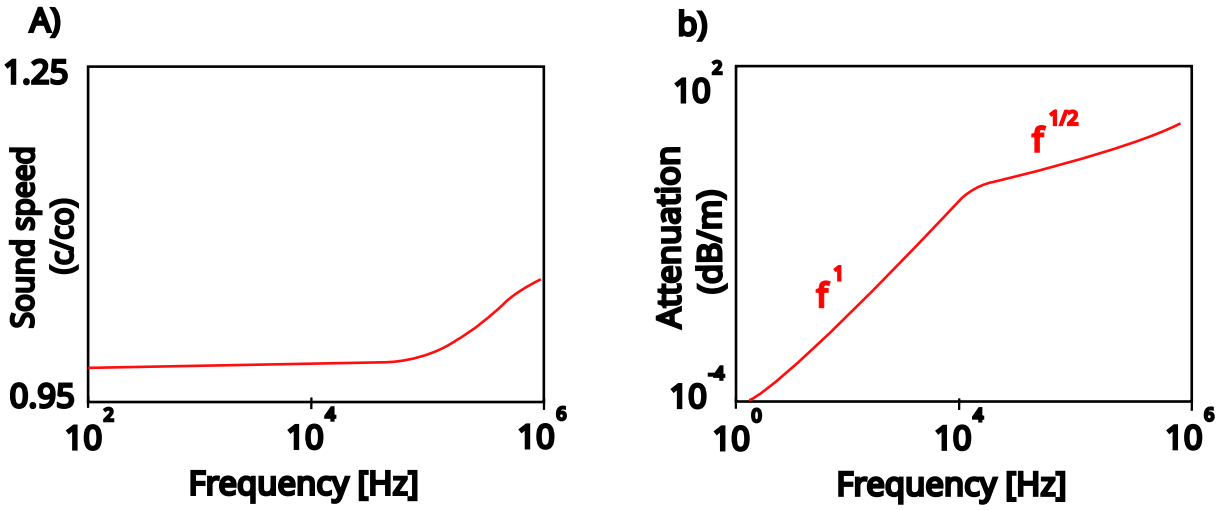

Figure 2.1 – Wave velocity (a) and attenuation (b) for low frequencies. Reference: Adapted from Dunlop 1988.

It is important to note that in a long-wavelength regime $ka << 1$, maintaining a constant frequency while increasing the grain size (eventually reaching a "sand-like" granular medium) can transition the system into a short-wavelength regime Fig.2.1(b) $f^{1/2}$. Conversely, a granular medium initially in a short-wavelength regime can shift to a long-wavelength regime by lowering the frequency of the excited wave or reducing the grain size.

While varying the frequency in the long-wavelength regime, McCann & McCann 1969 observed that the wave attenuation varies linearly with frequency, which is supported by the Biot-Stoll model. In this regime, where the relative movement between the pore fluid and the frame is negligible, the only loss mechanism is frame damping, which exhibits this linear relationship with frequency variations, as noted. In the long-wavelength regime, where $ka << 1$, the assumption of spherical grains by theoretical models has shown satisfactory agreement with some experimental results (Wu *et al.* 1993).

Some insights can be drawn from the developments made by McCann & McCann 1969, such as the fact that since there is no relative movement between fluid and frame, geometrical properties like pore size and grain shape should not influence the attenuation considerably. This assumption has been confirmed by several authors over the years, but it is only valid for long-wavelength regimes.

Another important point is that if the granular medium behaves like a homogeneous liquid, the frequency changes should not affect the wave velocity in the long-wavelength regime, which was observed by Shirley D. J. ; Bell 1979. However, in high-frequency regimes, the

wave velocity changes in function of frequency depending on various parameters of the porous material.

In the transition region, near the characteristic (relaxation) frequency—represented as $10^4 Hz$ in 2.1(b), viscous losses arise from slight relative motion between the fluid and solid frame. As multiple loss mechanisms overlap in this range, the frequency dependence of attenuation can temporarily increase to an f^2 scaling. According to their work, Biot proposed that viscous resistance is frequency-dependent, leading to a nonlinear behavior of wave damping with varying frequency. This implies that the transition from linear to nonlinear attenuation behavior indicates the increasing significance of viscous resistance, making it a crucial mechanism for characterizing granular microstructures.

For the short-wavelength regime *ka* $\approx \mathcal{O}(0.05)$, represented in Fig.2.1(b) $f^{1/2}$, the inertial forces are able to overpower the viscous forces, generating relative movement between fluid and skeletal frame. This can be visualized as follows: increasing the wave frequency results in a reduction of the wavelength, while the wave amplitude remains unchanged. Since amplitude represents the gradient between compression and rarefaction in a dilatational wave, this results in a greater particle displacement over a shorter distance. Consequently, higher inertial forces are imposed within that region.

As mentioned above, this regime can be achieved using frequencies in which the wavelength has dimensions similar to those of the porous structures of the medium $ka \approx \mathcal{O}(0.05)$, but not too similar to avoid a drastic presence of scattering. In this regime, viscous losses become more prominent, as stated by Dunlop 1988.

For this frequency region, the second term on the right-hand side of Eq. 2.1 prevails, causing the attenuation to scale approximately with the square of frequency $f^{1/2}$ Fig. 2.1(b).

Another important characteristic of this short-wavelength regime is the dependence of the geoacoustic parameters on the geometrical properties of the grains. Parameters such as pore size, grain size, and permeability partially influence the viscous resistance of the flow, which creates more sensitive signatures in the geoacoustic parameters. However, when dealing with $ka \approx \mathcal{O}(1)$, even the actual morphology of the grain must be taken into account (Yang & Seong 2018).

Such acoustic parameters begin to exhibit variations in the transition regime up to the short-wavelength regime, in contrast to the non-variational behavior observed in the long-wavelength regime. This phenomenon is well known and widely documented in the literature.

Theoretical attenuation values assuming perfectly rounded spheres are significantly less than the experimental ones, highlighting the influence of roughness on acoustic attenuation values for a regime not far less than $ka < 1$.

As presented before, when particles are much smaller than the wavelength, the system satisfies the Rayleigh long-wavelength condition. In this regime, the estimation of particle size is often preferred over the intermediate and short-wavelength ranges due to reduced sensitivity to particle shape and the ease of theoretical analysis (Dukhin 2002). However, while this simplifies the acoustic modeling, it also limits the number of variables available for material characterization. This is the case in our study, where the goal is to correlate geoacoustic parameters with the physical properties of the sediment.

The model of sediment as a viscous fluid (long-wavelength) serves as a first-order approximation, which can be useful for describing the overall acoustic behavior of many sediments. However, this approach has limitations when it comes to accurately predicting acoustic properties, such as sound speed, based on the physical characteristics of the sediment. Moreover, it does not account for the origins or magnitude of the acoustic damping observed in the sediment (Dunlop 1988).

Williams *et al.* 2002 presented comparisons between measured sound speed and attenuation in a sandy sediment and predictions from Biot's theory. He claimed that for the frequency range analyzed $125Hz - 400kHz$ sound speed dispersion was well captured by Biot's theory, indicating good agreement with the experimental data following the positive velocity dispersion observed in Fig.2.1(a). Attenuation predictions deviated at higher frequencies, possibly due to scattering from volume heterogeneity or shearing at grain contacts.

In contrast, Lee *et al.* 2007 observed a significant negative dispersion in the frequency range of $300kHz - 1MHz$, where Biot's model predicts a slightly positive dispersion. Multiple authors have reported similar findings, indicating that Biot's theory does not accurately describe high-frequency sandy systems above approximately $400kHz$.

For this work, we focus on high frequencies, specifically in the range of $ka \approx \mathcal{O}(1)$, to better understand the microstructural behavior of barite compaction. A more detailed analysis of the barite structure and the rationale for selecting this frequency range will be presented in Sec. 3.2.2. To accurately capture the acoustic behavior at these frequencies, models capable of describing the underlying physics of this regime are required.

Biot-Stoll's theory begins to lose accuracy for coarse sandy sediments at frequencies

around $400kHz$, but this threshold may extend for barite due to its smaller nominal grain size. The reduced particle size shifts the *ka* parameter closer to the long-wavelength regime at the same frequency, potentially mitigating some of the inaccuracies seen in sandy sediments. However, for a barite-based system with $ka \approx \mathcal{O}(0.1)$, the emitted wave must operate in the megahertz range. This places the analysis in a frequency regime where the Biot-Stoll model is no longer reliable, underscoring the need to explore alternative models for wave propagation in granular media.

Alternative models for acoustic wave propagation in sediments have been developed, simplifying the sediment by approximating it as a fluid (Buckingham 1998; Williams & Jackson 1998). One notable example is Buckingham's dissipative fluid-based model, designed to explain attenuation trends observed in experimental data that deviate from predictions made by Biot-type models. This approach assumes that the framework of unconsolidated grains lacks shear rigidity, with energy losses attributed to intergranular friction.

The Biot-Stoll theory and the Buckingham dissipative fluid-based model also break down in the "low frequency" regime, as observed in the sediment acoustics experiments conducted in 1999 and 2004. Referred to as *SAX99* and *SAX04*

Summarizing, over the past few decades, experimental data has increasingly deviated from the predictions of the Biot-Stoll model, particularly at both low and high frequencies (below $20kHz$ and above $400kHz$) (Argo 2012). In response, researchers have developed alternative models to improve experimental agreement across all wavelength regimes.

2.3 Theoretical Alternatives

Although there are several modeling approaches for describing the behavior of acoustic waves in water-saturated granular sediments, none can reliably predict both the speed and attenuation of sound across a wide frequency range. Consequently, there is no universal agreement regarding the validity or superiority of any particular model (Argo 2012).

Chotiros & Isakson 2008 introduced a modification to the Biot model to account for fluid motion perpendicular to the wave propagation direction, commonly referred to as squirt flow. This mechanism was developed to represent grain contact behavior in water-saturated sediments, where the grain contact is modeled as a spring and the surrounding fluid is represented as a spring-dashpot system. The model suggests that fluid flow between grains (squirt flow) influences the high-frequency behavior of the frame moduli. Furthermore, Chotiros & Isakson 2004

incorporated viscous drag at grain contacts alongside shear drag and squirt flow mechanisms to refine the understanding of acoustic wave propagation in granular media.

In Biot's original model, the flow of viscous fluid through the pores was assumed to follow a Couette flow profile. However, this assumption becomes invalid when the fluid boundary layer occupies a significant portion of the pore space, requiring a more complex flow profile. This frequency-dependent correction is incorporated into the shear modulus and depends on the thickness of the fluid film between the sediment grains. Thinner fluid layers deviate further from the Coettue flow, leading to greater discrepancies with the predictions of the original Biot-Stoll model.

This modification of the shear modulus reduces the wave speed at frequencies above the shear relaxation frequency, while the attenuation remains largely unaffected. In particular, this adjustment introduces significant changes in the behavior of the fast wave, as the relationship between sound speed and frequency transitions from an asymptotic trend to negative dispersion, a phenomenon not predicted by either the Biot or Biot-Stoll models (Argo 2012).

Chotiros' approach highlights that simplifications of the Biot-Stoll model can effectively retain predictive accuracy in specific contexts while reducing computational complexity. It demonstrates how researchers adapt theoretical models to focus on dominant mechanisms, such as fluid flow and intergranular interactions, rather than over complicating with parameters that may have negligible effects in certain scenarios.

The methods discussed earlier focus primarily on the application of Biot theory to sandy sediments. However, Leurer 1997 proposed a squirt flow model specifically designed for fine-grained sediments, such as barite. In this framework, fluid movement occurs within water layers formed by the swelling of clays, as well as in the remaining pore spaces. This interaction generates a grain modulus that is frequency-dependent, capturing the distinct acoustic behavior of fine-grained sediments.

Lee *et al.* 2007 reported that, in their experiments, wave velocity in the frequency range of $0.3 - 1MHz$ contradicted the predictions of both the Biot-Stoll model and Buckingham's GS model; however, it aligns more closely with the predictions of multiple scattering models Schwartz & Plona 1984, which explain the negative dispersion observed in a glass-grain composite. These models agreed well with experimental data for water-saturated sandy sediments. It is worth noting that significant wave velocity dispersion, while evident in this case, was neither well understood nor widely accepted prior to the 1990s (Argo 2012).

In the same work, Lee *et al.* 2007 collected experimental data for the attenuation coefficient that revealed a nonlinear increase with frequency in the range of $0.3 - 1.0MHz$. In contrast, both the Biot and GS models predicted a nearly linear increase in the attenuation coefficient with frequency. When the total attenuation coefficient was calculated as the algebraic sum of the absorption and scattering components, it showed a reasonable agreement with the experimental data across the entire frequency range. Their study concluded that scattering is the dominant mechanism responsible for frequency-dependent variations in phase velocity and attenuation coefficient in water-saturated sandy sediments at high frequencies.

In addition, attenuation and group speed measurements for water-saturated granular materials, including natural sand and glass beads, were also presented by Hare & Hay 2018 in the frequency range of 1.0 to $1.8MHz$. The grain diameters ranged from 219 to $497\mu m$, corresponding to $ka \approx 1$, placing the materials in the scattering regime. These measurements were taken for various sediment thicknesses resting on a reflective surface, using monostatic geometry. The attenuation and wave velocity estimates closely matched high-frequency experimental results and the predictions of multiple scattering theory

Ohkawa 2006 reported a strong agreement between the attenuation data $SAX99$ and the calculated attenuation coefficient, which was determined as the algebraic sum of the absorption and scattering components. The absorption attenuation, following the $f^{1/2}$ dependence, as predicted by the Biot model, corresponds to the viscous dissipation of the pore fluid. The scattering attenuation, on the other hand, was modeled using the empirical f^2 dependence, which was derived by fitting experimental data for water-saturated fine sands with a mean grain diameter of $230\mu m$, as measured by Seifert 1999.

2.4 Theoretical understanding of the compaction correlation

Numerous studies conducted over several decades to understand and predict the behavior of geoacoustic properties across various types of oceanic sediments and frequency ranges provide a solid foundation for interpreting and predicting the experimental data presented later in this work, as will be further discussed in Sec. 4.

Hare & Hay 2018 gathered valuable data on the attenuation acoustic behavior of various types of granular sediments, as shown in Fig.2.2(b), covering a broad range of frequencies, attenuation values and comparing these findings with model predictions. The data gathered in their work fall within the dashed data presented in Fig. 2.2. Their study provided critical insights

into the influence of sediment compaction on wave behavior, serving as a foundational reference for advancing the understanding of high frequency acoustic wave propagation in granular media.

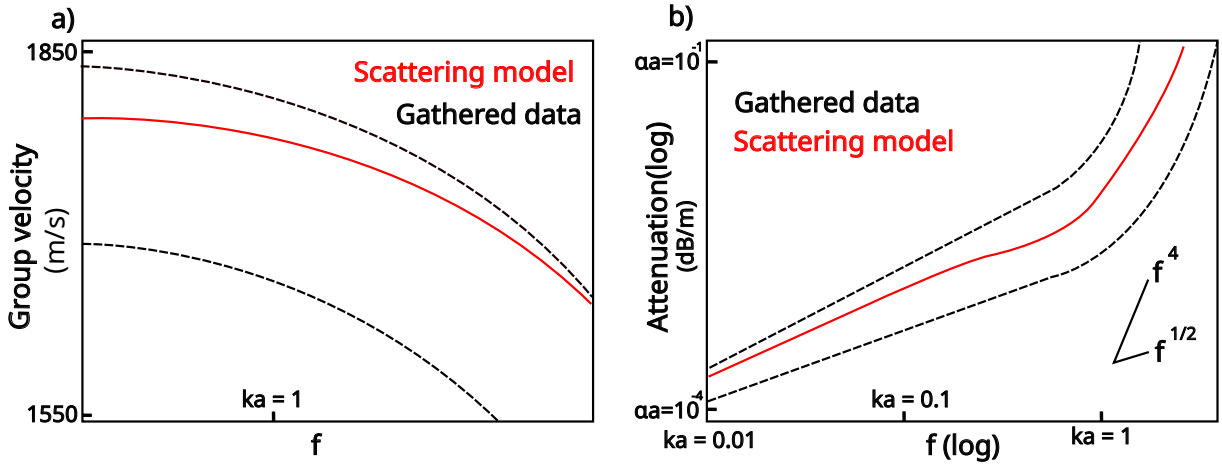

Figure 2.2 – Wave velocity (a) and attenuation (b) for high frequencies. Reference: Adapted from Hare & Hay 2018.

For instance, the increasing relationship between attenuation and frequency, ranging from $f^{1/2}$ to f^4 as observed by Hare & Hay 2018, can serve as a good indicator of different compaction levels. As the sediment compacts, its pore size decreases, resulting in lower porosity. Argo 2012 observed that the attenuation for $289\mu m$ beads demonstrates a frequency dependence ranging from approximately $f^{2.75}$ at lower porosities to $f^{1.75}$ as porosity increases. Similarly, $549\mu m$ beads show a frequency dependence that changes from $f^{3.5}$ at low porosity to $f^{2.75}$ at higher porosity. Of course, these values may vary depending on the type of sediment and other parameters. However, a thorough understanding of these attenuation dependencies is a powerful tool for characterization tasks, which is the primary aim of this work.

The Velocity dispersion can also serve as a useful indicator Fig.2.2(a), as it reflects changes in the bulk modulus and rigidity of the sediment, which are influenced by varying levels of compaction. As the sediment compacts, its internal structure becomes more consolidated, leading to alterations in the way waves propagate through the material. This variation in the acoustic wave velocity with frequency can thus provide valuable information on the sediment's compaction state and the associated changes in its physical properties, as made by Argo *et al.* 2011.

Argo *et al.* 2011 investigated the frequency dependence of wave velocities while varying the porosity of glass beads. Their study revealed an increase in wave velocity with greater compaction, due to the increase in the volume concentration of high sound speed

particles, highlighting the direct relationship between sediment structure and acoustic properties. Furthermore, they observed the phenomenon of negative dispersion at higher frequencies, which supports the findings of Hare & Hay 2018; Kimura 2011; Lee *et al.* 2007.

The importance of high-frequency measurements of attenuation and wave velocity to understanding the internal structure of granular media, such as sedimented barite compaction, is evident and will be further explored throughout this dissertation. This literature review serves as foundation for the analyses and insights presented in Sec.4.

Building on this foundation, the next chapter will describe the methodology employed for these measurements. It will detail the experimental setup, data acquisition protocols, and signal processing techniques used to achieve the desired data determining wave attenuation and wave velocity.

3 METHODOLOGY

Studies of experimental procedures to obtain acoustics properties gained attention in the academy in the same manner as the acoustics theories discussed in the Literature Review Sec.2. In the earlier 20th century, during an increasing stress that led the world into two global wars, several authors started to create experimental setups to attain wave attenuation and velocity.

Since then, numerous methods popped up in the industry and in the academy, all of them being improved over the decades. Nowadays, thanks to this effort, there are two major experimental acoustic setups, one using resonance tubes or cavities with continuous waves and the other using pulsed waves in several apparatus layouts. Usually, continuous waves are applied for a low frequency range, in the units of kilo Hertz, partly because of the difficulty of creating a setup layout for the measurement of a pulsed wave with wavelength in the order of meters. The pulsed wave methods are usually applied for higher frequencies, ranging from dozens of kilo Hertz to units of mega Hertz (Argo 2012).

Given the objective of this study, outlined in Sec.1 and theoretically explained in Sec. 2, the target frequency falls within the megahertz range. Based on trends in the literature, pulsed wave techniques were chosen.

Pulsed wave ultrasound characterization offers a wide range of procedures and setups, utilizing three, two, or even a single transducer.

One objective of this dissertation, beyond acoustically characterizing barite compaction, is to demonstrate the potential application of an alternative method for acoustical characterization of wet granular media, one that, to the best of the authors' knowledge, has not yet been utilized in the literature. To achieve this, wave velocity and attenuation measurements were conducted using the pulse-echo procedure, as made by McClements & Fairley 1992 based on Papadakis 1968. This method, which employs a single transducer in a rigid cell setup, is widely applied for characterizing solids, liquids, and emulsions. A detailed discussion of this approach is provided in Sec.3.1.2.2.

This section presents two acoustic measurement techniques, highlighting the advantages of single-transducer approaches, such as the pulse-echo method. This technique offers a simplified setup while effectively avoid many errors commonly addressed by more complex techniques, such as Buckingham's approach. Additionally, potential reasons for the limited use

of single-transducer methods in sedimentary acoustical measurements will be discussed.

The mentioned variety of techniques available to extract information from the compressional waves, which in our case is used to investigate the properties of marine sediment compaction, are all grounded on the same fundamental principles: detection of an acoustic wave from a source, before the contact with the sample, followed by the wave interaction with the sample and its detection by a receiver after the contact.

3.1 Techniques for measuring acoustic properties.

Before discussing the possible methods with different transducer layouts and their advantages, it is important to highlight a procedure common to all the methods later presented here: the frequency-domain approach, specifically the Spectral Ratio Method SRM.

3.1.1 Domain analysis and processing

In order to extract useful information from the acquired echo signals, as shown in Fig. 3.1, these signals must undergo processing. The subsequent processing involves comparing the emitted and received pulses to extract information about the compressional wave properties. From the temporal and amplitude characteristics of the measured echo signals, we can derive information about the sediment's sound speed and attenuation. With the growing number of studies on this subject, it is now possible to analyze waves in both the frequency and time-domain. Time-domain methods include techniques such as amplitude decay, rise time and wavelet modeling. However, frequency-domain methods, particularly sound spectroscopy, are the most widely used. These methods include techniques such as spectral ratio, matching technique, and spectral modeling. Tonn 1989 discusses these methods, along with their advantages and limitations in various applications aiming at the seismic quality factor Q measurement.

For this work, the Spectral Ratio Method was selected due to its favorable performance in comparison studies and the abundance of related literature. This method involves applying the Fast Fourier Transform *FFT* to both emitted and received acoustic waves, using magnitude and time shifts to extract acoustic properties. A broadband pulse was chosen alongside the *FFT* algorithm for its efficiency compared to measuring attenuation at discrete frequencies. Widely applied in studies of acoustic attenuation and wave velocity in marine sediments Hare & Hay 2018; Buckingham & Richardson 2002; Sessarego *et al.* 2008, the Spectral Ratio Method has also been used for suspensions and emulsions Silva 2020. Here, the power

spectrum ratio technique will be employed, extracting the power spectrum from two received echoes, as illustrated in Fig. 3.1.

The power spectrum is given by the following equation:

$$A_{1\&2}(f) = |FFT(p_{1\&2}(t))|^2, \tag{3.1}$$

where $p_{1\&2}(t)$ are the received signals in the time domain from both echoes 1 and 2, as shown in Fig.3.1 and Fig.A.1. To simplify the equations below, domain information will be omitted to avoid cluttering the notation.

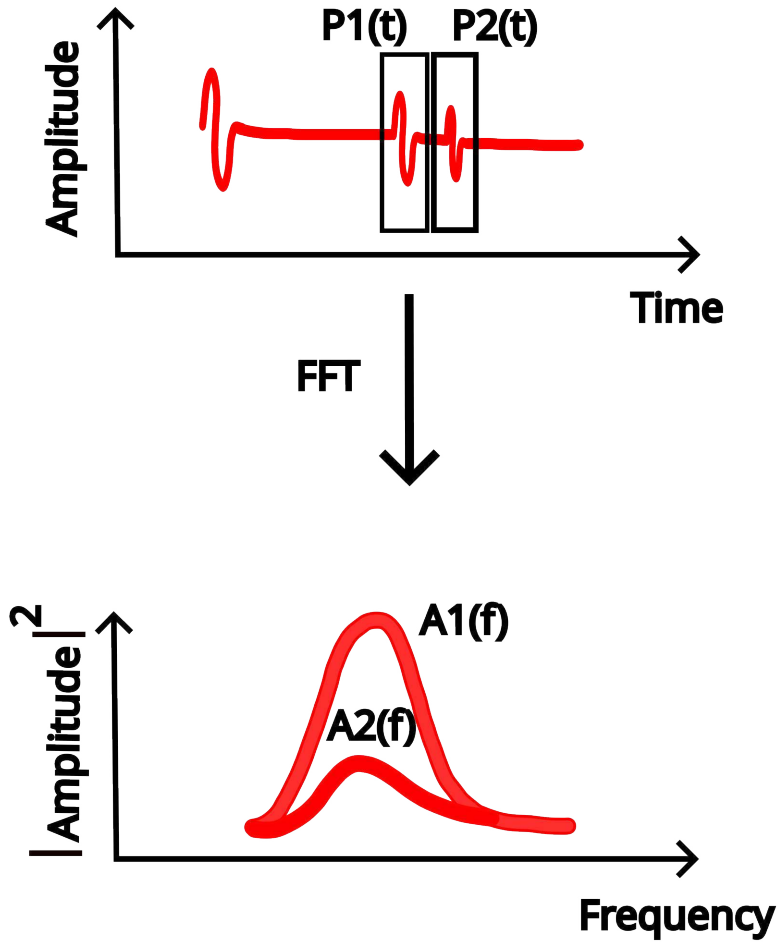

Figure 3.1 – Spectral analysis procedure.

To reliably determine the dependence of compressional wave properties on frequency and sediment compaction, the chosen technique must allow for precise measurement of the wave

properties within a controlled sediment volume, emphasizing the importance of selecting the appropriate method.

3.1.2 Wave attenuation processing

For wave attenuation measurement in sediments, the broadly utilized approach is using two transducers, one acting as an emitter, and the other one acting as a receiver (Kimura 2011; Argo 2012; Yang & Seong 2018; Lee *et al.* 2009). However Buckingham & Richardson 2002 stated in his work the advantages of using three transducers instead of two, the receiver-receiver approach.

Trying out the possibility of different numbers of transducers that can be applied, the present work focused its measurements using only one transducer, as said before. Which was popularized first by Nolle *et al.* 1963 and in a later work by Hare & Hay 2018, where the latter analyzed the applicability of scattering models in marine sediments. Although this is rarely used in sediment characterization, the pulse-echo method is well understood and broadly applied in ultrasonic measurements for liquids and emulsions (Silva 2020).

Initially, Buckingham's approach will be presented, since the authors claimed that their method improves data quality compared to the widely applied two-transducer technique. And furthermore the Papadakis method will be presented and compared with Buckingham's approach, highlighting their respective advantages and disadvantages, and demonstrating how the former can also be applied for this task using a more cost-effective approach.

3.1.2.1 Buckingham's approach

All the techniques require two measurements, before and after the wave passes throughout a specified sample length. If the two transducers considered are a source-receiver pair, this technique does not account for changes in the wave shape between the emitted acoustic pulse, and the received pulse by the sample. These differences arise from the varying coupling impedance between the transducer and the two different media, water and sediment, resulting in distinct shapes of the acoustic pulses emitted in each medium (Buckingham & Richardson 2002).

If two receivers are considered, as noted, the wave shape changes arising from the impedance mismatch won't need to be accounted for, only the dissipation and dispersion degree of the acoustic pulse; properties which depend only on the separation of the receivers and compressional wave properties of the sediment.

Their approach also uses water as the calibrant medium, this water-column is necessary to eliminate amplitude mismatch between the receivers and account for the geometrical spread losses. As will be seen below in Eq.3.5, when we subtract the water attenuation from the sediment attenuation, it doesn't change its value due to the extremely low attenuation of the water, allowing us to cut out these losses terms due to the natural logarithm propertie $ln(sediment) - ln(water) = ln(\frac{sediment}{water})$. Consequently, the geometrical spread and amplitude mismatch errors in both water and sediment will be removed due to their presence in the numerator and denominator.

One limitation of the above technique, irrespective of the transducers selected, is the assumption that spreading losses in the sediment and water are the same. If these media possess different velocities this will not be the case, and the calculated attenuation coefficient will be incorrect; however, this error isn't significant in comparison to the level of precision required for this study.

Buckingham's approach uses a box filled with pure water and water-filled sediment, which in our case would be barite. We can see the apparatus utilized by Buckingham & Richardson 2002 in Fig. 3.2.

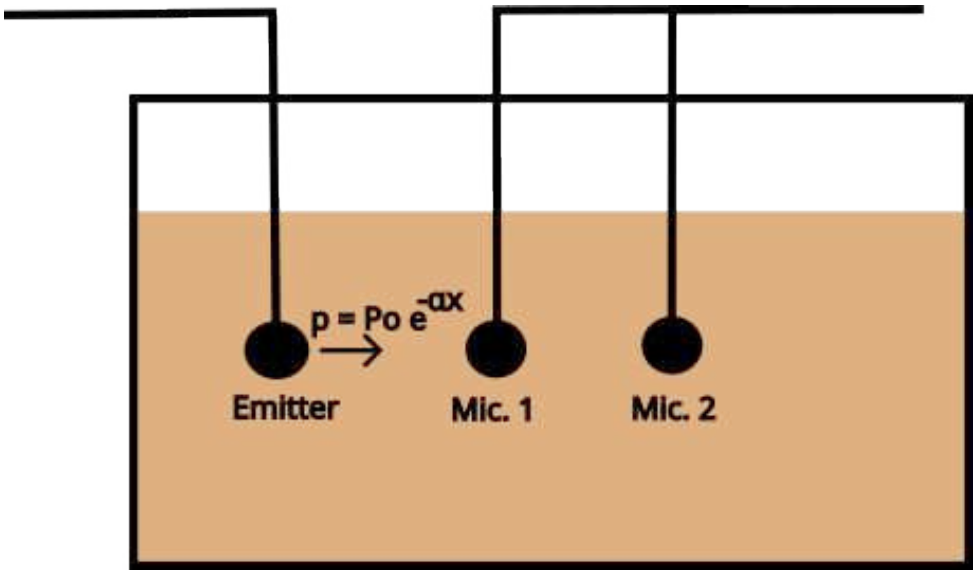

Figure 3.2 – Three transducer layout made by Buckingham & Richardson 2002.

Using the solution of the lossy wave equation Eq.1.7 presented in section Sec.1.2, the equation for attenuation α can be developed in an explicit form. Therefore, assuming B as the power spectrum of the wave received by the receiver-transducers Eq.3.1, we have:

$$B_2 = B_1 e^{-\alpha_{2,s} l}, \tag{3.2}$$

$$\alpha_{2,s} = -\frac{1}{l} ln \left(\frac{B_{2,s}}{B_{1,s}} \right), \tag{3.3}$$

with the subscripts 1 and 2 being $Mic.1$ and $Mic.2$ respectively, and l being the distance between the receivers. The same way, using water as a reference:

$$\alpha_{2,w} = -\frac{1}{l} ln \left(\frac{B_{2,w}}{B_{1,w}} \right). \tag{3.4}$$

As previously discussed regarding diffraction and mismatch corrections, subtracting Eq.3.4 from Eq.3.3, yields the corrected attenuation:

$$\alpha_2 = \frac{1}{l} ln \left(\frac{\frac{B_{2,w}}{B_{1,w}}}{\frac{B_{2,s}}{B_{1,s}}} \right). \tag{3.5}$$

By following the latter approach, no specific form of the spreading law needs to be assumed, as will be demonstrated in Papadakis' case. Nevertheless, one disadvantage of the method proposed by Buckingham & Richardson 2002 is the reliance on multiple transducers, which can pose significant challenges for some researchers.

As will be seen next, the approach made by Papadakis 1968 allows us to use only one transducer and also avoid the same errors as the three transducer method.

3.1.2.2 Papadakis' method

The method utilized in this work, originally introduced by Papadakis 1968 in 1968, was developed to measure the attenuation of solids and the reflection coefficient at the buffer–sample interface. Over time, it has also been successfully adapted for the use in fluids and emulsions (McClements & Fairley 1992), and now in this work, for sediments. This technique employs a single transducer operating in pulse-echo mode, utilizing the power spectrum A of first two echo signals generated by reflections at the buffer–sample A_1 and sample back-wall A_2 interfaces. Along this dissertation the first and second echo will also be called entry and back-wall echo respectively.

As shown in Fig. A.1, and more clearly in Fig. 3.1, the first step is to isolate the two Gaussian pulses from the main signal received by the oscilloscope. One approach employed in this study was using water as a reference. By first characterizing the echoes in water, the same

time window was then applied to remove the corresponding echoes when using barite as the sample.

Figure A.1 illustrates both the entry and back-wall echoes for barite and water, allowing a direct comparison of their acoustic responses.

In Fig.3.3 we can see a flowchart representing the signals emitted and received using Papadakis' approach.

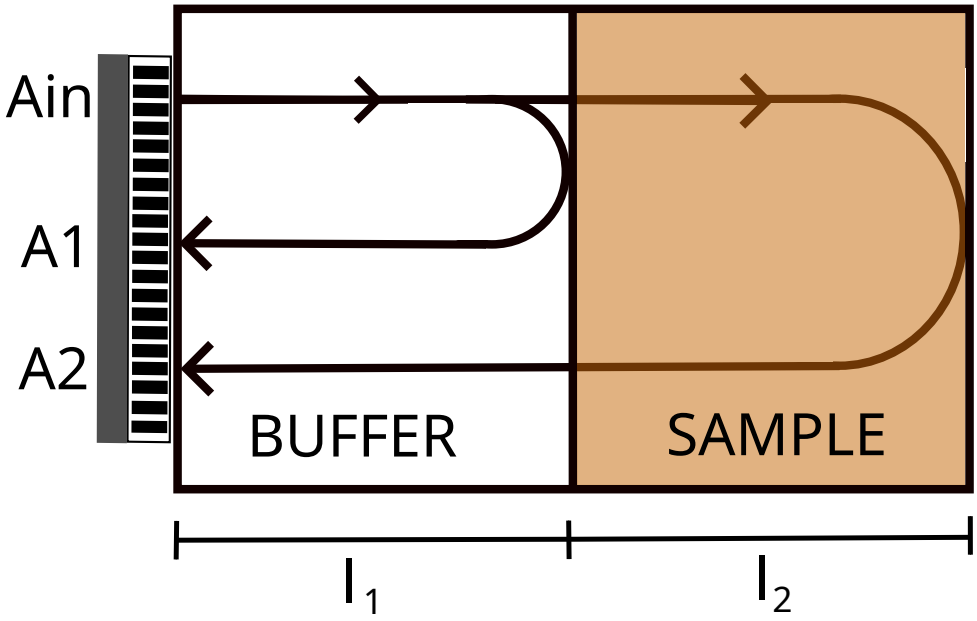

Figure 3.3 – Pulse echo method based on Papadakis 1968.

As made in the Buckingham's method, from the solution presented in Eq.1.7 we can analyze the attenuation of the sample by looking at the echoes and transmitted pulses from the given system, as follows:

When transmitter A sends a Gaussian pulse A_{in}, it goes throughout the buffer rod and hits the interface between it and the sample, suffering a R_{12} reflection, so the total energy of the pulse will be partially reflected back to the emitter and the other part will be transmitted through the sample. Based on it, the first echo A_1 obtained by the transducer will be:

$$A_1 = A_{in} R_{12} D_1 e^{-2\alpha_1 l_1}. \tag{3.6}$$

The first received echo A_1 is equal to the incident wave A_{in} reduced by the amount of transmitted energy to the sample R_{12} and the energy attenuated while propagating through the buffer rod $e^{-2\alpha_1 l_1}$ (two times the rod's length). D_1 is a parameter utilized to account for

the diffraction error due to the plane wave propagation assumption made in Sec.1.2, and will discussed deeply later on in Sec. 3.2.4.2.

For the second echo A_2 on transducer A, part of the A_{in} energy which is not reflected at the buffer rod/sample interface (the A_1 echo) goes through the sample. Knowing that the acoustic energy at the interface can be represented as $R + T = 1$, which means that the wave energy is only reflected or transmitted at the interface, we can rewrite it like $T = 1 - R$. Hence, instead of multiplying Eq.(3.6) by R_{12}, it is multiplied by $1 - R_{12}$, representing the energy that passes through the interface buffer rod/sample.

Subsequently, the wave goes throughout the sample, hits the back-wall/sample interface, and reflects back towards the transducer A, this reflection can be mathematically represented as R_{23}. When the reflected wave from the back-wall/sample interface passes through the buffer rod/sample interface again, but this time in the opposite direction, the reflection coefficients in both directions can be assumed as equals in magnitude, validating the relation $R_{12} = -R_{21}$. Since the transmission coefficient for the ingoing wave is $1 - R_{12}$ and for the outgoing wave is $1 - R_{21}$, their product yields an energy coefficient of $1 - R_{12}^2$, representing the energy of a wave traveling in and out of the sample in R_{12} mean.

But first, for better visualization, the second echo A_2 can be represented in function of the transmitted *T* and reflected *R* coefficients as in Eq.3.7:

$$A_2 = A_{in} T_{12} R_{23} T_{21} D_2 e^{-2\alpha_1 l_1} e^{-2\alpha_2 l_2}. \tag{3.7}$$

As explained before, A_{in} represents the total energy sent by the emitter. The terms T_{12} and T_{21} are the transmission coefficients at the buffer rod/sample interface, which can be expressed as $1 - R_{12}^2$. The parameter R_{23} denotes the energy reflected at the back-wall of the sample. The term D_2 accounts for wave diffraction for the buffer and sample path. Finally, $e^{-2\alpha_1 l_1}$ and $e^{-2\alpha_2 l_2}$ represent the wave attenuation in the buffer rod and the sample, respectively.

This leads to the equation for the second echo, on transducer *A* expressed solely as a function of the reflection coefficients:

$$A_2 = A_{in} R_{23} (1 - R_{12}^2) D_2 e^{-2\alpha_1 l_1} e^{-2\alpha_2 l_2}. \tag{3.8}$$

It is important to keep in mind that the goal is to analyze the acoustic information solely using the received signals on the oscilloscope. This implies that in the Eq.3.8, R_{12} and R_{23}, must be known in advance.

The representation of the actual data obtained by this method can be seen in Appendix A.

3.1.2.2.1 Buffer rod and back-wall made of the same material

For this dissertation, both the buffer and back-wall are made of the same material: polyvinyl chloride. An important advantage of this approach is that it eliminates the need to know the acoustic properties of the buffer and back-wall, as will be demonstrated below. In the next section Sec.3.1.2.2.2, the use of two different materials will be introduced.

If the back-wall and the buffer rod were made of the same material, we can assume $R_{23} = R_{12}$. This way we would reformulate the expression Eq.3.8 for all reflection coefficients in function of R_{12}:

$$A_1 = A_{in} R_{12} D_1 e^{-2\alpha_1 l_1}, \tag{3.9}$$

$$A_2 = A_{in} R_{12} (1 - R_{12}^2) D_2 e^{-2\alpha_1 l_1} e^{-2\alpha_2 l_2}. \tag{3.10}$$

Now, to obtain the reflection coefficient R_{12}, several authors have proposed numerous methods within the literature. However, in this work, the relative reflection method ***RRM*** described by Adamowski *et al.* 1995 will be employed. Adamowski *et al.* 1995 proposed the use of a reference sample, specifically air, due to its lower acoustic impedance in comparison with the buffer rod solid material. Since the buffer rod has a higher impedance compared to the air, its reasonable to infer that the reflection coefficient on the interface is $R_{\text{ref}} = -1$ for all frequencies present within the pulse sent. If another sample was utilized, with a acoustic impedance similar to the buffer material, the relation between the buffer and the sample reflection coefficient R along the frequency utilized must to be known.

Under this assumption, the entry-echo amplitude A_1 is first measured using air, where it is referred to as A_{ref}. Subsequently, the entry-echo amplitude A_1 is measured with the unknown sample, whose physical and acoustic properties are being investigated. The reflection coefficient at the interface between the buffer rod and the sample R_{12} is calculated by the ratio of the amplitudes of the entry-echoes from the second and first measurements. So, we can write the following equations:

$$A_{ref} = A_{in} R_{ref} D_{ref} e^{-2\alpha_1 l_1}, \tag{3.11}$$

$$A_1 = A_{in} R_{12} D_1 e^{-2\alpha_1 l_1}, \tag{3.12}$$

making the ratio between the echoes, and isolating R_{12} :

$$R_{12} = R_{ref} \frac{A_1}{A_{ref}}. \tag{3.13}$$

Since $D_{\text{ref}} = D_1$, these terms cancel out in the fraction. The same applies to the attenuation using air and the sample, as the buffer remains unchanged, causing the term $e^{-2\alpha_1 l_1}$ to cancel out as well. Consequently, neither the diffraction error nor the buffer properties affect the energy ratio. Since we know that $R_{ref} = -1$, we can obtain R_{12} only with the collected data from the oscilloscope. This vector of R_{12} is in function of frequency and will also be used for the procedure in which utilizes different materials for the measurement cell Sec.3.1.2.2.2.

With the equations Eq.3.9 and Eq.3.10 we are able to develop a simple equation that relates the echoes amplitudes with the sample attenuation α_2. Making the ratio between A_1 and A_2, we yield to the following relationship:

$$\alpha_2 = \frac{1}{2l_2} ln \left(\frac{A_1(1 - R_{12}^2) D_2}{A_2 D_1} \right). \tag{3.14}$$

3.1.2.2.2 Buffer rod and back-wall made of different materials

If two types of materials were selected, one for the buffer rod and another for the back-wall, the assumption $R_{12} = R_{23}$ made in Sec.3.1.2.2.1 is no longer valid. Why the use of one or two materials and their advantages will be discussed later in Sec. 3.2.2.

In this case, the acoustic properties of the materials used for both the buffer and back-wall must be known. Since for this work the same material was utilized, for future studies we'll explore the use of two different materials, Acrylic and Stainless Steel, to address certain issues encountered in the setup used for this dissertation (Sec. 3.2.3 and Appendix B).

For different materials, we know beforehand that a crystal Acrylic acoustic impedance is around $Z_{acrylic} = 3.245 \pm 0.005 \times 10^6 kgm^{-2}s^{-1}$, at 20^oC. In addition, the impedance of the Stainless Steel back-wall also must be known beforehand, and according to Ultrasonic Testing (Nondestructive Testing Handbook) Amazon Website its value is around $Z_{steel} = 45.45 \times 10^6 kgm^{-2}s^{-1}$ at 20^oC.

As made previously in Sec.3.1.2.2.1, R_{12} is obtained by the equation Eq.3.13. However, to yield to R_{23}, we need to follow the methodology made by McClements & Fairley 1992;

McClements & Fairley 1991 which is based on Kinsler *et al.* 2000. For this task, we know that we can correlate the acoustical impedance with the reflection coefficient for a plane wave using the expression Eq.3.15:

$$Z_2 = \frac{Z_1(1-R)}{1+R}, \tag{3.15}$$

in which the subscripts 1 and 2 are the first and second media in which the wave goes through.

In our case, when the wave goes through the buffer rod to the sample, $Z_1 = Z_{acrylic}$ and $Z_2 = Z_s$, when it goes from the sample to the back-wall, $Z_1 = Z_s$ and $Z_2 = Z_{steel}$.

With the assumption of plane wave propagation through flat interfaces, we can derive equations that lead to the back-wall reflection coefficient, R_{23}.

Since our barite sample has unknown properties, with the equation Eq.3.15 we are able to obtain its acoustical impedance:

$$Z_s = \frac{Z_{acylic}(1-R_{12})}{1+R_{12}}, \tag{3.16}$$

and consequently the reflection coefficient at sample/back-wall interface R_{23}:

$$R_{23} = \frac{Z_s - Z_{steel}}{Z_{steel} + Z_s}. \tag{3.17}$$

Finally with all this information in hand, the ratio between the equations Eq.3.6 and Eq.3.8 can be made to yield the attenuation using different materials:

$$\alpha_2 = \frac{1}{2l_2} ln\left(\frac{A_1(1-R_{12}^2)R_{23}D_2}{A_2R_{12}D_1}\right). \tag{3.18}$$

This straightforward physical understanding, combined with the cost-effectiveness of the single-transducer approach, makes the latter method the preferred choice for acoustical characterization of granular media compaction in this work. Furthermore, it introduces a new possibility for sedimentary acoustic characterization.

Some disadvantages may arise with the latter approach, namely Papadakis' method, such as the high power required to receive strong back-wall echoes due to the high attenuation characteristics of granular media. Another concern is the ring-down effect on the transducer, which creates a "comet-tail" after the received electrical signal ends, resulting from the energy dissipation delay of the capacitive cells within the transducer. Since the echoes are closely

spaced, this effect can cause subsequent echoes to overlap. Other concerns regarding this method will presented in Sec. 3.2.4. However, as demonstrated in Sec. 4, these issues do not significantly impact the overall trend of the data when compared to literature results obtained with more complex transducer arrays. This showcases the potential applicability of ultrasonic measurement cells for this purpose, extending beyond fluid and emulsion characterization.

3.1.3 Wave velocity processing

When a mechanical wave propagates through a homogeneous media, its phase velocity is constant. The equation that rules the relation between frequency and phase velocity is given by Eq. 3.19:

$$c = \lambda f. \tag{3.19}$$

So, with a double frequency increase, the wavelength will be reduced by twice to maintain the same phase velocity. However, when we are dealing with non-homogeneous media, such as granular ones, each frequency in a broadband propagation pulse behaves in different ways along the medium. This type of attenuation is called wave dispersion due to the envelope deformation which is characteristic of this kind of phenomenon Fig. 3.4.

For a homogeneous medium, when analyzing the pulse in the frequency domain, the pulse shape (envelope) and the carrier position remain unchanged along the propagation path. This indicates that the phase velocity (the propagation speed of the compressional peak) and the group velocity (the propagation speed of the envelope peak) are identical and remain constant (Shin & Hammond 2008). Consequently, the orange short pulse in Fig. 3.4 remains unchanged as it propagates through the medium, as also shown in Fig. 3.5(b).

On the other hand, in a heterogeneous medium, low frequencies interact differently than high frequencies, as the former interacts less with structures exhibiting varying impedance and contacts. When analyzing the pulse in the frequency domain, this behavior becomes evident through envelope deformation and a shift along the frequency axis. Frequently, the envelope peak shifts to lower frequencies due to its reduced attenuation, which also deforms the carrier, altering the pulse shape. In such cases, the phase velocity and group velocity are not equal Fig.3.4 and Fig.3.5(a).

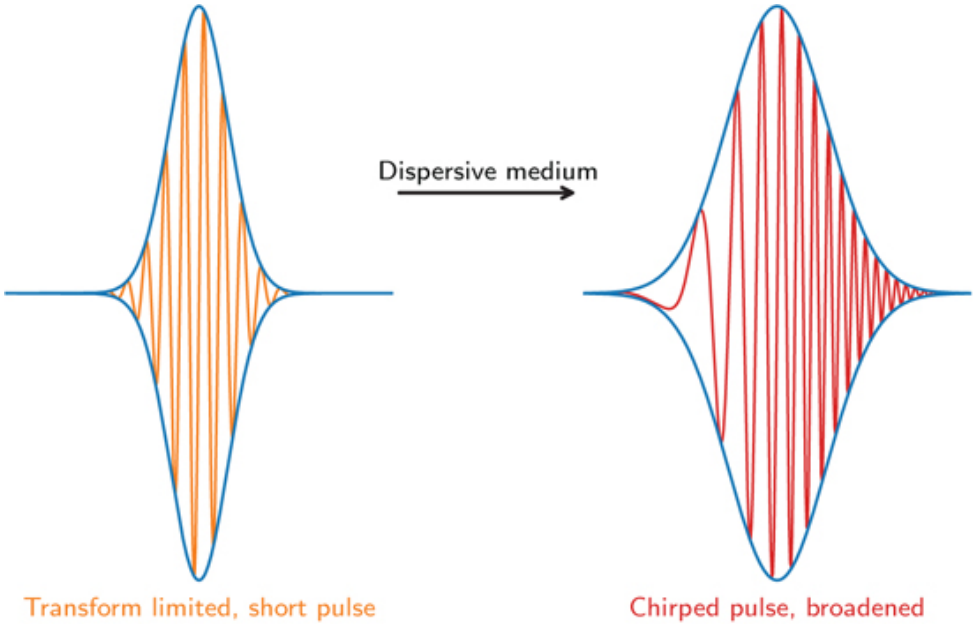

Figure 3.4 – Propagation of a broad-frequency wave group through a dispersive medium (Pickering 2024).

As illustrated in Fig. 3.5(a), the phase delay t_p represents the time delay of each sinusoidal component (carrier), whereas the group delay t_g corresponds to the time delay of the amplitude envelope. These delays are continuous functions of frequency, meaning they can vary across different frequencies. When the group delay deviates from being constant, it reflects the degree of nonlinearity in the phase. In such systems where the group delay is frequency-dependent, each frequency component in the input signal experiences a different delay. Consequently, the output signal's shape differs from the input signal, a phenomenon known as dispersion (Shin & Hammond 2008).

Since velocity is defined as the distance traveled divided by the time taken, the group delay is directly linked to the group velocity of a wave, while the phase delay corresponds to the phase velocity.

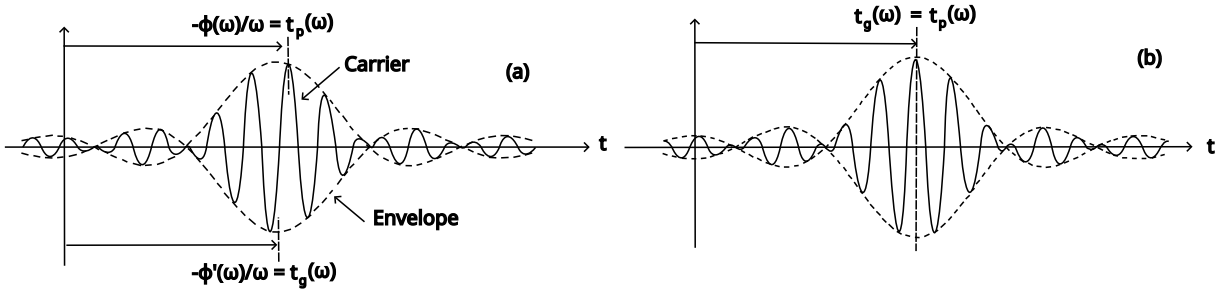

Figure 3.5 – Phase velocity and group velocity characteristics. Reference: (Shin & Hammond 2008)

The methods used here are based on the same geometry presented in Fig. 3.3, so the power spectra A_1 and A_2 represent the entry echo and the back-wall echo, as described in Sec. 3.1.2.2.

The measurement of the group velocity is determined as a function of frequency, looking at the phase difference between the two echoes $\phi_g(f)$:

$$\Delta\phi_g(f) = arg\left(\frac{FFT(p_2(t))}{FFT(p_1(t))}\right), \tag{3.20}$$

the group delay between the first two echoes can be yielded as did by Carlson *et al.* 2003:

$$t_g(f) = \frac{1}{2\pi}\frac{\delta\left(\Delta\phi_g(f)\right)}{\delta f}. \tag{3.21}$$

With the group delay in hands, the group velocity is basically the ratio between the path space and the group delay:

$$c_{g,2}(f) = \frac{2l_2}{t_g(f)}. \tag{3.22}$$

Equation Eq. 3.20 represents the phase difference between the first two echoes, which is also used to calculate the phase velocity. The phase velocity was determined following the approach outlined by Peters & Petit 2003, who developed a simple method for automatic signal processing to avoid ambiguity of the phase shifting when dealing with experimental data. This issue arises primarily from the periodic nature of the phase in Fourier analysis, where the phase is typically constrained within a limited range, usually between $-\pi$ and π. Consequently, the equation used is:

$$c_{f,2}(f) = -\frac{2\pi l_2 f}{\Delta\phi_p(f) - 2\pi f \Delta t_{A_2-A_1}}, \tag{3.23}$$

with $\Delta t_{A_2-A_1}$ being the time of flight *ToF* of the first two echoes. There are several methods for determining the transit time between echo signals to calculate the longitudinal sound velocity in the medium. In this work, the cross-correlation method was used Eq.3.24:

$$C(t) = \int_{-T/2}^{T/2} P1(\tau)P2(t+\tau)d\tau. \tag{3.24}$$

According to Silva 2020; Costa-Júnior *et al.* 2018, the signal obtained through cross-correlation of the two echo signals in the time domain enables the estimation of the transit time Δt (*ToF*) by identifying the location of the maximum amplitude within the resulting vector Fig.3.6.

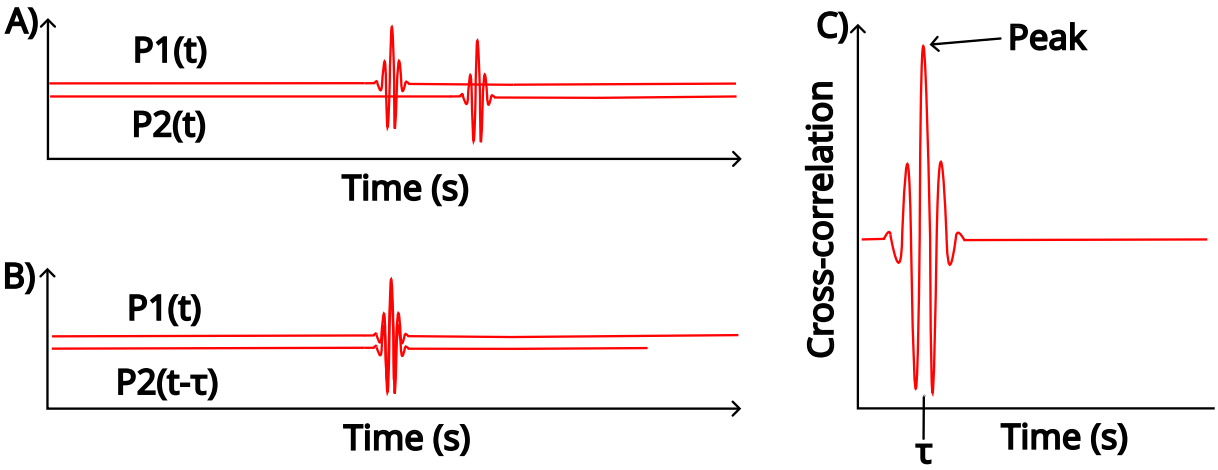

Figure 3.6 – Phase delay between pulses through Cross-correlation.

In a homogeneous medium like water, a distinct peak appears at a time τ, corresponding to the pulse's time of flight. This peak is well-defined because water is a non-dispersive medium, meaning all frequency components of the pulse travel at the same speed, resulting in minimal distortion. However, in a dispersive medium, where pulse distortion is significant, this peak is accompanied by leakage in the cross-correlation data.

For the calculation of the longitudinal wave speed throughout the buffer and sample instead of its analyze in the frequency domain, the following equations can be used:

$$c_1 = -\frac{2l_1}{\Delta t_{A_4-A_1}}, \tag{3.25}$$

$$c_2 = -\frac{2l_2}{\Delta t_{A_2-A_1}}, \tag{3.26}$$

with A_1 being the power spectrum Eq.3.1 of the entry echo, A_2 the back-wall echo, and A_4 being the second reflection of the entry echo inside the buffer rod.

3.2 Design of the experimental setup

All the equations needed for the methods presented previously in this work assumes a plane wave propagation through an infinite media, without wall effects, propagation constraints, and wave interactions, which is nearly impossible to replicate perfectly in small apparatus within the laboratory walls. It's worth pointing out that assuming a plane wave propagation, only a compressional wave is present, often called a P-wave. Hence, the creation of shear waves or low-velocity compressional waves (Biot's waves) in the laboratory measurements, increases the overall measurement error. Based on it, all the steps made here were trying to reduce such errors, as will be specified in each of the steps below.

3.2.1 Ultrasonic measurement cell geometry

On Fig. 3.7 we can see the photo of the ultrasonic measurement cell, which is filled with the sample under investigation, in our case, barite.

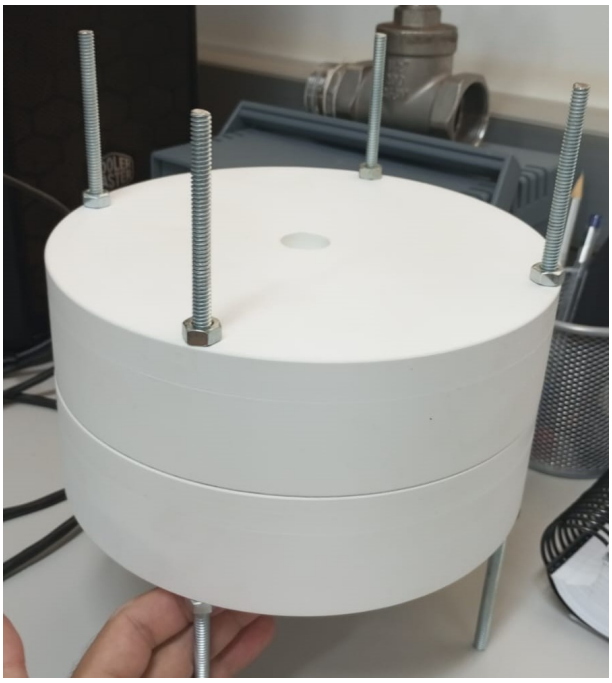

Figure 3.7 – Photo of the ultrasonic measurement cell utilized in this work.

For a better understanding of the propagation fields and the acoustic wave interaction with different interfaces, a schematic representation was made in Fig. 3.8.

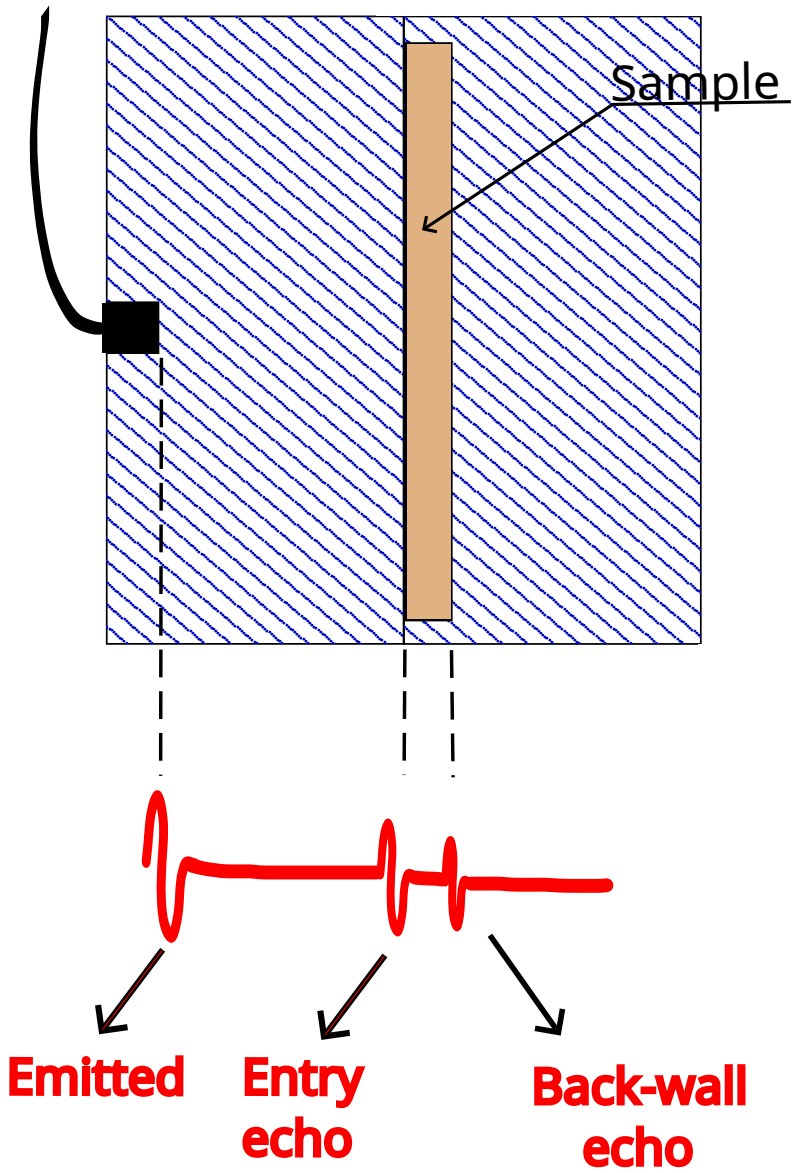

Figure 3.8 – Ultrasonic measurement cell schematics. The type of data captured by the oscilloscope is represented in red.

As explained previously, for this dissertation, the same material approach was utilized, the blue hatched rod (polyvinyl chloride) is attached to the ultrasonic transducer and also holds the sample. The sample is positioned between these two rods as shown in Fig.3.8.

Both rods and the sample are modeled as an infinite acoustic field where the ultrasound wave propagates through. By means of the received echoes on the oscilloscope, first we'll collect the emitted pulse, after a while, the entry-echo will be received and the back-wall echo in the sequence, as shown in red on Fig. 3.8, and mathematically explained in Sec.3.1.2.2.

A common rule of thumb for the pulse-echo procedure, is to have the sample depth at least 5-10 wavelengths of the ultrasound wave being used. This ensures that the primary reflection from the front surface of the sample (here called as entry-echo), is distinguishable from any subsequent reflections from the back-wall (back-wall echo). This means that if the sample depth isn't large enough, the subsequent reflection between the entry and back-wall echo will be close in a non desirable way. Hence, there is also an upper size limit for the sample's depth, the wave propagation time through the buffer rod must be greater than the time in which it propagates through the sample, this avoids multiple reflection within the buffer rod before the back-wall echo arrives (McClements & Fairley 1991; McClements & Fairley 1992). All the echoes are labeled at Fig. 3.8 for better understanding.

Another point of concern is the cross-sectional area of the ultrasonic cell, which corresponds to the area where the normal vector aligns with the direction of the wave propagation. The cell's normal area should generally be several times the diameter of the transducer's active area. It helps to ensure that the main beam of the ultrasound wave interacts first with the sample and not with the side walls of the cell, which can possibly create undesired side echoes. Since the wave field is modeled as infinite, lateral reflections are unwanted, only reflections occurring at the interfaces are considered: between the sample and the buffer rod and between the sample and the back-wall Fig. 3.8. These reflections are modeled based on an infinite boundary between these three distinct media, in which a parallel plane wave goes through them.

To achieve this, a back-wall of the same size as the sample cell and with a smooth flat surface is placed at the bottom to reflect ultrasonic waves. Consequently, the reflection coefficient R remains consistent for both downward and upward propagation during each measurement. For specular reflection, where the angle of incidence equals the angle of reflection, the transverse dimensions of the reflector plate's surface must be significantly larger than the wavelength (Kinsler *et al.* 2000); a small object in front of a wave surface will scatter it all around.

With that in mind, McClements & Fairley 1991; McClements & Fairley 1992 pointed out that using a wave transmitter with a diameter d, the width and height of a squared cell should be at least $3d$ to $5d$, providing a sufficient margin to avoid unwanted reflections and side echoes.

Another option is to have the cell radius greater than the greatest depth dimension (adding sample's depth), which will also ensure that the first reflections observed by the oscilloscope will come from the entry and back-wall echo consecutively. Both requirements were applied in this work, proving to be a correct procedure.

The dimensions and frequencies chosen in this study were carefully selected to align with the fundamental principles of the pulse-echo technique, which focuses on generating a signal commonly referred to as the "A-line". This signal represents a one-dimensional (depth) profile of the received echo signals. To accurately reconstruct the A-line, several key assumptions are made. First, the transmitted pulse is considered extremely short in duration, closely approximating a delta function in the time domain. This ensures precise temporal localization of the reflected signals. Additionally, the propagating wave is assumed to be planar, with attenuation of its amplitude attributed only to the medium's intrinsic attenuation characteristics and the transmission coefficients at interfaces (Azhari 2010).

Furthermore, the structures or interfaces encountered by the propagating wave are modeled as a series of thin, parallel plates, which simplifies the dynamics of wave interaction. Lastly, all targets within the wave's propagation path are assumed to be oriented perpendicular to the propagation direction, ensuring that only axial reflections and transmissions are taken into account, thereby disregarding contributions from off-axis interactions. These assumptions create a streamlined framework for reconstructing the A-line and analyzing the acoustic behavior of the system under investigation.

The use of a buffer rod instead of direct transducer-sample contact, is widely employed in acoustic characterization of solids, fluids and emulsions

As stated before in Sec.3.1.2.1, Buckingham & Richardson 2002 addressed impedance mismatch using a setup with one emitter and two receivers calibrated in water. In contrast, the buffer rod concept from Papadakis 1968 overcomes these challenges with a single transducer serving as both emitter and receiver.

The buffer rod introduces an intermediate reflection, the "entry echo," replacing the first receiver in Buckingham's setup. The back-wall echo then acts as the second, the sample attenuated one. This configuration enables pulse comparison and provides insights into the properties of the sample using only one transducer.

3.2.2 Samples, working frequencies and applied power

Based on the knowledge presented in Sec. 3.2 and the working frequency chosen, the measurement cell has a diameter D of $203.2mm$, the buffer rod has $50mm$ of length *d'*, the back-wall has $50mm$ of length and the sample's depth *l* is $5mm$.

3.2.2.1 Barite and glass spheres morphology

For the chosen frequency, Riebel & Löffler 1989 assumes that the particle size range must be known in advance, allowing the selection of a correspondingly appropriate frequency range. Therefore, a detailed study were carried out to better understand our sample microstructure.

A morphological analysis of the barite sample was performed using a Scanning Electron Microscope (SEM) from JEOL, model JSM-6010LA.

The samples were prepared by diluting $0.1g$ of barite in $10ml$ of deionized water to create a stock solution. Subsequently, $200\mu l$ of the stock solution was further diluted in $1ml$ of deionized water.

In the image below, a 1,000x magnification provides an enhanced visualization of the overall distribution of the barite sample, as shown in Fig.3.9.

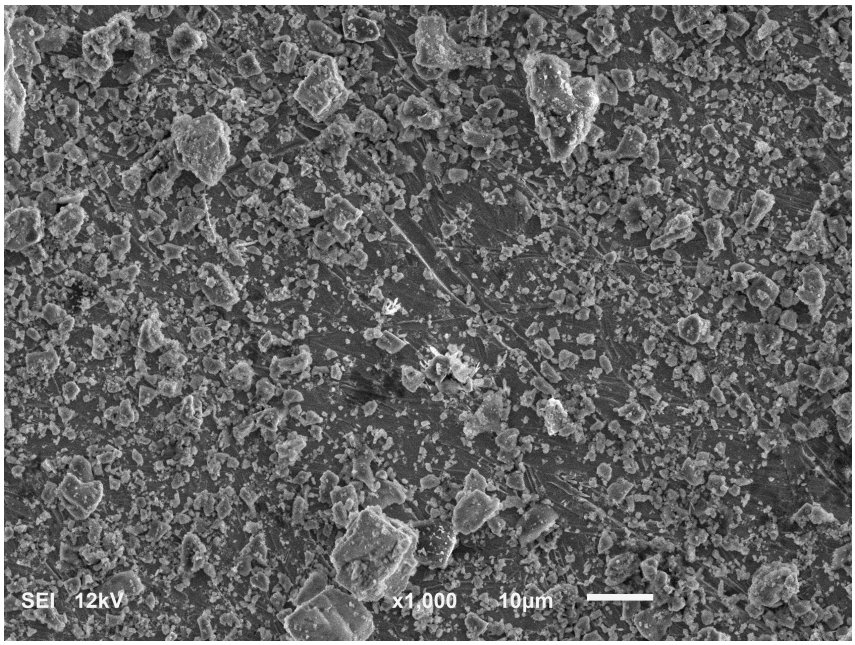

Figure 3.9 – Barite sample at 1,000x magnification.

As observed in Fig.3.9, the sample contains larger particles measuring approximately

$10\mu m$, with smaller particles dispersed within the voids of the larger ones.

Further magnifications of 3,500x and 11,000x were applied to examine the morphology of the smaller particles, as presented in Fig.3.12.

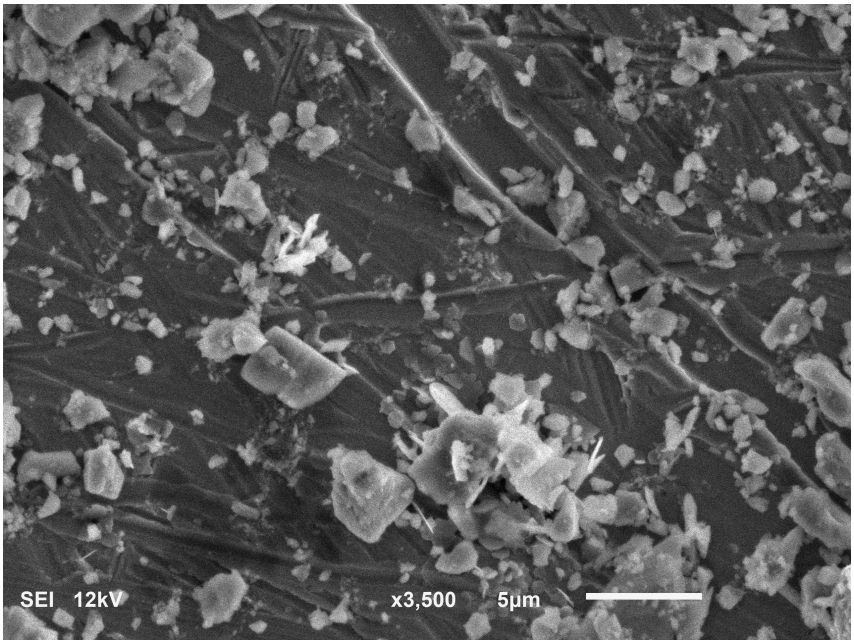

Figure 3.10 – Magnification at 3,500x.

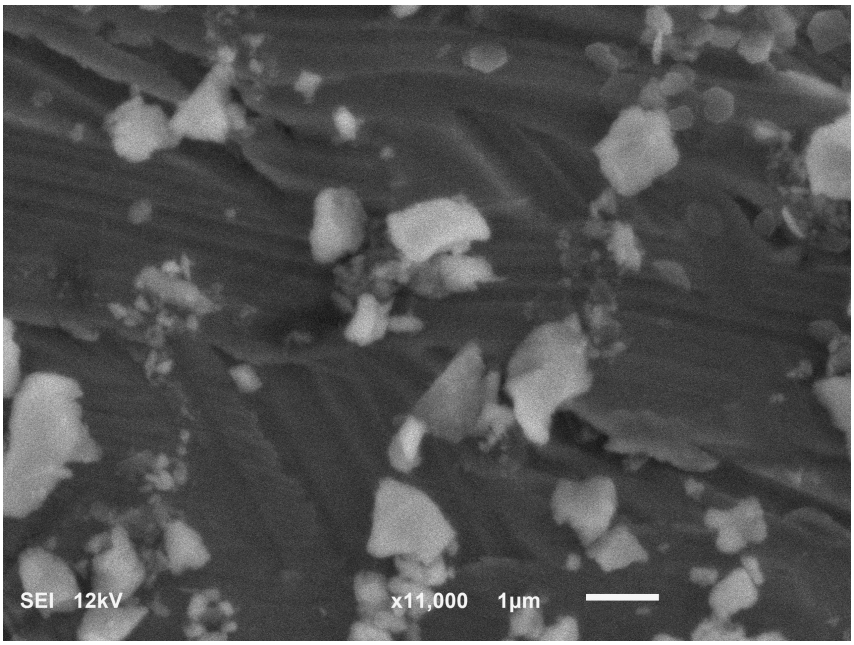

Figure 3.11 – Magnification at 11,000x.

Figure 3.12 – Morphology of the smaller particles.

Examining Fig.3.10, it is evident that the smaller particles range in size from less than $500nm$ to approximately $5\mu m$. However, upon closer inspection of Fig.3.11, it becomes

more apparent that these smaller particles are likely fractured fragments of the larger ones. This hypothesis aligns with the behavior of barite in offshore pipelines, where the particles undergo fragmentation due to impact forces within the flow.

Based on the SEM analysis, barite exhibits a broad size distribution, ranging from $1\mu m$ to $10\mu m$, along with a non-uniform geometry, lacking a consistent morphological pattern.

For this study, glass spheres were also used as samples due to their well-known size and morphology. As further detailed in Sec.4, they aid in understanding the structure of barite and the behavior of sound waves. Several authors have resorted to glass spheres to investigate sound behavior at high frequencies while varying particle size and geometry. Since glass spheres have well-controlled parameters, researchers can isolate and vary only one parameter at a time, allowing for precise observation of its acoustic signatures.

Regarding the glass spheres, their morphology and properties were easily determined due to the controlled fabrication process. The data were provided by the supplier that furnished the samples. Their sizes range from $53\mu m$ to $106\mu m$, with a sphericity of 80%. Although the supplier provided several other parameters, they will not be presented here due to the lack of corresponding physical property data for barite.

3.2.2.2 Compaction control

For compaction control, a vibrating table from ELO Scientific, model SP-1100 was used, onto which the measurement cell was securely fixed, as shown in Fig. 3.13.

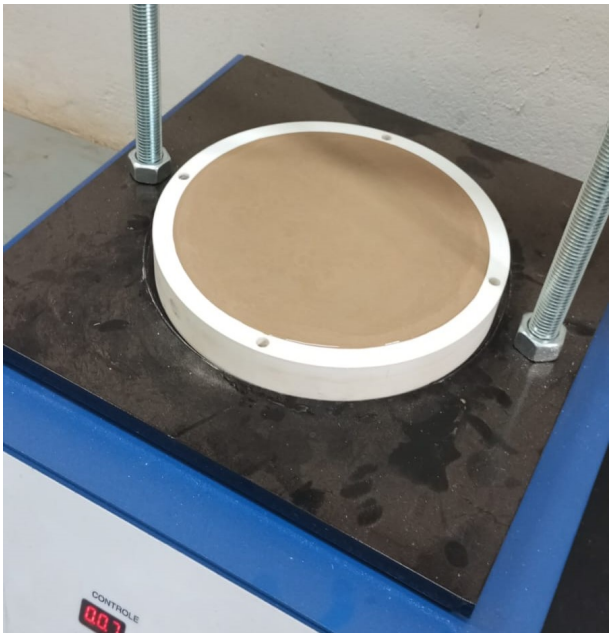

Figure 3.13 – Experimental procedure for compaction control.

The barite mud was poured into the sample holder, and the measurement cell was fixed on the vibrating table. Vibration continued until the mud spread evenly across the surface of the sample holder and air bubbles stopped emerging.

After this initial stage, the first measurement was taken. Subsequent measurements for increasingly compacted samples were performed at controlled intervals of 10 minutes per compaction level. The most compacted samples were those that remained under vibration and the influence of gravity for the longest duration.

3.2.2.3 Frequency range

In addition to grain size and morphology, a physical understanding of the phenomena, grounded in specialized literature Sec.2, provides the basis for selecting an appropriate working frequency to target a specific acoustic signature. As specified in Sec.2, selecting a wavelength that falls within a transition regime $ka \approx \mathcal{O}(1)$ (where one regime is dominated by diffraction effects and the other by scattering effects) allows for an investigation of compaction behavior. In such cases, variations in pore size, grain compaction structure, might shift the system from one acoustical regime to another, enabling the acoustic characterization of these changes.

Using $1MHz$ as the central frequency is particularly effective for testing sediment compaction and the regime transition behavior in the barite study, as it positions the ka relation

around $\mathcal{O}(1)$. For a better understanding of the ka relation with the boundaries of these acoustical regimes and their characteristics, the reader is referred Sec. 2.

3.2.2.4 Electronic equipment

The signal generator utilized is a Model 5077PR from Panametrics-NDT, the available transducer for the task is a V102-RM VIDEOSCAN model from Olympus, with $1MHz$ of nominal frequency allied with a model zz from Tektronix oscilloscope and a post-processing software done in a Matlab environment.

For the power amplitude applied to the system, when operating in a wavelength regime where scattering is unavoidable, increasing the power as the sample depth increases may result in the same back-wall echo amplitude. However, the initial portion of the sample will experience a higher pressure compared to the previous measurement. Nevertheless, this can increase the response of small flaws and grain boundaries, giving a different scattering phenomena. As a result, all the specimens and layouts must be inflicted by the same wave power (Krautkrämer & Krautkrämer 2013), so, all the measurements made for this work were done at a voltage of $300V$.

3.2.3 Measurement challenges and future improvements of the ultrasonic cell

The geometry described in Sec. 3.2.1 posed certain challenges to the measurements, which future studies will aim to overcome.

The first issue concerns polyvinyl chloride (PVC), which exhibits high attenuation. The amplitude difference between the entry echo and the input signal was significantly greater than that observed with acrylic in previous measurements, thereby reducing the signal-to-noise ratio SNR. Additionally, PVC's opacity prevents visual inspection of the sample after fixation, potentially allowing air bubbles or uneven surfaces to go unnoticed. These imperfections can be inferred from anomalous acoustic data, but by the time they are detected, significant effort has already been invested in data collection. A transparent material would enable early detection and correction of such issues.

Another challenge arises from using the same material for both the buffer and back-wall. Since the input signal must return to the transducer, energy losses reduce the signal-to-noise ratio. Ideally, a buffer material with an acoustic impedance similar to the sample's allows more energy transmission, facilitating measurements of highly attenuative materials. However, using

the same approach for the back-wall is problematic, as excessive energy transmission reduces reflection at this interface. To enhance signal recovery from the back-wall, a high-impedance material is preferred. In the ideal case, an infinitely rigid back-wall with infinite impedance would provide a reflection coefficient of 1.

The sample's depth also plays a crucial role in signal conservation. If the signal is too weak, a deeper sample may absorb all the energy. Using optimized materials for the buffer and back-wall allows for increased sample depth due to signal strength. According to the theory in Sec. 3.2.1, the sample depth should be at least five times the wavelength to avoid overlap between the entry-echo and back-wall echo.

Based on these considerations, a suitable material pairing for this task is a buffer made of crystal acrylic and a back-wall made of stainless steel.

Crystal Acrylic is widely used in the literature due to its well-characterized acoustic properties, including low attenuation and minimal wave distortion. Its transparency also enables visual inspection of the sample after fixation, preventing undetected air bubbles or improper contact.

Stainless steel may be chosen for the back wall due to its high density and wave speed, which create a strong acoustic impedance mismatch with the sample. This enhances the desired reflection, increasing the SNR. While perfect reflection (100%) is theoretically ideal, it is not experimentally feasible. Additionally, stainless steel offers resistance to corrosion from liquids and chemical reagents, further improving the setup's durability.

In Appendix B, these improvements are tested in the COMSOL environment to evaluate whether they can effectively address the previously mentioned issues, while also demonstrating how numerical simulations can aid in the construction of the experimental cell.

3.2.4 Planar wave considerations and scattering

As previously discussed, the acoustic theory outlined in Sec. 1.2 assumes a planar, lossy wave propagation, which is not an accurate depiction of the complex propagation dynamics within the ultrasonic measurement cell. Weight 1987 noted that modeling the propagation of short ultrasonic pulses in solid media is considerably more challenging, both theoretically and experimentally, compared to wave propagation in fluids. This complexity arises because many diffraction studies and analyses, including those associated with short-pulse transducers used in nondestructive testing *NDT*, are primarily limited to fluid media.

In contrast, the ultrasonic cell investigated here involves a solid and granular media of finite dimensions, where both longitudinal (compression) and transverse (shear) waves can propagate, and the wave can also be scattered all around. This wave conversions significantly complicates the application of the simplified wave field solutions presented in Sec. 1.2, which were developed with less intricate propagation conditions in mind. Consequently, adapting these theoretical frameworks, or geometry, to accurately capture the wave dynamics in such a system requires additional considerations and modifications.

3.2.4.1 Mode conversion

Mode conversion is the process where acoustic energy transitions between longitudinal and shear waves or vice versa, and it occurs at interfaces where there is a mismatch in acoustic properties, such as density and wave velocity, between two materials. This phenomenon is particularly pronounced when at least one of the materials is rigid, as rigid media support both longitudinal (compression) and shear (transverse) wave modes. At an interface, when an incident wave strikes at an oblique angle, the acoustic impedance mismatch and rigidity of the material facilitate the generation of new wave modes Fig. 3.14. For example, a longitudinal wave may partially convert into a shear wave upon transmission or reflection, and similarly, a shear wave may convert into a longitudinal wave.

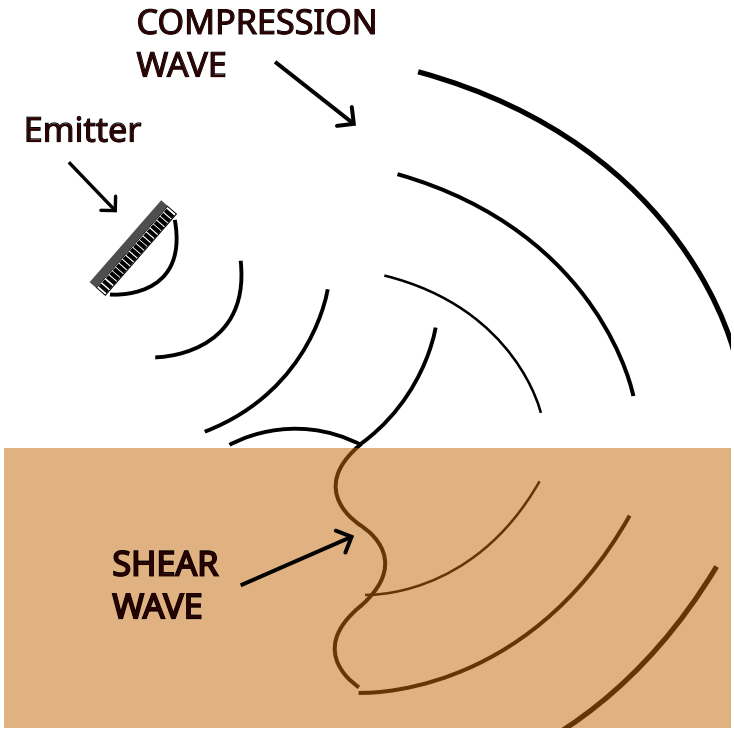

Figure 3.14 – Mechanical wave mode conversion representation.

When an acoustic transducer is coupled to a solid buffer material with finite lateral dimensions, the edges can generate both longitudinal and shear waves, as illustrated in Fig. 3.15. Some of the shear waves undergo mode conversion into longitudinal waves, which are then reflected at the buffer rod/sample interface. These converted longitudinal waves are subsequently detected by the transducer, which is typically optimized for sensitivity to longitudinal waveforms (Bjørndal 2007). This process is further illustrated in Fig. 3.15, offering a clearer representation of the phenomenon.

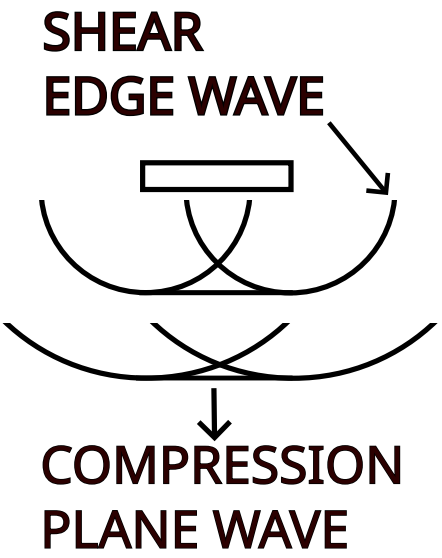

Figure 3.15 – Mechanical wave mode conversion for sources with finite sizes.

In this study, the influence of mode conversion is mitigated by carefully isolating the desired echo signals within time intervals that are free from interference caused by mode-converted waves. This is achieved by utilizing buffer rods with sufficiently large dimensions, which not only minimize the impact of mode conversion but also simplify the process of accounting for diffraction effects. By designing the experimental setup to reduce these complications, the accuracy and reliability of the measurements are significantly improved. As a matter of fact, mode conversion between interfaces is unavoidable; however, the geometry and transducer placement are designed to minimize this effect as much as possible. Another type of errors, such as noise, scattering, windowing, are more prominent than mode conversion and they will be discussed later.

3.2.4.2 Diffraction

Diffraction refers to a specific form of wave interference that arises when a wave is partially obstructed due to the finite dimensions of the source or receiver. This phenomenon introduces distortions in measurements, necessitating corrections that account for both the time-dependent and amplitude-related properties of the pulses to ensure precise results, for highly sensitive samples. This phenomenon introduces distortions in measurements, requiring corrections that address both the time-dependent and amplitude-related properties of the pulses

to ensure accurate results, particularly for highly sensitive samples. These distortions can affect wave amplitude due to energy conservation principles. In a non-dissipative medium, the amplitude of a planar wave remains constant. However, for a non-planar wave, the energy is distributed across the wavefront, causing the wave's surface area to expand over time. As this surface area increases, the energy per unit area decreases, leading to a reduction in amplitude that isn't related to the medium attenuation.

In Fig. 3.16b, a wave exhibiting diffraction characteristics due to the finite size of the emitter is shown, whereas Fig. 3.16a illustrates the propagation of an ideal plane wave with infinite dimensions.

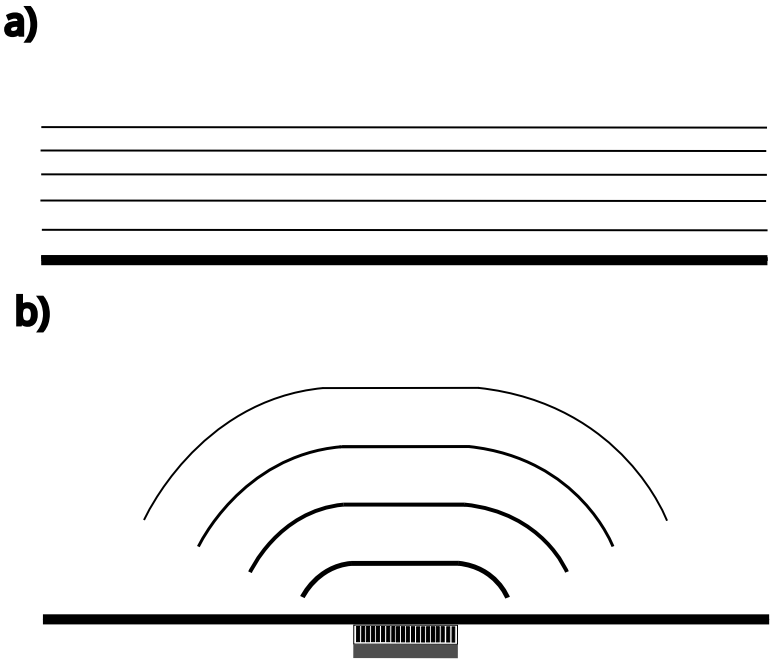

Figure 3.16 – No diffraction presence (a), diffraction representation for sources with finite sizes (b).

A comprehensive explanation of how diffraction corrections are applied within the context of the measurement methodology used in this study is provided in Section 3.3.

3.2.4.3 Scattering

Another source of error when trying to obtain the intrinsic acoustic attenuation, is the scattering, which represents the energy wave that wasn't absorbed by the sample nor transmitted by the back-wall, instead of it, it was scattered all around due to the contact between the wave and structures with dimensions in the order of the wavelength regime. When dealing with media

characterization, this phenomenon can be useful for understanding its microstructure, as in our case.

Losses in the "scattering loss range" arise either from interference between the scattered wave and the incident wave, or from the scattering of sound energy from the beam path, preventing it from reaching the point of detection (Lowan 1946).

Under conditions of short wavelengths, scattering becomes more dominant compared to geometric spreading effects, such as diffraction. This phenomenon is analogous to the way light from a headlamp is scattered by tiny water droplets in fog. For grain sizes *a* that are approximately $1/1000th$ to $1/100th$ of the wavelength λ, corresponding to $ka < \mathcal{O}(0.01)$, scattering is practically negligible. However, scattering increases rapidly, roughly proportional to the third power of the grain size, becoming significant for grain sizes on the order of $1/10th$ of the wavelength, or $ka \approx \mathcal{O}(0.1)$. At this scale and beyond, reaching up to $ka \approx \mathcal{O}(1)$, scattering becomes a dominant factor. For highly anisotropic materials, where $ka >> \mathcal{O}(1)$, scattering can be so pronounced that ultrasonic testing becomes impractical (Krautkrämer & Krautkrämer 2013).

Scattering echoes significantly diminish the amplitude of the primary echo signals, both at the entry point and at the back-wall of the sample. Additionally, they generate numerous secondary echoes with varying transit times, often referred to as "grass." This phenomenon can obscure the desired echoes, making their identification and analysis more challenging.

Scattering can be likened to the effect of fog, where a driver becomes blinded by the glare of its own headlights, rendering the surroundings difficult to see. This disturbance cannot simply be mitigated by increasing the transmitter voltage or amplification, as the "grass" i.e. numerous secondary echoes, intensifies proportionally. The only effective solution is to employ lower frequencies, which inherently reduce the sound's beaming effect and increase pulse length, reducing the resolution. Hence, this approach imposes a natural limitation on the *ka* parameter, which must be carefully accounted for in any analysis (Krautkrämer & Krautkrämer 2013).

In Fig. 3.17a, a depiction of high-frequency wave propagation highlights the prominence of the scattering phenomenon. Conversely, Fig. 3.17b illustrates the scenario for long wavelengths, where scattering effects are significantly diminished to negligible levels. This reduction in scattering, however, comes at the cost of decreased resolution, making it challenging to observe acoustically fine structural details.

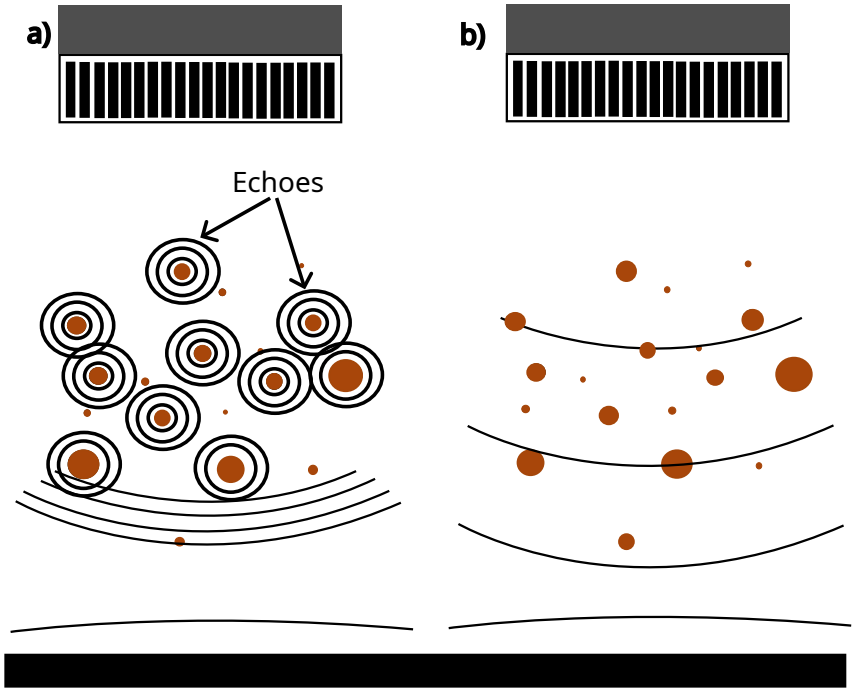

Figure 3.17 – Scattering representation for shortwavelength (a) and longwavelength (b).

The intrinsic wave attenuation is the sum of thermal dissipation losses, visco-inertial dissipation losses, and intrinsic absorption (McClements *et al.* 2000). Therefore, if the goal is to analyze intrinsic wave attenuation, scattering must be carefully considered. In this study, where the focus is on analyzing the sample at high frequencies in regions where the presence of scattering is uncertain (depending on compaction and size distribution) investigating this phenomenon could provide valuable insights into the effects of compaction and granular size on wave attenuation. Based on that, several authors developed numerous scattering models for such analyzes, as the one used by Hare & Hay 2018.

Anderson 1950 results indicate that the transition region between the scattering- and diffraction-loss ranges extends from $2.5 < ka < 3.0$ for each frequency, as pointed out before, near the range utilized in this work. This region is responsible for diffraction and scattering being the main source of intrinsic attenuation errors, with $2\pi r/\lambda$ below 2.5, diffraction is dominant, and with $2\pi r/\lambda$ above 3, scattering is dominant. However, data from Hare's work indicates a limit around $ka \approx 0.5$.

3.3 Diffraction Correction

The main sources of error in the measurements stem from several factors, including temperature fluctuations, misalignment or lack of parallelism between the face of the buffer

rod and the back-wall, inaccuracies in the diffraction corrections applied, and inconsistencies in the output signal of the emitter (McClements & Fairley 1991; McClements & Fairley 1992). Furthermore, as highlighted by Buckingham & Richardson 2002; Bjørndal 2007, the application of windowing techniques to transient data introduces additional sources of error into the measurement data processing.

Since most of the errors outlined above were minimized during the construction of the ultrasonic measurement cell Sec.3.2, the last one to be analyzed before proceeding with data processing is diffraction Sec.3.2.4.2.

During ultrasonic measurements conducted in the laboratory, one of the main source of errors arises from the diffraction phenomenon, which occurs due to the finite dimensions of the transducers relative to the wavelength (Tang *et al.* 1988).

When measuring the attenuation coefficient of ultrasound using the standard pulse technique in low absorption media, particularly in the mega Hertz frequency range, it is possible to introduce specific corrections to the obtained results (Khimunin 1972). Diffraction plays a significant role in such measurements, as it can noticeably contribute to the apparent attenuation while causing a slight increase in the measured velocity (Papadakis 1966). Given that the present medium exhibits high attenuation, the applicability and effectiveness of this correction approach will also be evaluated in the current study.

Kažys *et al.* 2002 stated that to mitigate these errors, an additional buffer rod can be employed as a waveguide between the transducer and the measurement chamber. This setup were applyied here and ensures that the measurements are conducted within the transducer's far-field zone, thereby reducing the influence of diffraction effects.

Additionally, diffraction effects in ultrasonic attenuation measurements can be effectively minimized by several adjustments to the experimental setup. These include increasing the length of the sample (i.e., the distance between the pulses), raising the operating frequency of the transducer, enlarging the transducer radius, and reducing the velocity difference between the test sample and the reference sample (Feng *et al.* 2018). Obs.: diffraction when using Papadakis' method isn't improved by the latter.

Based on the work of Khimunin 1972, a diffraction correction parameter D will be presented, aiming for improvement for Papadakis' method diffraction error. Following Williams 1951, this parameter is defined as the ratio between the measured average pressure on the front wave and a plane wave pressure at the same distance. The average pressure is

considered on a uniformly sensitive receiver, assuming circular transducers of equal radius *a* in an infinite, uniform, isotropic medium without absorption:

$$D(ka,S)=\frac{\bar{P}}{P_o}=1-\frac{4}{\pi}\int_0^{\pi/2} exp\left[-i\frac{(ka)^2S}{2\pi}\sqrt{1+\left(\frac{4\pi}{Ska}\right)^2 cos^2(\theta)}\right] sin2(\theta)d\theta. \quad (3.27)$$

Here, *S* is the dimensionless distance, defined as $S=\frac{z\lambda}{a^2}$, which represents the wave path throughout the medium normalized by the Fresnel zone. This concept will be discussed in more detail later in this dissertation.

For this equation, there is no analytical solution for the general case, i.e. arbitrary *ka*, so numerical methods must be used. Khimunin 1972 implemented these methods on a computer *BESM 4* employing Simpsons's method with a reasonable error. Rogers & Van Buren 1974 otherwise, shown that the required integral of Lommel's expression can be evaluated analytically obtaining a simple closed-form expression for the diffraction correction using Bessel's function of cylindrical coordinates:

$$D(S)=1-e^{-(\frac{2\pi}{S})i}\left[J_0\left(\frac{2\pi}{S}\right)+J_1\left(\frac{2\pi}{S}\right)\right]. \quad (3.28)$$

Taking the absolute value of Eq. 3.28 provides the diffraction correction for the amplitude Eq.3.18, while applying the inverse tangent *arctan* function gives the correction for the phase.

Using the proposed measuring cell, the emitted wave propagates through different media, such as the acoustic coupling layer, buffer rod, and sample path. As a result, the propagation media are not isotropic and homogeneous, as assumed by the presented model. To address this, Bjørndal 2007 suggested that when using buffers much greater than the sample, the accumulated error becomes negligible, given that less than 5% of the propagation occurs through granular media. This assumption is based on the work of Papadakis 1968, who developed a method to correct this anisotropic issue. Given that the difference between the distance traveled by the first echo (entry-echo) through the buffer rod and the wave that propagated through the buffer rod plus the sample (back-wall echo) is minimal, Papadakis 1968 assumed that the product *kz*, which represents the phase of the wave as it propagates through the medium, is the same for both the buffer rod and the sample. This assumption holds due to the minimal contribution of the sample to diffraction errors.

So basically, the axial distance normalized to the last axial pressure maximum in the piston model (Williams 1951) can be presented for each echo as:

$$S_{A,1} = \frac{2l_1c_1}{a^2f}, \tag{3.29}$$

$$S_{A,2} = S_{A,1} + \frac{2l_2c_2}{a^2f}. \tag{3.30}$$

All these S-values are inserted into Eq. 3.28 to calculate the diffraction correction for each desired echo.

As said, to analyze the time shift of the wave velocity in the time domain, we must take the argument of Eq. 3.28:

$$t_{dif} = -\frac{tan^{-1}(D(S))}{w}. \tag{3.31}$$

To obtain the corrected wave velocity, Eq. 3.31 must be subtracted from the denominator of Eq. 3.22, and for attenuation, Eq. 3.28 must be accounted in Eq. 3.18.

3.4 Data acquisition and processing

Efficient data acquisition and processing are essential for extracting meaningful insights from the received signals. This section outlines the fundamental steps involved, including signal reception, digitization, and processing techniques to enhance signal quality and extract relevant features.

The main steps of the signal processing are shown in Fig. 3.18.

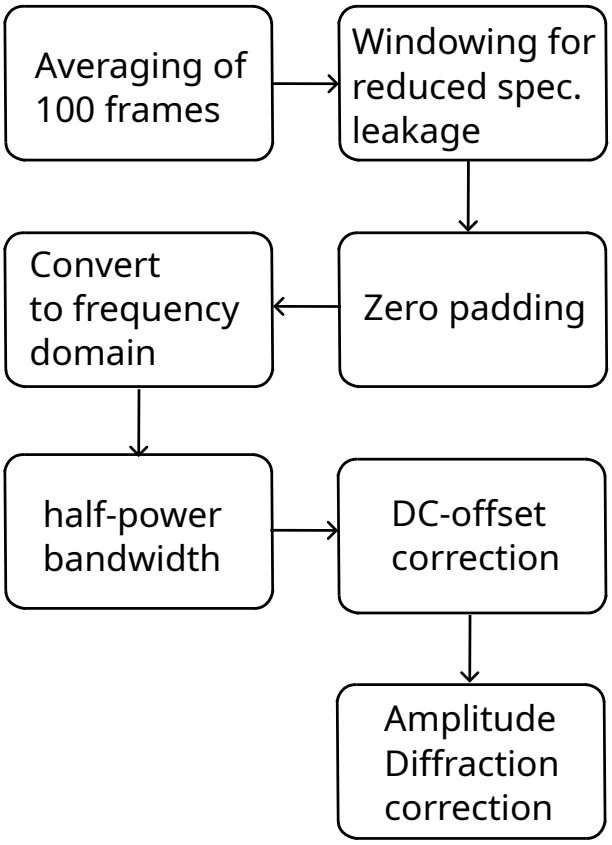

Figure 3.18 – Flowchart illustrating the sequence of data processing steps for the dataset.

1. **Averaging Phase:**

During the averaging phase, repetitive measurements are acquired a specified number of times and are subsequently presented to the PC in an averaged form by the oscilloscope. This approach offers two key benefits:

- The averaged samples achieve an effective resolution for 12 bits,
- Random noise is significantly reduced in the final signal.

The importance of the noise reduction is based on the applied method for this work, the spectral ratio method. Tonn 1989 made comparisons between several types of attenuation measurements methods.

According to Tonn, the spectral ratio method proved to be highly effective when noise interference was minimal. Its efficiency, combined with the ability to integrate statistical analyses, made it particularly suitable for accurate Q estimation. On the other hand, while Modeling Techniques were less reliable in noise-free conditions compared to both the Spectral

Ratio Method and the analytical signal approach, they demonstrated certain benefits when dealing with slight noise disturbances.

In the acquisition process using the oscilloscope, two key aspects are crucial for the signal-to-noise ratio *SNR* and the quality of the acquired signals: temporal resolution and bit resolution. Temporal resolution is essential for accurately obtaining both sound speed and signal amplitudes, while bit resolution primarily affects the accuracy of the signal amplitudes. For this work, a sampling rate of $2.5GS/s$ was used, which is well above the highest frequency content of the echo signals $\mathcal{O}(1MHz)$, thus preventing frequency overlap (aliasing).

2. **Windowing to Reduce Spectral Leakage:**

A Hanning window function is employed to coherently reduce spectral leakage for each echo signal. The window is consistently positioned at the same relative location across all echo signals. The window function's width is constrained:

- At one end, by the start of the acquired waveform,
- At the other end, by the requirement for symmetric placement around the relevant voltage extreme.

Using a window narrower than one period of the burst causes the spectral characteristics to shift from band-pass to low-pass digital filter.

Additionally, to estimate the windowing error, the spectral amplitude algorithm was repeatedly applied to the data, incrementally shifting the start time of the window by $1\mu s$ through a complete wave period. As described in Buckingham & Richardson 2002, the window placement was shifted, and the attenuation variation across measurements was incorporated into the error analysis.

3. **Zero padding:**

In this stage of processing, another crucial aspect is the number of data points collected. As mentioned earlier, the oscilloscope used has a sampling rate of $2.5GS/s$, meaning it captures 2.5×10^9 samples per second. However, for pulse analysis, only a $2.5\mu s$ time window is selected for further processing (pulse duration), as illustrated in Fig. 3.1. This limited window contains approximately 8000 data points. After applying the Fourier transform and isolating the frequency band of interest, only a small subset of points remains.

To enhance the curve, zero padding is applied to the vector, increasing the number of points in the time domain before performing the FFT. This process helps smooth the attenuation

and wave velocity data. To see the representation of the osciloscope vector in which the zeros are added, the reader is referenced to Appendix A Fig.A.2.

Another option made is the least squares sense cubic spline approximation, which can also be used to improve both the temporal- and the vertical resolution (Bjørndal 2007).

4. **Convert to frequency domain:**

This step is related with the spectral analyze of the data collected, a deep discussion were made in Sec.3.1.1.

5. **Half power bandwidth:**

The test conditions in this work, including the ultrasonic instrumentation and the materials of the specimens, differ from those used by the transducer manufacturer, who tested a silica specimen. As a result, the optimal frequency range of the ultrasonic transducer in this study is expected to deviate from the manufacturer's datasheet specifications. To determine this range, the half-power bandwidth ($-3dB$) of the acquired data was analyzed.

For this task, the Eq.3.32 was utilized:

$$M[dB] = 20log_{10}\left[\frac{A(f)}{A(f)_{max}}\right]. \tag{3.32}$$

As a remainder, A is the power spectrum presented before Eq.3.1.

According to Silva 2020, higher attenuation in the sample leads to a narrower half-power bandwidth, which also shifts further from the transducer's resonance frequency specified by the manufacturer. In the case of barite under a $1MHz$ ultrasonic transducer, the higher-frequency components were significantly attenuated, limiting the frequency range with reliable data to approximately 200–$600kHz$.

Based on this investigation, the results presented in Sec. 4 will focus on this identified frequency range.

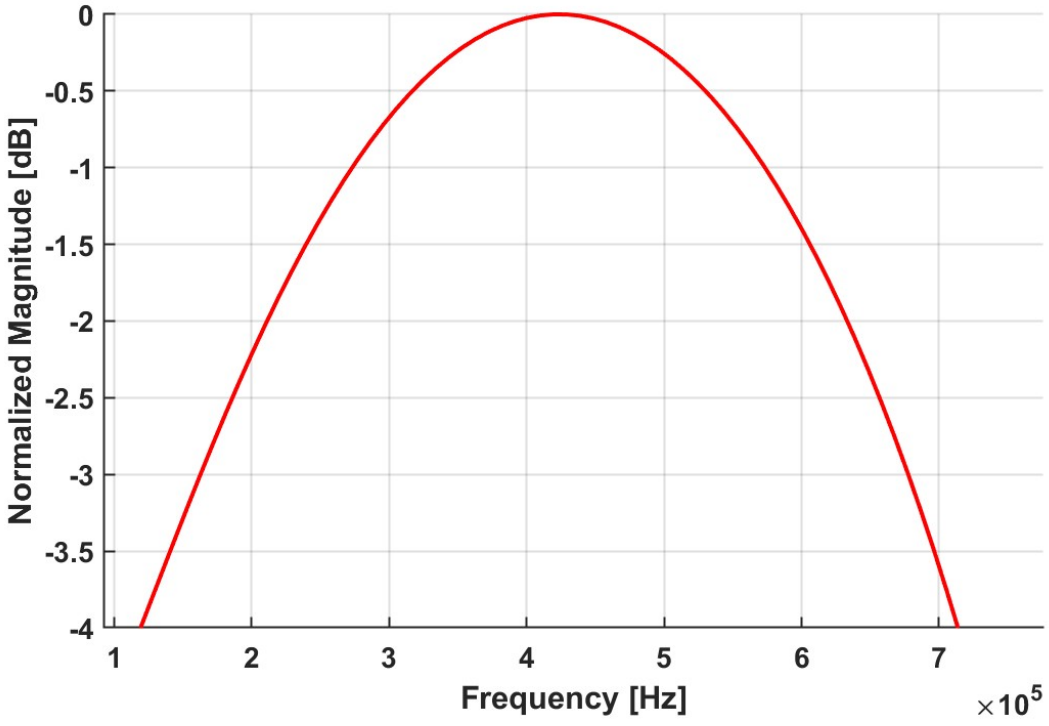

Figure 3.19 – Transducer half power bandwidth.

Fig.3.19 illustrates the downshift of the wave pulse as it propagates through barite. With a transducer nominal frequency of $1MHz$, the energy peak of the frequency spectrum is at $0.4MHz$. However, this too high downshift in the frequency axis is not observed in a less lossy media, such as the polyvinyl chloride or Acrylic, backing the statement made by Silva 2020. This behavior is well-known in the study of wave attenuation, where higher frequencies experience greater attenuation than lower frequencies, leading to a reduction in energy at higher frequencies in the spectral analysis.

6. **DC-Offset Correction:** DC-offset correction is applied to the time frame by determining the average voltage value in a short time window immediately before the first echo signal appears. This offset value is subtracted from every sample in the trace after the first echo signal appears. Without this correction, a low-frequency component would appear in the frequency spectrum in a non-coherent manner across individual echo signals, leading to errors. Additionally, in the frequency domain, the DC component (point 1) is removed from the data before further processing.

7. **Diffraction Correction:**

Diffraction correction is applied to the sound speeds and wave amplitude. More details in Section 3.3.

4 RESULTS AND DISCUSSIONS

4.1 Attenuation

Fig. 4.1 shows the wave attenuation coefficients for barite samples with different compaction levels. The compaction levels are indicated by the C mark in the legend, as follows: $C1 < C2 < C3$ and also by the colors $blue < green < red$. As the number increases, the compaction level becomes higher. Two barite samples were tested, $Sample1$ and $Sample2$, respectively; however, compaction was not controlled between the two samples. The only controlled compaction was within the same sample, as controlled by the C mark.

Each line observed in Fig.4.1 is the average of several collected data. This procedure was done since the attenuation variation in each measurement in the experiment was in the same order of the attenuation variation due to compaction. To address this issue, more than ten data were collected for each level of compaction, and the average value of the data were chosen. For better understanding, doing one measurement, the attenuation in function of sample compaction wasn't being observed, only after several measurements a trend on the data become clear, and it was related with the compaction phenomena.

At first glance on Fig.4.1, one can observe a difference between the curves of the same sample ($Sample1$ or $Sample2$). As the compaction level increases, there is a downward shift in the sample's attenuation magnitude, indicating lower attenuation on average with higher compaction. Another interesting observation is the difference in attenuation between the two samples. Although compaction was not controlled between them, it is reasonable to assume that $Sample1$ is more compacted than $Sample2$. This assumption is supported by the fact that the mud for $Sample1$ was denser and more difficult to handle.

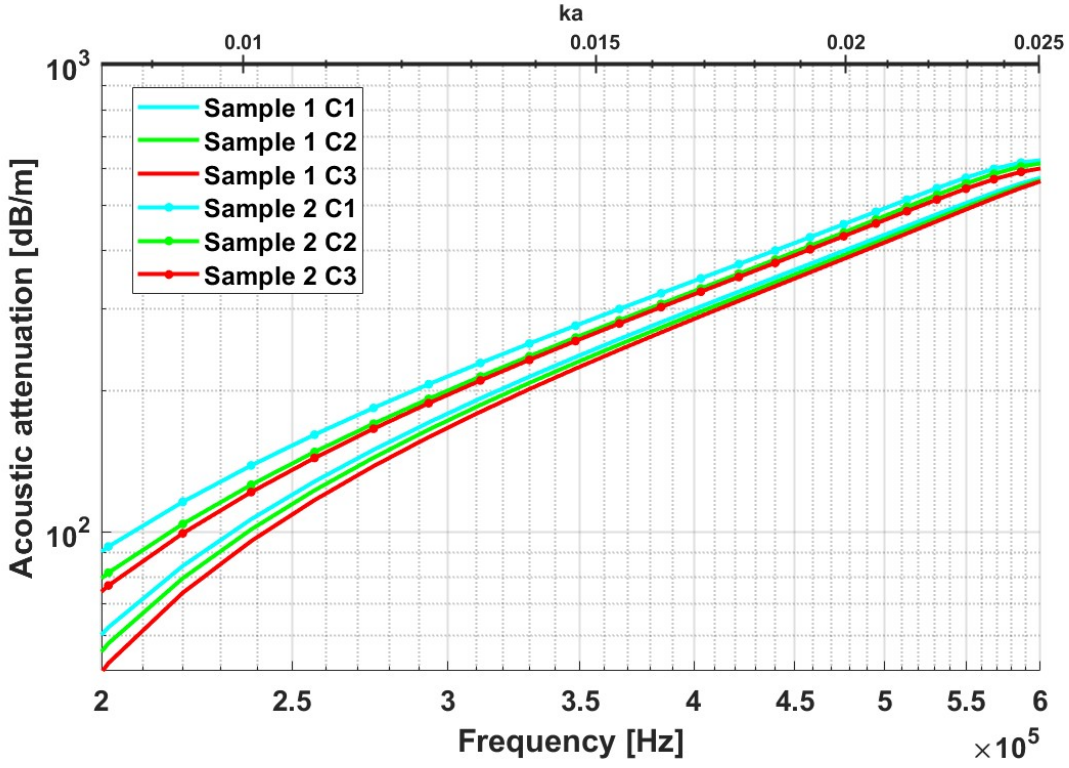

Figure 4.1 – Attenuation comparison with levels of compaction.

The linearity in attenuation observed between 0.2 and 0.6 MHz, as shown in Fig.4.1, is consistent with the findings of Hamilton 1980, who documented similar behavior up to 1 MHz in "clay-like" marine sediments, which resemble the barite sample, which are also backed by Argo 2012; Lee *et al.* 2009; Kimura 2011; Kimura 2014; Dunlop 1988. Clay-like sediments typically range from units to dozens of microns (μm), while sandy-like sediments range from hundred to thousand of microns (μm). Jackson & Richardson 2007, in contrast to Hamilton's data, presented a data regression for 78 siliciclastic and carbonate sites where in situ measurements were were conducted at either $38kHz$ or $58kHz$, frequencies much lower than working frequency utilized, but they can still serve as preliminary validation for this work, which will be further refined in subsequent studies. This regression also have shown a linear behavior, as seen in Fig. 4.1.

Dunlop 1988 introduced a variable called the "structure factor" g to analyze wave attenuation as a function of variations in pore directions. The structure factor, as described by Dunlop, accounts for the apparent increase in fluid inertia due to the random orientation of pores in a sediment. It modifies the effective fluid density in Biot's theory, meaning a difficulty for the fluid to go through the pores in the wave propagation direction. Dunlop observed that increasing

the g factor, by increasing compaction and reducing the pore sizes, resulted in a reduction in acoustic wave attenuation. This behavior can be explained using Biot's acoustic theory.

There are two ways of compressional wave propagation through granular media according to Biot's model. For long wavelengths, where the wavelength is much larger than the granular structures, the medium behaves like a homogeneous material. In this case, propagation is governed by the skeletal frame properties, which arise from the interactions between the particles (Stoll 1989). However, for higher frequencies (shorter wavelengths), where the wavelength is no longer much larger than the granular structures, the phenomenon of decoupling begins to occur. Instead of the medium acting as homogeneous, the fluid within the medium starts to move relative to the skeletal frame, introducing additional attenuation mechanisms, such as viscous damping. The reader is referred to read Sec.2 for a better understanding.

The last statement highlights how a granular structure susceptible to a relative flow displacement (high porosity) can impose higher attenuation for a viscous dominated sound wave, due to increase in the viscous damping presence while obscuring the solid frame damping.

This phenomena were observed by several authors such as Lee *et al.* 2009; Kimura 2011; Argo 2012 while analyzing porosity as the parameter under investigation. However, as exemplified in Sec.2, while increasing frequency, grain size or compaction level, the order relation between attenuation and frequency increases, going from $f^{0.5}$ to f^4. Such trend wasn't observed in Fig.4.1, the only trend observed was the attenuation magnitude being reduced.

As stated by Argo 2012, The expected higher-order frequency dependence of attenuation due to porosity reduction was only weakly observed at lower frequencies $\mathcal{O}(400kHz)$ or in samples with smaller grains (small ka). The same statement were made by Kimura 2011 while increasing the granular grain size (porosity reduction), which observed only a downward shift in the attenuation's magnitude for low frequencies $\mathcal{O}(400kHz)$, not seeing any trend of attenuation increase slope in this low frequency regime. Kimura's data showed this tendency of frequency order increase only in lower porosity samples (larger grains) in the high frequency regime.

To avoid misunderstanding by the part of the reader, it's important to keep clear that the lower frequency regime from the works of Lee *et al.* 2009; Kimura 2011; Argo 2012 can be assumed as the high frequency regime (second regime, viscous loss dominated) in the work made by Dunlop 1988. Since Dunlop's compilation worked with way lower frequencies $0.01 - 100kHz$, his high frequency regime can be placed in the low frequency regime in the

works done by the formers mentioned authors, which have worked in the range of $0.3 - 1MHz$.

Since the present work has a mud like sample (small grains and high porosity) Sec.3.2.2, even though working in a high frequency range susceptible to the frequency order increase due to compaction, the data collected placed the barite sample in a lower ka regime, where a increase in frequency dependence order of attenuation wasn't observed. This can also be observed in the work from Lee *et al.* 2009, in which the samples with mean grain size from $60\mu m$ to $150\mu m$ don't presented a order increase from one another while increasing grain size, only a reduction in attenuation magnitude, backing the data collected from barite, which has small grain size than the ones tested by Lee.

Based on Biot-Stoll theory (Dunlop 1988), it can be seen that for this ka regime (viscous damping dominated), as the permeability (or pore size) decreases (more compaction) while maintaining the same frequency, the acoustic attenuation starts to decrease, as observed in the experiments. This occurs because the pores structure become smaller relative to the wavelength, which remains constant, thus reducing the ratio between pore size and wavelength. As a result, viscous damping (which is more pronounced when the pore size to wavelength ratio is large) is reduced, placing the ka regime of the wave/barite in a region where the skeletal damping starts to become more influent, reducing the attenuation observed.

Nevertheless, in spite of the ultrasonic measurement cell had been under vibration for each level of compaction, and it's had degassed our sample, one can't say that no other air bubble remained within the tested sample; therefore, such attenuation reduction as observed in the measurements could be due to the reduced presence of air bubbles for each measurement compaction level. On the other hand, the observed attenuation behavior can be seen in the specialized literature, which supports the assumption of increased compaction as stated earlier.

Nevertheless, despite the ultrasonic measurement cell being under vibration at each level of compaction (and having degassed our sample) one cannot assert that no air bubbles remained within the tested sample. Therefore, the observed attenuation reduction in the measurements could be attributed to the decreased presence of air bubbles at each compaction level. On the other hand, the observed attenuation behavior is also reported in the specialized literature, supporting the assumption of increased compaction, as stated earlier.

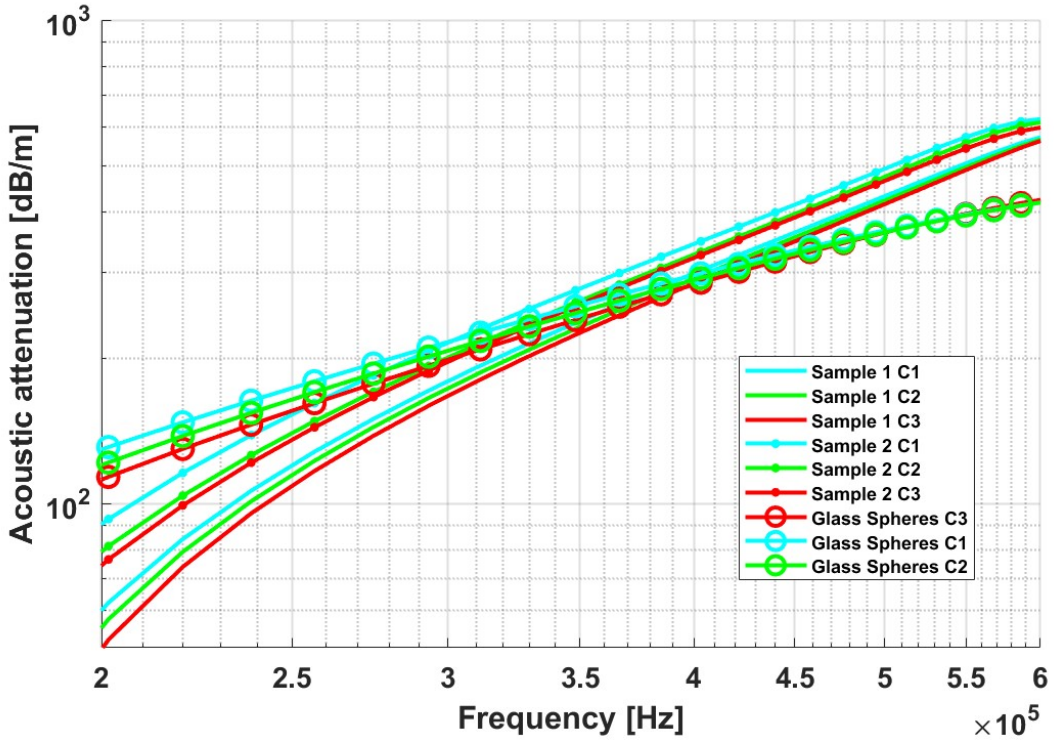

Figure 4.2 – Attenuation comparison between Barite samples and Glass Sphere samples.

In Fig.4.2, when comparing the attenuation of Glass Spheres $60 - 100\mu m$ with the barite samples, a significant difference is observed. Barite exhibits higher attenuation at higher frequencies, but as the frequency decreases, the barite attenuation becomes less than the one from Glass Spheres.

The slope of the attenuation curves for the Glass Spheres varies between samples, but on average, the Glass Spheres shows a shallower slope in comparison with barite. This suggests that their attenuation do not increase as rapidly with frequency as the barite samples.

Similar to Barite, as the compaction of the Glass Spheres increases, the attenuation decreases, even though this effect is more pronounced at lower frequencies. Since the glass sphere sample has a bigger grain size, it places the ka relation closest to the high frequency regime based on the works from Kimura 2011; Argo 2012; Lee *et al.* 2009. As observed by Argo 2012, when increasing the frequency, or increasing the grain size, the relation between higher-order frequency dependence of attenuation and porosity is more evident. This statement by Argo can be the explanation for why the slope wasn't observed clearly in the Barite samples, as it was in the Glass Spheres. This phenomena was also observed by Lee *et al.* 2009.

A similar characteristic was reported by Stoll 1989, based on the work of

The higher frequency exponent observed in the high frequency regime, compared to the low-frequency value, can be explained by greater shear losses due to a higher density of grain contacts per unit volume or by increased scattering losses resulting from a greater number of scattering centers per unit volume

It is important to understand that the long and short wavelength regimes depend on several factors, including frequency, particle size, temperature, structural factor and permeability, to name the most relevant ones. Between these regimes lies the transition zone. Given the grain size of our samples and the wavelength used, the samples are situated in the transition regime, with Glass Spheres being more susceptible to short-wavelength behavior than barite.

Setting aside the fact that Barite and Glass Spheres should not be directly compared due to their significant differences (such as geometry, physical properties, and purity) we will attempt to explain certain inconsistencies in their behavior through physical principles.

Since individual Barite particles ranges from fraction of units to dozens of microns, its frequency order dependence of attenuation is expected to be lower due to the smaller dimensions relative to the wavelength ($ka_{barite} < ka_{glass}$). However, this is not the case, suggesting that other factors are contributing to the higher attenuation observed. As shown in Sec.3.2.2, Fig. 3.9, the microscope image of diluted barite reveals its geometry and adhesion effects, which likely play a significant role in the observed attenuation behavior.

In Fig.3.9, it can be observed that barite particles cluster together, forming flakes of various sizes and shapes, ranging from a few microns to several dozen microns. The morphology of these flakes seems to be irregular, lacking spherical shapes or a consistent pattern. According to the work of

As pointed out above, despite the barite particles being smaller in nominal size than the glass spheres, meaning lower ka relation, the barite sample exhibits higher attenuation slope with frequency. This discrepancy can be explored in future studies, focusing on samples with different geometries (more or less spherical) while maintaining the same physical properties, and vice versa, with the same geometries and varying physical properties. This could clarify another parameters related with wave attenuation for high frequency studies other than ka. The observed behavior could also be attributed to several factors, such as the non-Newtonian characteristics of the compacted barite, possible electrical interactions between barite particles, contamination from unidentified particles, or various other physical properties.

The authors of this study also noted that attenuation results for the glass spheres

were more sensitive to variations in geometry and compaction. This sensitivity can be attributed to the displacement of the spheres, even with slight movements, as they did not easily aggregate. Due to their larger size, the glass spheres are more susceptible to scattering effects, so, small variations in the grain arrangement changed the scattering values. This highlights the sensitivity of non-cohesive granular media to scattering variation in a wavelength range where such effects are prominent. In contrast, the barite sample exhibited more aggregated behavior and smaller nominal sizes, resulting in a more homogeneous wave path compared to the glass spheres.

4.2 Phase velocity

The phase velocity was obtained using the same samples presented in Sec. 4.1. The legend $C1 < C2 < C3$ indicates increasing levels of compaction. As for attenuation, the data presented here is derived from several measurements, representing the average value of these measurements.

It was presented in Sec.3, two types of wave velocity, the group and the phase ones. In despite of that, for this work only phase velocity will be presented, this is made to align with bibliographic comparisons, as it is commonly used to characterize sedimentary media.

Fig. 4.3 shows the phase velocity behavior of barite in function of compaction. At first glance, the positive correlation between compaction and wave velocity is evident, consistent with the literature discussed in previous sections. Additionally, a slight increase in wave velocity with frequency is observed, which is a characteristic of low frequencies or small grains $ka << 1$ in the experimental data, such regime is predicted by Biot-based models.

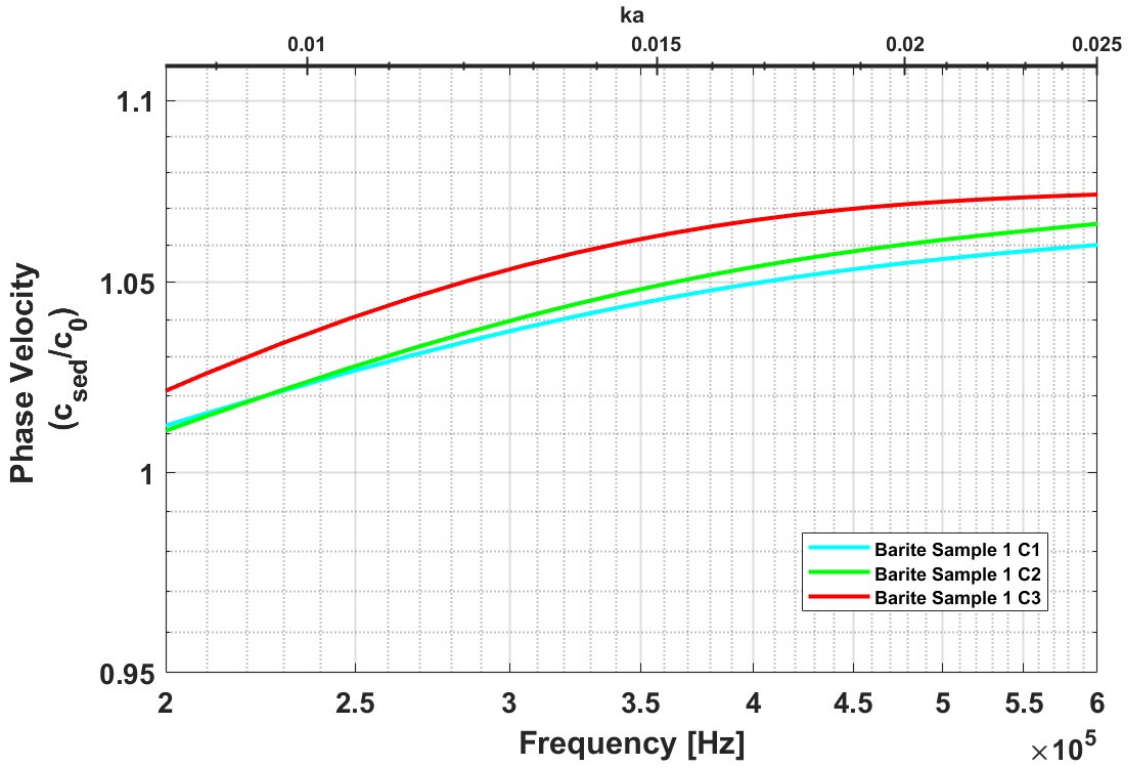

Figure 4.3 – Phase velocity of barite as a function of compaction.

The increase in velocity ratio with decreasing porosity (higher compaction) aligns well with Biot's model, making it reasonable to interpret the results based on its parameters and physical implications. The velocity increase can be attributed to the fact that sound speed in a porous medium is significantly influenced by the skeletal frame modulus and fluid content. As porosity decreases, the proportion of solid grains increases, strengthening the bulk and shear moduli of the medium and thereby increasing acoustic wave velocity. Since the frequency remains in a regime where wave propagation through skeletal frame is present, compaction enhances the rigidity of the frame through which the wave propagates.

Furthermore, higher porosity (lower compaction) results in a greater presence of fluid-filled voids, which reduce the overall stiffness of the sediment, increase attenuation (as discussed in Sec. 4.1), and lower the velocity ratio.

Interestingly, this trend was not observed in the glass sphere samples, as shown in Fig. 4.4.

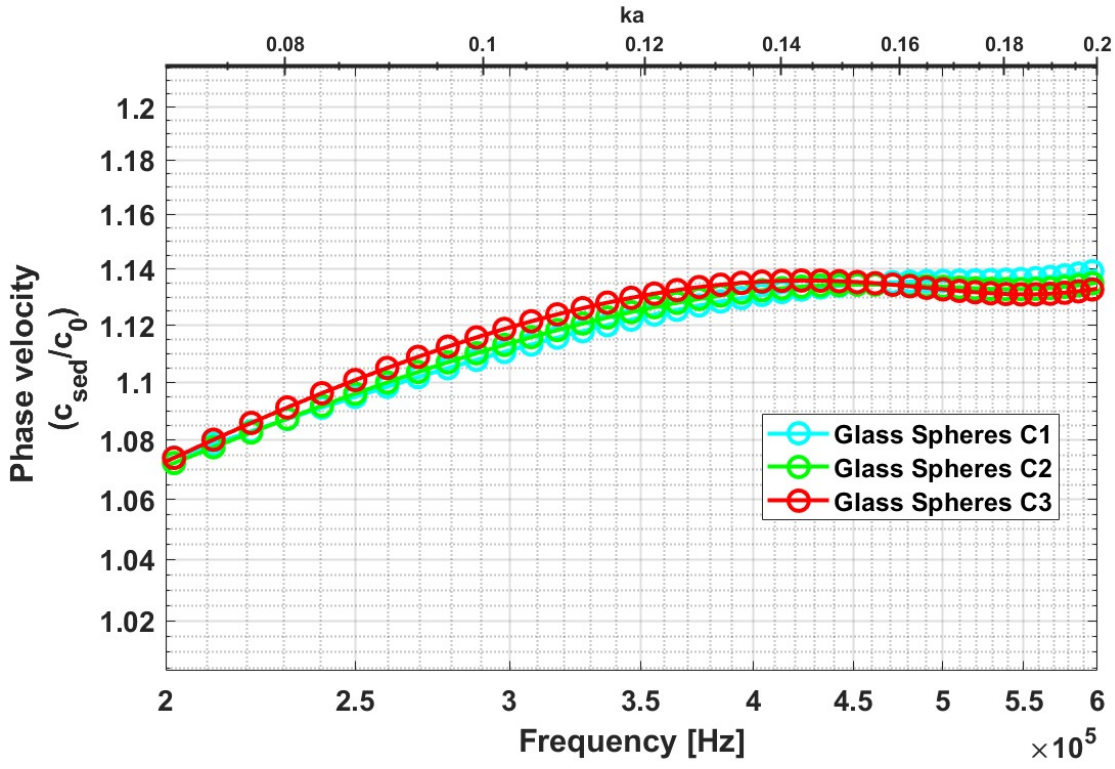

Figure 4.4 – Phase velocity of glass spheres as a function of compaction.

While glass spheres exhibit an increase in wave velocity with frequency, there is no clear correlation between velocity and compaction. Two possible explanations exist for this discrepancy. First, glass spheres may have a greater compaction capacity than barite, resulting in a weaker velocity signature that falls within the data's measurement uncertainty. Second, the ka parameter for the glass spheres could be closer to a transition region where minimal or even negative dispersion is expected (velocity decreasing with frequency). This might explain the observed tendency toward velocity reduction at frequencies around $450kHz$.

Another important consideration is the small variation between the sediment wave velocity and water velocity. This places the observed variations within a range where distinguishing true physical phenomena from measurement errors becomes challenging. Unlike barite, where a clear trend was observed, the glass sphere data lacked a definitive correlation between compaction and velocity, suggesting that minor experimental variations or measurement inconsistencies could be influencing the results.

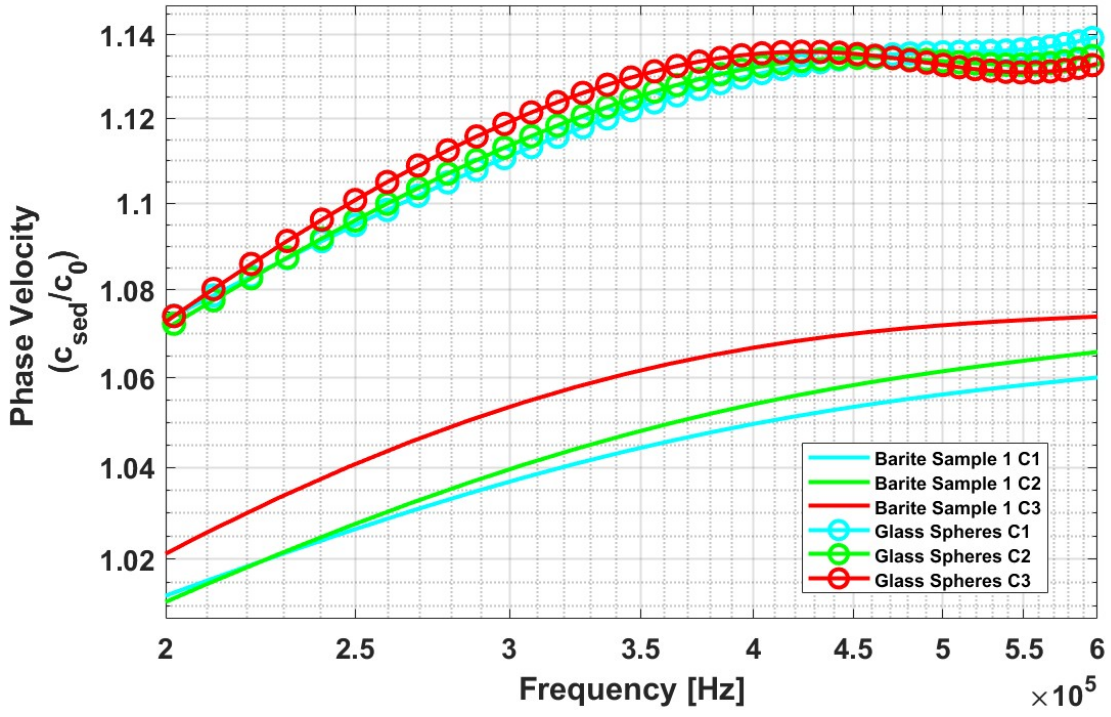

Figure 4.5 – Comparison of phase velocities between glass spheres and barite samples.

One notable observation is that the phase velocity of glass spheres is consistently higher than that of barite, as shown in Fig. 4.5. This result aligns with previously cited literature and was consistently observed across all tested samples. The possible physical explanation for these values supports the proposed factor behind the lack of an observable relationship between glass sphere compaction and attenuation: the high compaction capacity of glass spheres. Because glass spheres compact easily, their overall elastic modulus is higher than that of barite, leading to an increased wave velocity compared to barite.

5 CONCLUSIONS

One of the primary goals of this work was to measure sound speed and attenuation in sedimented barite within the high-frequency range. The study focuses on how P-wave velocity and attenuation vary with compaction, contributing to a broader effort to correlate acoustic properties with barite sediment behavior.

Alongside the barite measurements, glass spheres were under investigation to stablish a precedent of grain size distribution on the acoustic behavior during the granular compaction process.

A novel measurement cell arrangement for granular media was also proposed. While similar experimental setups are frequently used for characterizing fluids and emulsions, to the best of the author's knowledge, this method has not been previously applied to granular media. The data collected using the single transducer measurement cell showed reasonable agreement with specialized literature, emphasizing its applicability to this task.

In the analyzed $ka \approx \mathcal{O}(0.01)$ range, results indicated that increasing compaction led to a downward shift in acoustic wave attenuation magnitude in barite samples. However, no significant variations in the attenuation dependence order with frequency were observed. Meaning that a linear relationship between attenuation and frequency remained consistent across all compaction tests, without changes in slope.

A similar trend was observed for glass spheres, though it was more pronounced at lower frequencies. However, when varying the compaction level, an overall increase in slope was noted, indicating a stronger relationship between wave attenuation and frequency. This difference may arise from glass spheres being in a $ka \approx \mathcal{O}(0.1)$ range, which is more sensitive to high-frequency effects than barite. This order variation can be attributed to scattering phenomena, which are more prominent in the glass spheres' ka range.

Additionally, the results showed that acoustic attenuation in the high-frequency range is influenced not only by grain size or porosity (compaction level) but also by inter-particle interactions, including electrical effects, the degree of aggregation, particle morphology, to say the less. The absence of the expected behavior when comparing barite and glass spheres samples suggests that other uncontrolled parameters played a significant role in the acoustic attenuation data.

Phase velocity analysis in barite samples demonstrated a clear response to compaction variations. As expected for $ka << 1$ conditions, phase velocity increased with higher compaction levels. A slight positive dispersion was observed in the studied frequency range, where wave velocity increased with frequency, a behavior predicted by Biot-based models.

In contrast, the relationship between phase velocity and compaction in glass spheres was not as evident. No consistent trend was observed in velocity variations while averaging the data, whether compaction was changed or not. As discussed in Sec. 4, this could be due to the higher compaction capability of glass spheres compared to barite or the transition regime, making wave dispersion effects ambiguous.

Such differences between barite samples and glass spheres highlight how grain size—even when relatively similar—can significantly affect wave propagation, thereby altering the acoustic response due to microstructural changes such as compaction.

As noted in Sec. 3, the experimental apparatus had some operational challenges, which were detailed in that section. For future studies, a refined version of the measurement cell has been proposed to address these limitations, reducing uncertainties in the collected data.

Although the data presented in this dissertation serve a qualitative purpose, meaning exact numerical values or precise compaction behaviors were not fully captured, the overall acoustic behavior of barite as a function of compaction was effectively observed. These acoustic signatures can already be utilized for phenomenological surveys. However, since high-frequency studies aim for a more detailed microstructural understanding, the development of a more precise experimental cell becomes a crucial factor for future researches. The acoustic signature successfully recorded in this study will be further analyzed in future investigations focused on the detailed acoustic characterization of barite.

All the presented argument along this dissertation showed that the use of high-frequency ultrasound waves to study the geometry and physical behavior of sedimented barite through wave attenuation and velocity as a function of frequency has proven to be effective. High frequencies enable the analysis of grain shapes, sizes, and compaction while isolating geoacoustic properties of the medium. This is valuable for developing acoustic models that characterize granular media using remote measurement methods. By isolating and analyzing specific properties such as compaction, we can infer their evolution by identifying expected acoustic trends, thereby understanding medium behavior without direct contact. These acoustic signatures can be readily observed through acoustic methods, highlighting the potential for

surveying APB phenomena using acoustic measurement techniques.

BIBLIOGRAPHY

Adamowski, J. C.; Buiochi, F.; Simon, C.; Silva, E. C.; Sigelmann, R. A. Ultrasonic measurement of density of liquids. **Journal of the Acoustical Society of America**, v. 97, n. 1, p. 354–361, 1995.

Adams, A. J.; MacEachran, A. Impact on Casing Design of Thermal Expansion of Fluids in Confined Annuli. **SPE Drilling Completion**, v. 9, n. 03, p. 210–216, 09 1994.

Anderson, V. C. Sound scattering from a fluid sphere. **The Journal of the Acoustical Society of America**, v. 22, n. 4, p. 426–431, 1950.

Argo, T. F. Laboratory measurements of sound speed and attenuation of water-saturated granular sediments. 2012.

Argo, T. F.; Guild, M. D.; Wilson, P. S.; Schröter, M.; Radin, C.; Swinney, H. L. Sound speed in water-saturated glass beads as a function of frequency and porosity. **The Journal of the Acoustical Society of America**, v. 129, n. 4, p. EL101–EL107, 2011.

Azhari, H. **Basics of biomedical ultrasound for engineers**. [S.l.]: John Wiley & Sons, 2010.

Bjørndal, E. **Acoustic measurement of liquid density with applications for mass measurement of oil**. Tese (Doutorado) — University of Bergen, Norway, 2007.

Buckingham, M. J. Theory of compressional and shear waves in fluidlike marine sediments. **The journal of the acoustical society of America**, v. 103, n. 1, p. 288–299, 1998.

Buckingham, M. J.; Richardson, M. D. On tone-burst measurements of sound speed and attenuation in sandy marine sediments. **IEEE Journal of oceanic engineering**, v. 27, n. 3, p. 429–453, 2002.

Calçada, L.; Scheid, C.; Meleiro, L.; Ribeiro, J.; Seufitelli, G.; Peliano, S.; Santos, H. F.; Souza, E.; Monteiro, V.; Martins, A. Barite sag and its impact on annular pressure build up mitigation in producing offshore wells. In: SPE. **SPE Annual Technical Conference and Exhibition?** [S.l.], 2016. p. D021S023R008.

Carlson, J.; Deventer, J. van; Scolan, A.; Carlander, C. Frequency and temperature dependence of acoustic properties of polymers used in pulse-echo systems. In: IEEE. **IEEE Symposium on Ultrasonics, 2003**. [S.l.], 2003. v. 1, p. 885–888.

Chotiros, N. P.; Isakson, M. J. A broadband model of sandy ocean sediments: Biot–stoll with contact squirt flow and shear drag. **The Journal of the Acoustical Society of America**, v. 116, n. 4, p. 2011–2022, 2004.

Chotiros, N. P.; Isakson, M. J. High-frequency dispersion from viscous drag at the grain-grain contact in water-saturated sand. **The Journal of the Acoustical Society of America**, v. 124, n. 5, p. EL296–EL301, 2008.

Costa-Júnior, J. F.; Cortela, G. A.; Maggi, L. E.; Rocha, T. F.; Pereira, W. C.; Costa-Felix, R. P.; Alvarenga, A. V. Measuring uncertainty of ultrasonic longitudinal phase velocity estimation using different time-delay estimation methods based on cross-correlation: Computational simulation and experiments. **Measurement**, v. 122, p. 45–56, 2018.

Daniel A. Russell. The Pennsylvania State University Website. <https://www.acs.psu.edu/drussell/demos/waves/wavemotion.html>. Accessed: 2025-01-16.

Dukhin, A. S. **Ultrasound for Characterizing Colloids Particle Sizing, Zeta Potential Rheology**. [S.l.]: Elsevier, 2002.

Dunlop, J. Propagation of acoustic waves in marine sediments, a review. **Exploration Geophysics**, v. 19, n. 4, p. 513–535, 1988.

Feng, G.; Jian-Xin, W.; Bang-Rang, D.; Pin-Bo, D.; Shi-Qi, H. Influence of diffraction effects on attenuation measurement using pulse transmission method. **Journal of Geophysics and Engineering**, v. 15, n. 4, p. 1610–1623, 2018.

Flammer, G. H. **Ultrasonic measurement of suspended sediment**. [S.l.]: US Government Printing Office, 1962. v. 1141.

Gassman, F. Uber di elatizitat poröser medien. **Vierteljahrssch. Naturforsch.**, v. 91, p. 1–23, 1951.

Hamilton, E. L. Geoacoustic modeling of the sea floor. **The Journal of the Acoustical Society of America**, v. 68, n. 5, p. 1313–1340, 1980.

Hare, J.; Hay, A. E. Attenuation and group speed in water-saturated granular materials at mhz frequencies. **The Journal of the Acoustical Society of America**, v. 143, n. 5, p. 2744–2755, 2018.

Biot I, M. Theory of propagation of elastic waves in a fluid saturated porous solid. i. low frequency range. **J. Acoust. Soc. Am**, v. 28, n. 2, p. 168–178, 1956.

Biot II, M. A. Theory of propagation of elastic waves in a fluid-saturated porous solid. ii. higher frequency range. **The Journal of the acoustical Society of america**, v. 28, n. 2, p. 179–191, 1956.

Irawan, S.; Kinif, B.; Bayuaji, R. Maximizing drilling performance through enhanced solid control system. In: IOP Publishing. **IOP Conference Series: Materials Science and Engineering**. [S.l.], 2017. v. 267, n. 1, p. 012038.

Jackson, D.; Richardson, M. **High-frequency seafloor acoustics**. [S.l.]: Springer Science & Business Media, 2007.

Kažys, R.; Mažeika, L.; Barauskas, R.; Jasiūnien, E.; Daniulaitis, V. Evaluation of diffraction errors in precise pulse-echo measurements of ultrasound velocity in chambers with waveguide. **Ultrasonics**, v. 40, n. 1-8, p. 853–858, 2002.

Khimunin, A. Numerical calculation of the diffraction corrections for the precise measurement of ultrasound absorption. **Acta Acustica united with Acustica**, v. 27, n. 4, p. 173–181, 1972.

Kimura, M. Velocity dispersion and attenuation in granular marine sediments: Comparison of measurements with predictions using acoustic models. **The Journal of the Acoustical Society of America**, v. 129, n. 6, p. 3544–3561, 2011.

Kimura, M. Erratum: Velocity dispersion and attenuation in granular marine sediments: Comparison of measurements with predictions using acoustic models [j. acoust. soc. am. 129, 3544–3561 (2011)]. **The Journal of the Acoustical Society of America**, v. 135, n. 4, p. 2126–2127, 2014.

Kinsler, L. E.; Frey, A. R.; Coppens, A. B.; Sanders, J. V. **Fundamentals of acoustics**. [S.l.]: John wiley & sons, 2000.

Krautkrämer, J.; Krautkrämer, H. **Ultrasonic testing of materials**. [S.l.]: Springer Science & Business Media, 2013.

Lee, K.; Park, E.; Seong, W. High frequency measurements of sound speed and attenuation in water-saturated glass-beads of varying size. **The Journal of the Acoustical Society of America**, v. 126, n. 1, p. EL28–EL33, 2009.

Lee, K. I.; Humphrey, V. F.; Kim, B.-N.; Yoon, S. W. Frequency dependencies of phase velocity and attenuation coefficient in a water-saturated sandy sediment from 0.3 to1. 0mhz. **The Journal of the Acoustical Society of America**, v. 121, n. 5, p. 2553–2558, 2007.

Leurer, K. C. Attenuation in fine-grained marine sediments: Extension of the biot-stoll model by the "effective grain model"(egm). **Geophysics**, v. 62, n. 5, p. 1465–1479, 1997.

Lofqvist, T. Ultrasonic wave attenuation and phase velocity in a paper-fibre suspension. In: IEEE. **1997 IEEE Ultrasonics Symposium Proceedings. An International Symposium (Cat. No. 97CH36118)**. [S.l.], 1997. v. 1, p. 841–844.

Lowan, A. N. **Scattering and Radiation from Circular Cylinders and Spheres: Tables of Amplitudes and Phase Angles**. [S.l.]: US Navy Department, Office of research and inventions, 1946. v. 62.

McCann, C.; McCann, D. The attenuation of compressional waves in marine sediments. **Geophysics**, v. 34, n. 6, p. 882–892, 1969.

McClements, D.; Fairley, P. Ultrasonic pulse echo reflectometer. **Ultrasonics**, v. 29, n. 1, p. 58–62, 1991.

McClements, D.; Fairley, P. Frequency scanning ultrasonic pulse echo reflectometer. **Ultrasonics**, v. 30, n. 6, p. 403–405, 1992.

McClements, D. J. Principles of ultrasonic droplet size determination in emulsions. **Langmuir**, v. 12, n. 14, p. 3454–3461, 1996.

McClements, D. J. *et al.* Ultrasonic measurements in particle size analysis. **Encyclopedia of analytical chemistry**, p. 5581–5588, 2000.

Moe, B.; Erpelding, P. Annular pressure buildup: What it is and what to do about it. **World Oil**, v. 221, n. 8, p. 21–23, 2000.

Multiphysics, C. Introduction to comsol multiphysics®. **COMSOL Multiphysics, Burlington, MA, accessed Feb**, v. 9, p. 2018, 1998.

Nguyen, T.; Miska, S.; Yu, M.; Takach, N. Predicting dynamic barite sag in newtonian-oil based drilling fluids in pipe. 2011.

Nolle, A.; Hoyer, W.; Mifsud, J.; Runyan, W.; Ward, M. Acoustical properties of water-filled sands. **The Journal of the Acoustical Society of America**, v. 35, n. 9, p. 1394–1408, 1963.

Ohkawa, K. Confirmation of the biot theory for water-saturated sands at high frequencies and effects of scattering on the attenuation of sound waves. **The Journal of the Acoustical Society of America**, v. 119, n. 2, p. 709–711, 2006.

Papadakis, E. P. Ultrasonic diffraction loss and phase change in anisotropic materials. **The Journal of the Acoustical Society of America**, v. 40, n. 4, p. 863–876, 1966.

Papadakis, E. P. Buffer-rod system for ultrasonic attenuation measurements. **The Journal of the Acoustical Society of America**, v. 44, n. 5, p. 1437–1441, 1968.

Peters, F.; Petit, L. A broad band spectroscopy method for ultrasound wave velocity and attenuation measurement in dispersive media. **Ultrasonics**, v. 41, n. 5, p. 357–363, 2003.

Pickering, J. D. **Ultrafast lasers and optics for experimentalists**. [S.l.]: IOP Publishing, 2024.

Riebel, U.; Löffler, F. The fundamentals of particle size analysis by means of ultrasonic spectrometry. **Particle & Particle Systems Characterization**, v. 6, n. 1-4, p. 135–143, 1989.

Rogers, P. H.; Van Buren, A. L. An exact expression for the lommel-diffraction correction integral. **the Journal of the Acoustical Society of America**, v. 55, n. 4, p. 724–728, 1974.

Schulte, K. **KIMBERLY SCHULTE Lumenwaymaker**. Disponível em: <https://courses.lumenlearning.com/geo/chapter/about-this-course/>.

Schwartz, L.; Plona, T. Ultrasonic propagation in close-packed disordered suspensions. **Journal of applied physics**, v. 55, n. 11, p. 3971–3977, 1984.

Seifert, P. K. Effect on ultrasonic signals of viscous pore fluids in unconsolidated sand. v. 106, n. 6, p. 3089–3094, 1999.

Sessarego, J.-P.; Ivakin, A. N.; Ferrand, D. Frequency dependence of phase speed, group speed, and attenuation in water-saturated sand: Laboratory experiments. **IEEE journal of oceanic engineering**, v. 33, n. 4, p. 359–366, 2008.

Shin, K.; Hammond, J. **Fundamentals of signal processing for sound and vibration engineers**. [S.l.]: John Wiley & Sons, 2008.

Silva, C. A. M. da. **Desenvolvimento de um sistema computacional e experimental para caracterização de emulsões por meio da técnica de espectroscopia ultrassônica= Development of a computational and experimental system for characterization of emulsions using the ultrasonic spectroscopy technique**. Tese (Doutorado) — [sn], 2020.

Stoll, R. D. **Sediment acoustics**. [S.l.: s.n.], 1989.

Tang, X.; Toksöz, M. N.; Tarif, P.; Wilkens, R. H. A method for measuring acoustic wave attenuation in the laboratory. **The Journal of the Acoustical Society of America**, v. 83, n. 2, p. 453–462, 1988.

Shirley D. J. ; Bell, D. W. **Laboratory and field studies of sediment acoustics**. [S.l.]: Texas Univ., Austin. Applied Research Labs, 1979.

Vargo Richard F., J.; Payne, M.; Faul, R.; LeBlanc, J.; Griffith, J. E. Practical and Successful Prevention of Annular Pressure Buildup on the Marlin Project. **SPE Drilling Completion**, v. 18, n. 03, p. 228–234, 09 2003.

Wang, H.; Zhang, H.; Li, J.; Sun, T. Study on annular pressure buildup phenomenon in subsea wells considering the effect of cement. **Energy Science & Engineering**, v. 10, n. 1, p. 81–95, 2022.

Weight, J. P. A model for the propagation of short pulses of ultrasound in a solid. **The Journal of the Acoustical Society of America**, v. 81, n. 4, p. 815–826, 1987.

Williams, A. The piston source at high frequencies. **The Journal of the Acoustical Society of America**, v. 23, n. 1, p. 1–6, 1951.

Williams, K. L.; Jackson, D. R. Bistatic bottom scattering: Model, experiments, and model/data comparison. **The Journal of the Acoustical Society of America**, v. 103, n. 1, p. 169–181, 1998.

Williams, K. L.; Jackson, D. R.; Thorsos, E. I. Comparison of sound speed and attenuation measured in a sandy sediment to predictions based on the biot theory of porous media. **IEEE journal of oceanic engineering**, v. 27, n. 3, p. 413–428, 2002.

Wood, A. B. Textbook of sound. 1946.

Wu, D.; Qian, Z.; Shao, D. Sound attenuation in a coarse granular medium. **Journal of sound and vibration**, v. 162, n. 3, p. 529–535, 1993.

Yang, H.; Seong, W. High frequency compressional wave speed and attenuation measurements in water-saturated granular media with unimodal and bimodal grain size distributions. **The Journal of the Acoustical Society of America**, v. 143, n. 2, p. 659–665, 2018.

Zhang, G.; Li, X.; Zhang, S.; Kundu, T. Investigation of frequency-dependent attenuation coefficients for multiple solids using a reliable pulse-echo ultrasonic measurement technique. **Measurement**, v. 177, p. 109270, 2021.

Zwikker, C. Sound absorbing materials. 1949.

Tonn, R. Comparison of seven methods for the computation of q. **Physics of the Earth and Planetary interiors**, v. 55, n. 3-4, p. 259–268, 1989.

Tournat, V.; Gusev, V. Acoustics of unconsolidated “model” granular media: An overview of recent results and several open problems. **Acta Acustica united with Acustica**, v. 96, n. 2, p. 208–224, 2010.

APPENDIX A – COLLECTED DATA REPRESENTATION

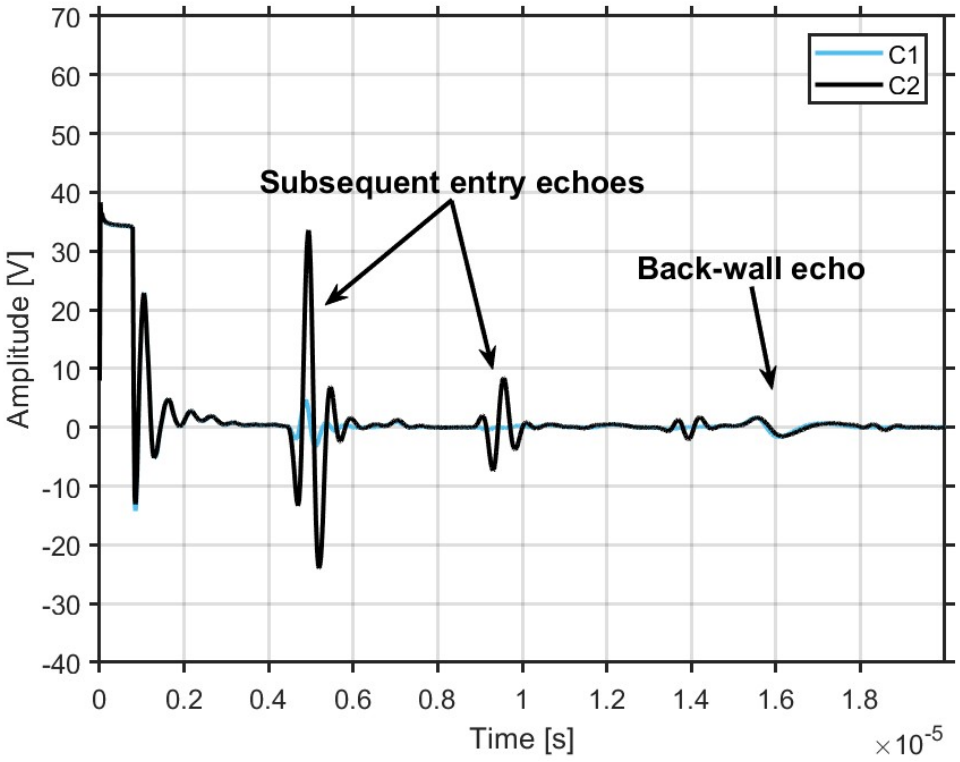

Figure A.1 – Complete vector in time domain.

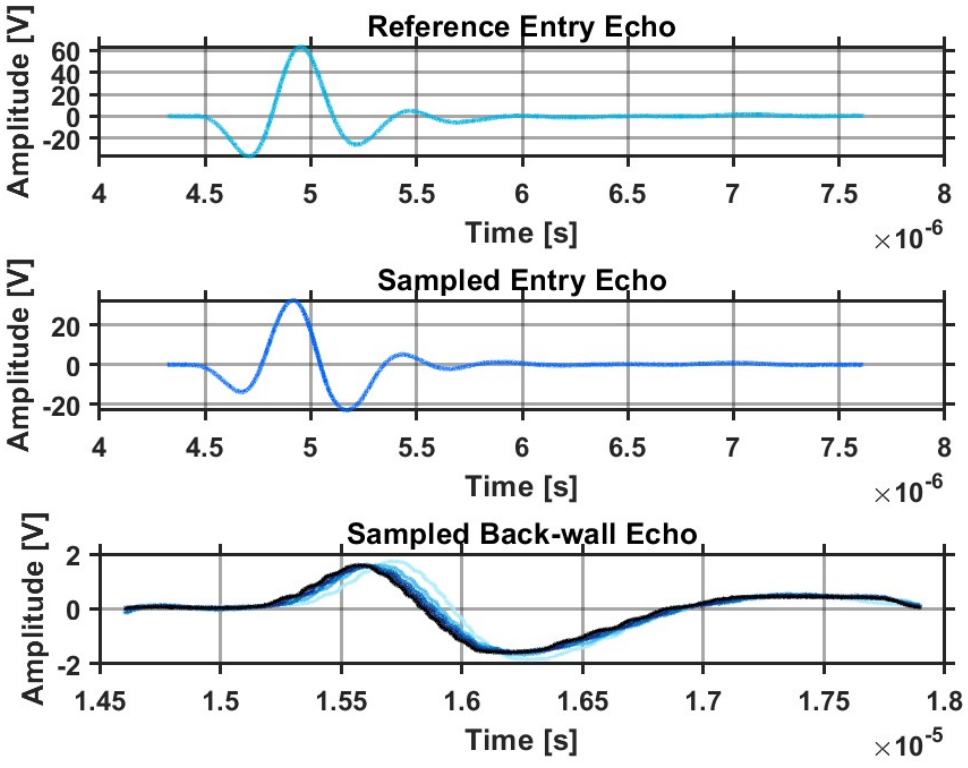

Figure A.2 – Separated echoes in time domain.

APPENDIX B – NUMERICAL SIMULATION FOR EXPERIMENTAL CELL OPTIMIZATION

This section presents numerical simulations intended to enhance the design of the ultrasound cell described in Sec. 3.2.3. These simulations are carried out using Finite Element Method (FEM) environments, which are essential tools for analyzing wave behavior within ultrasonic measurement setups and are widely accessible to engineers. One of the main challenges addressed in this study is the presence of internal reflections and wave superpositions, which can interfere with signal clarity and distort the acoustic field, thereby degrading measurement quality, as previously discussed in Sec. 3.2.3.

Concerning back-wall echoes, a specific issue arises from the high wave velocity of stainless steel (approximately $5,800.00m/s$). When employing a steel plate at the bottom, even with a substantial thickness of $1cm$, it results in a double back-wall echo from the opposite face of the plate, with a delay of about $3\mu s$ between the two back-wall echoes, which complicates identifying the desired echo. In the work by (Lofqvist 1997), an inclined back-wall bottom was introduced to mitigate unwanted reflections. In this dissertation, rather than using the same approach, different geometries were analyzed to determine which provided the best results.

Several geometries were tested in a $COMSOL$ environment aiming for the optimized back-wall echoes. Below we can see some of the geometries tested and their back-wall echoes received by a probe placed in the position of the receiver transducer. In Fig. B.1, the echo behavior for each geometry can be seen graphically:

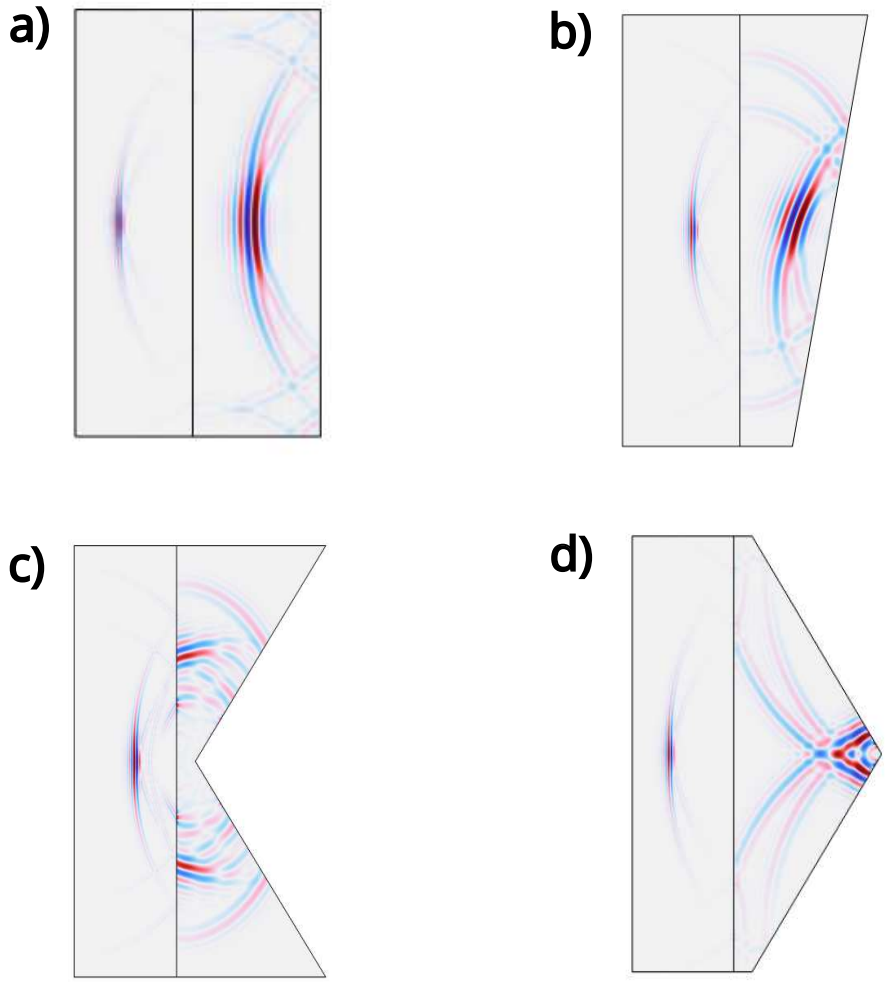

Figure B.1 – Numerical representation of the wave behavior within the cell using FEM method (Multiphysics 1998).

For a thick rod, represented by Fig. B.1a, the unwanted echo was detected right before the back-wall echo Fig. B.2, in $0.75 \times 10^{-4}s$ and $1 \times 10^{-4}s$.

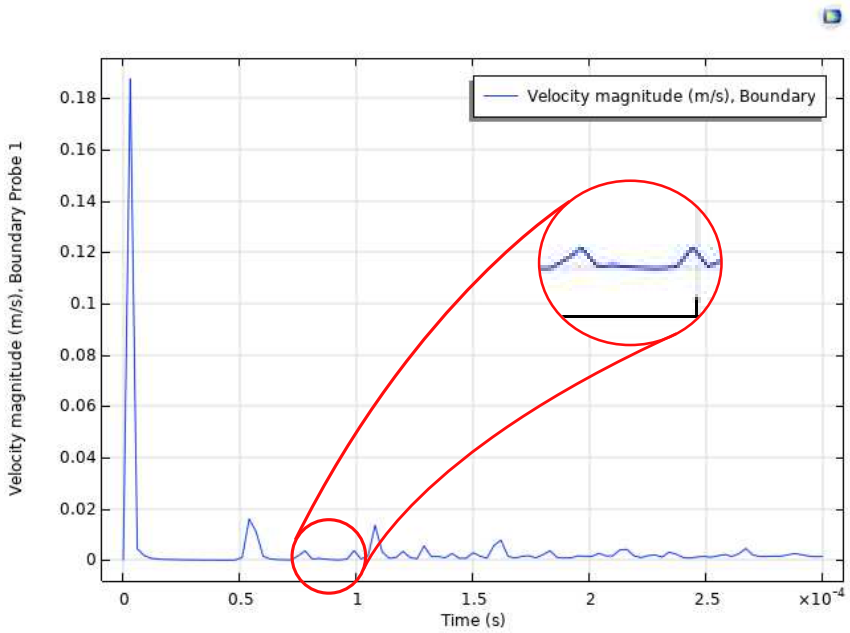

Figure B.2 – Unwanted echoes using a flat back-wall end.

Using an inclined bottom Fig. B.1b, as used by Lofqvist 1997, it can be observed that the echoes are closer to the back-wall echo compared to those in Fig. B.2, albeit with slightly weaker amplitudes.

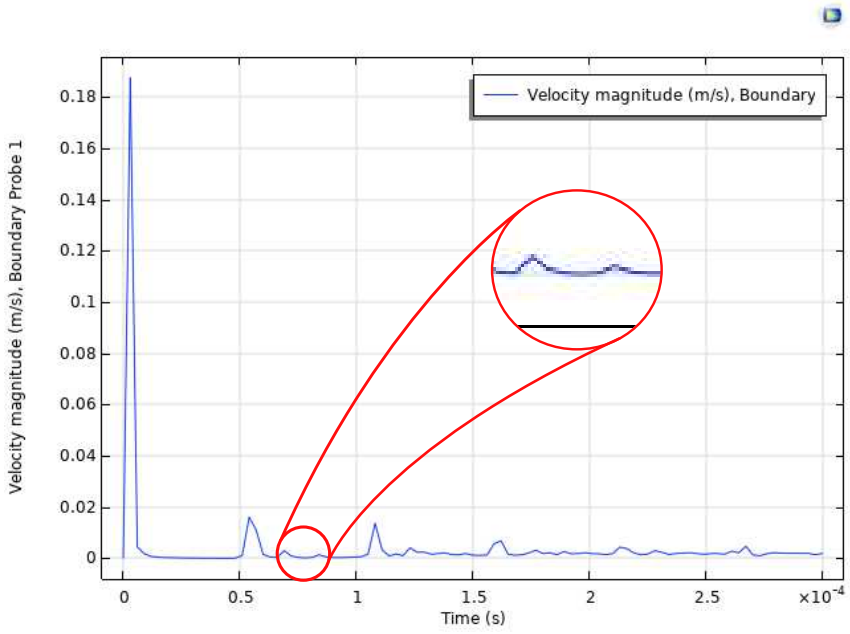

Figure B.3 – Unwanted echoes using a inclined back-wall end.

As presented in Fig. B.4, the conic geometry, represented by Fig. B.1(d) returned the best data compared to the previous ones, and only a slightly unwanted echo was observed with a acceptable amplitude within $0.5 \times 10^{-4}s$ and $1 \times 10^{-4}s$.

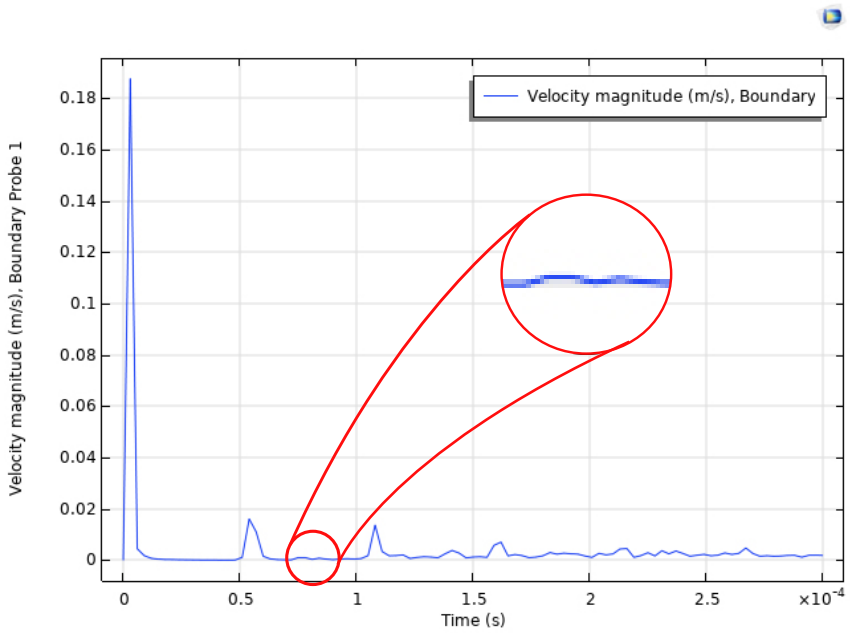

Figure B.4 – Unwanted echoes using a positive conic back-wall end.

However, the clearer subsequent echoes were made using a negative conic shape Fig.B.1(c), as can be seen in Fig.B.5.

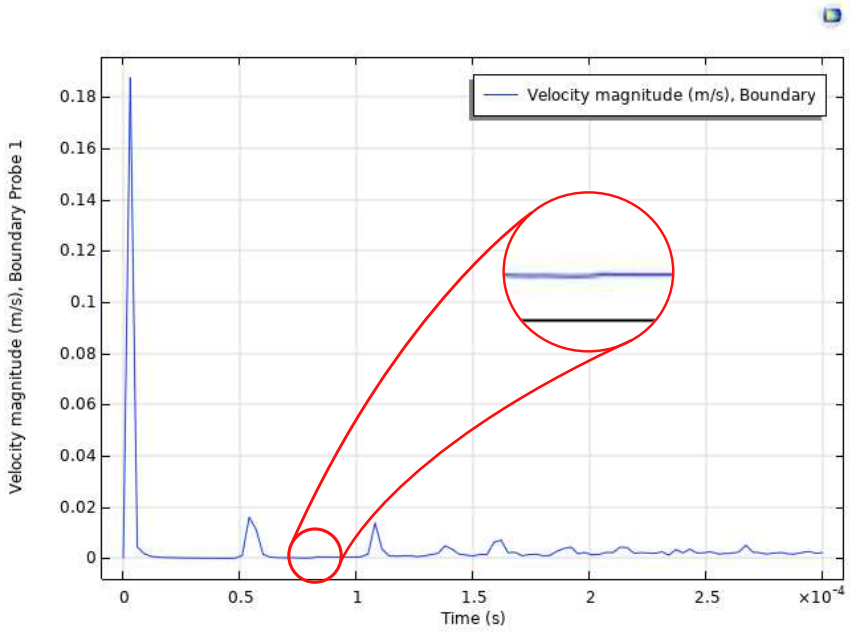

Figure B.5 – Unwanted echoes using a negative conic back-wall end.

Therefore, based on the data obtained, the two geometries shown in Figs. B.5 and B.4 provided the best results in terms of minimizing subsequent echoes from the back-wall rod. These geometries are represented in a simplified form in Fig. B.8.

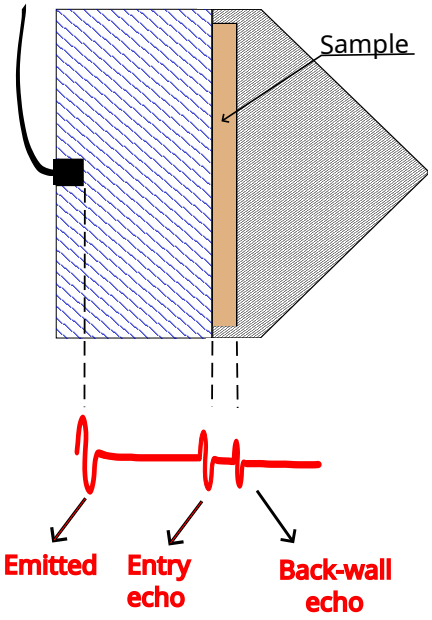

Figure B.6 – Geometry as the simulation from Fig.B.1(d).

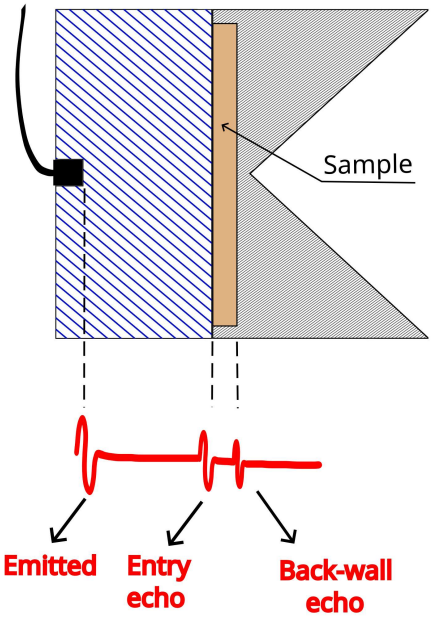

Figure B.7 – Geometry as the simulation from Fig.B.1(c).

Figure B.8 – Out of scale representation of the improved ultrasonic measurement cells.

Even though Fig. B.1(c) yielded the best data between the two geometries, its mechanical complexity during fabrication is the primary concern when selecting this design. However, since the goal of this section is to present the acoustical challenges of ultrasonic cell construction and how to address them, the geometry that produced the clearest data will be used despite its

fabrication difficulty.

Another point of concern related to the cell geometry is the presence of side echoes and the delay between the entry echo and the back-wall echo due to the sample's depth.

To mitigate these issues, in Sec. 3.2.1, literature values were chosen that significantly exceed the minimum sample size required to prevent echo overlap, thereby accounting for uncontrolled variables. The referenced literature recommends sample depths between 5 and 10 times the wavelength used, ensuring they are sufficiently large.

However, more dispersive media broaden the emitted pulse, resulting in a greater effective wavelength than that selected by the signal generator (Sec.3.1.3). Thus, using fixed values for sample depth based solely on the chosen wavelength for all materials is not the most optimal approach. In despite of that, this is the simplest and quickest method to apply.

In the case of barite, an excessive sample depth could result in complete signal dissipation within the material, making it essential to determine an optimal depth suitable for our specific sample.

Following this approach, an analysis was conducted using COMSOL (Multiphysics 1998) to determine the optimal sample depth for a highly dissipative medium. The tested sample was constrained by COMSOL's viscous model, an equivalent-fluid model that simulates sound propagation in a fluid while accounting for viscous losses within the bulk. Although this model does not perfectly represent a granular medium, it provided a reasonable initial approximation.

The tested geometry is depicted in Fig.B.9.

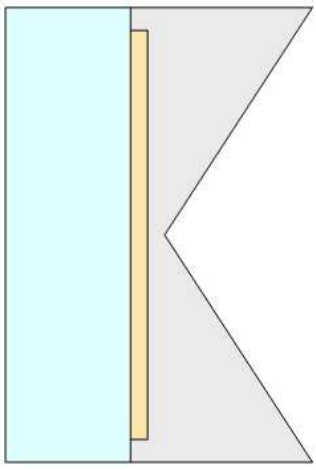

Figure B.9 – Geometry tested in COMSOL (Multiphysics 1998).

In this figure, the cyan color represents the acrylic buffer rod, the sample is shown in beige, and the back-wall is in gray.

The acoustic field behavior within the cell is presented in Fig. B.10:

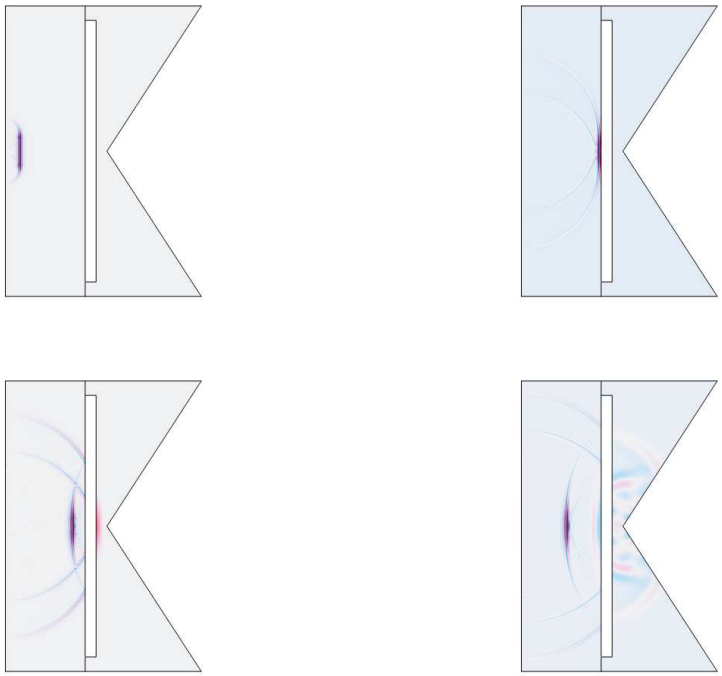

Figure B.10 – Sound field within the optimized ultrasound measurement cell.

Visually, the first two echoes correspond to the entry and back-wall reflections.

A probe was placed at the transducer's position to collect acoustic pressure data, simulating the pulse-echo procedure, as shown in Fig.B.11.

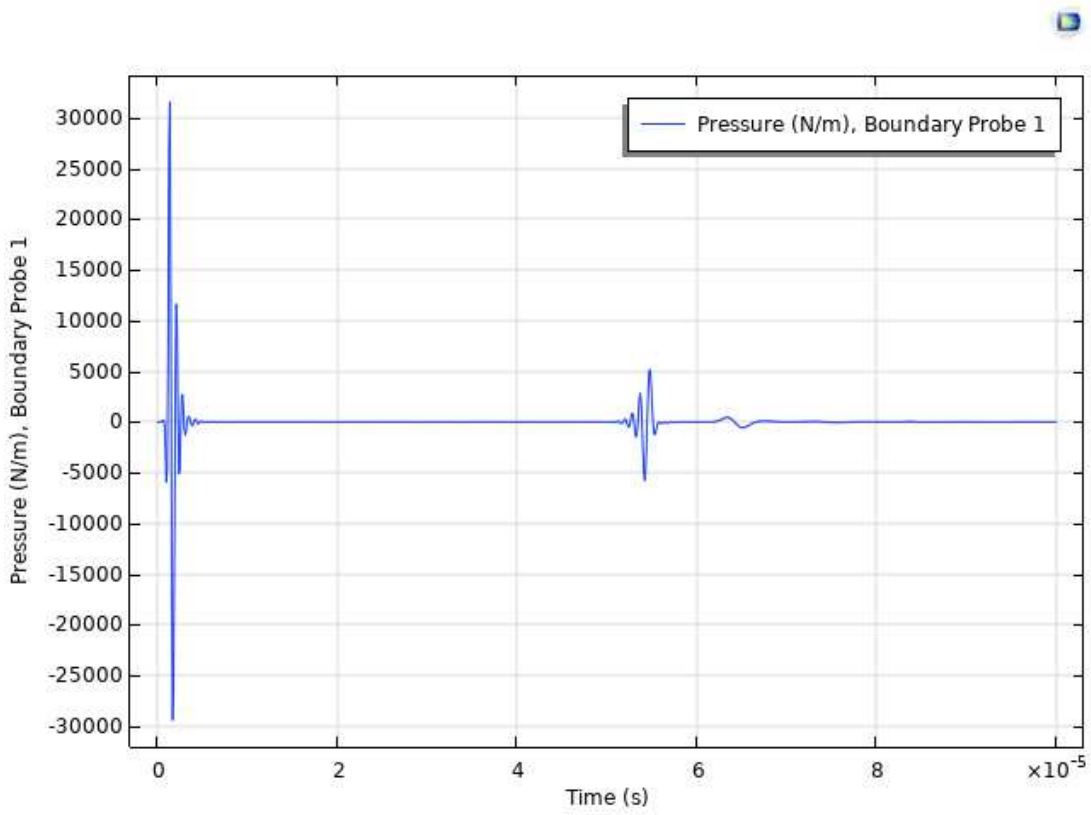

Figure B.11 – Acoustic data collected from the probe.

As seen in Fig. B.11, the selected sample depth is ideal, providing a clear gap between the two desired echoes in approximately $6E-5s$. The chosen sample's depth is smaller than the literature-recommended values discussed in Sec. 3.2. This reduction was partly influenced by prior results obtained through FEM techniques, which allowed for a shorter wave propagation path, thereby improving the signal-to-noise ratio.

Another important observation concerns the frequency downshift caused by the transducer's half-power bandwidth, which is discussed in detail in Sec. 3.4. Fig. B.12 illustrates this shift, where meaningful data is displaced from the resonance pulse frequency initially set in the system.

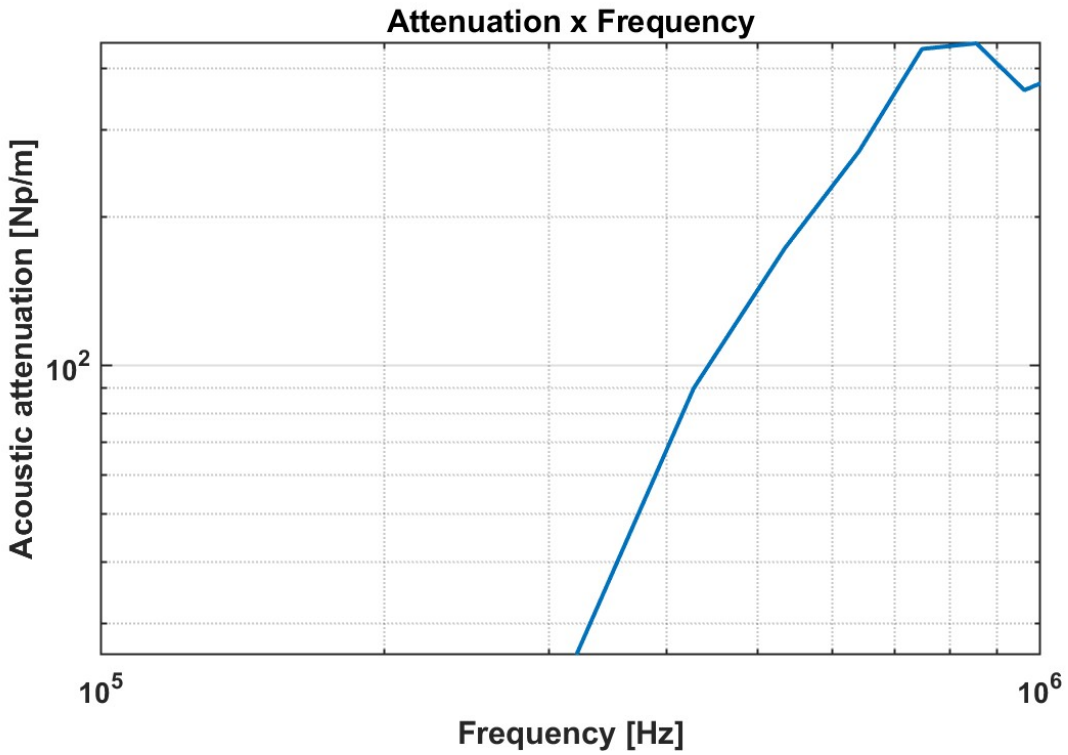

Figure B.12 – Sample attenuation using FEM.

The attenuation as a function of frequency, shown in Fig. B.12, exhibits reasonable values around $300kHz$ and $700kHz$ for the tested sample, emphasizing the unavoidable downward shift in the transducer's optimal frequency band.

This type of analysis can help the acoustic engineer purchase and order the appropriate equipment, knowing its behavior in a real application. In this case, the use of an ultrasonic transducer with a $1MHz$ resonance frequency will result in a reasonable acoustic study around $400kHz$ for this type of dissipative material.

The discussion presented this Section showcases an improved ultrasonic cell compared to the one used in this work, as presented in Section 3.2.1. The data provided here aim to illustrate how acoustic waves propagate in this type of cell and how its geometry can be optimized.